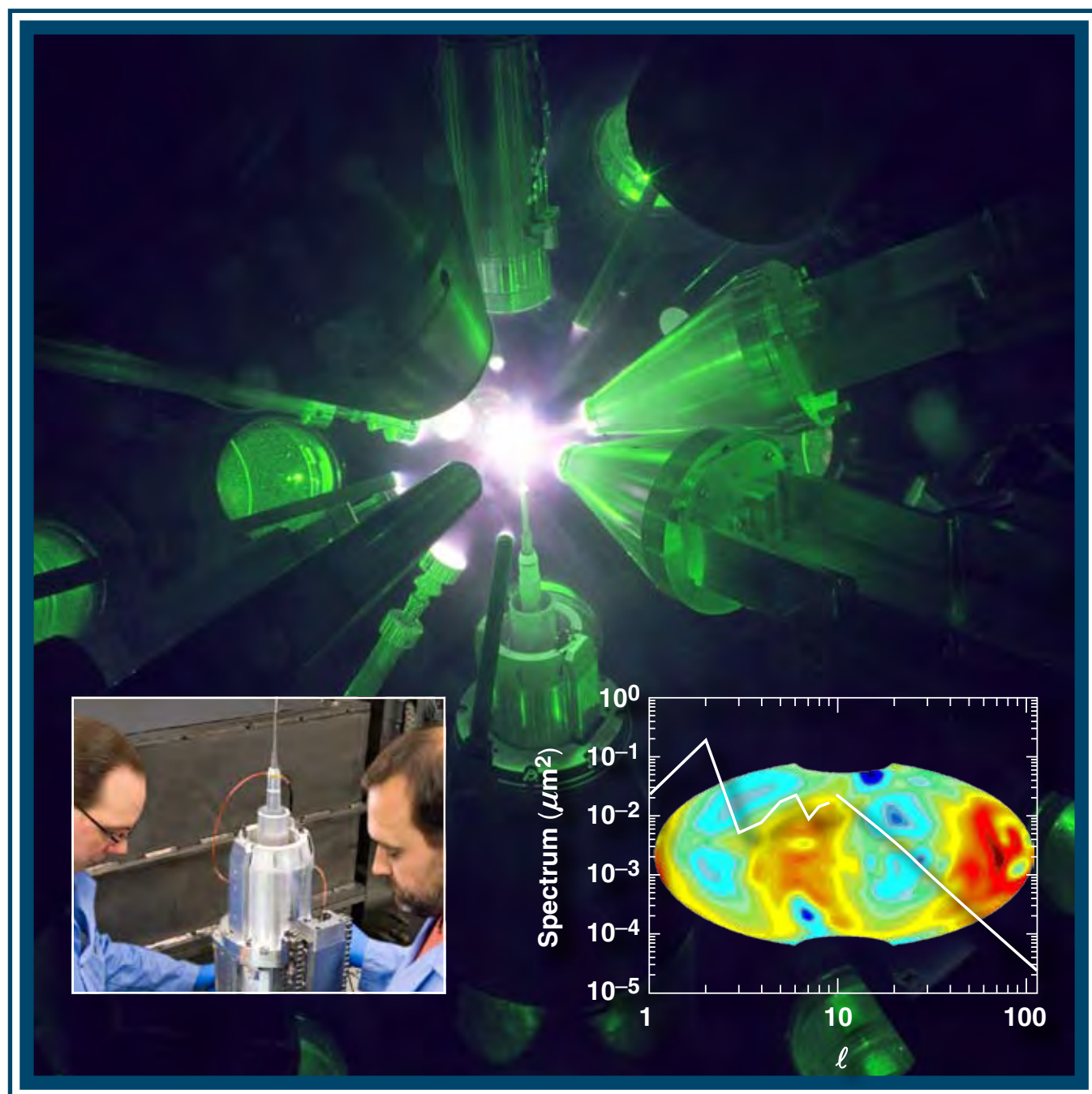


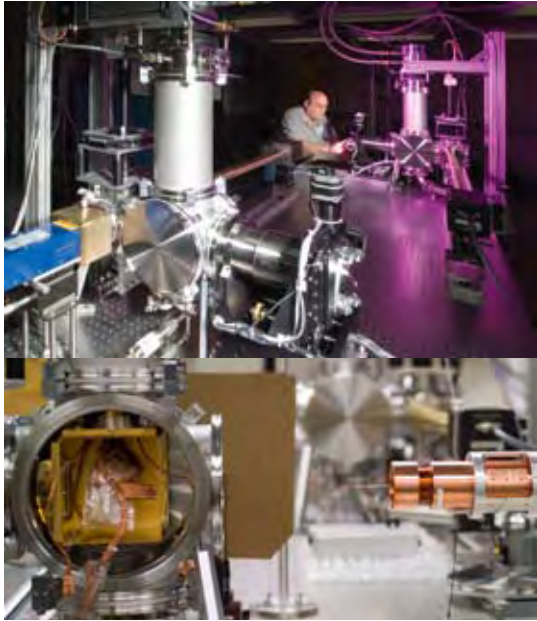
LLE Review

Quarterly Report



About the Cover:

Cryogenic direct-drive targets scaled from NIF ignition and high-gain target designs are a critical element of LLE's experimental program. A major recent accomplishment has been optimizing the layering process and producing cryogenic targets with a consistently high quality (see **Cryogenic Targets: Current Status and Future Development**, p. 57). A cryogenic target implosion is shown where the cryogenic target handling equipment and many target diagnostics in the OMEGA target chamber are illuminated by unconverted 2ω laser light. The target is delivered in a moving cryostat to target chamber center and the target is exposed when the thermal shrouds (seen in the upper central portion of the image) are pulled away from the target support. Senior Technical Associates



Steven Verbridge (left) and Alfred Weaver (right) prepare a cryogenic target system with the thermal shrouds removed (lower left-hand inset) for a final evaluation before the equipment is returned to service. The calculated power spectrum for the first 100 modes, which meets the NIF roughness specification, is superimposed (lower right-hand inset) on an Aitoff projection of the thickness variations in a 95- μm -thick cryogenic DT-ice layer.

The inside cover photo shows Research Engineer Mark Wittman preparing the cryogenic fill-tube test facility for experiments that will study target layering in NIF-scale targets and fast-ignition targets. This facility is independent of the OMEGA Cryogenic Target Handling System and will be used to define the engineering requirements and protocol for achieving high-quality ice layers in cryogenic targets that are substantially larger than targets fielded on OMEGA, or contain features that will likely perturb the ice layer, such as the fill tube, a fast-ignition cone, or a "Saturn ring." The upper image shows the two cryostats, the x-ray phase-contrast imaging system, the optical shadowgraphy imaging system, and the target positioning system. The lower image shows a target attached to a fill tube that is about to be installed into the cryogenic system.

This report was prepared as an account of work conducted by the Laboratory for Laser Energetics and sponsored by New York State Energy Research and Development Authority, the University of Rochester, the U.S. Department of Energy, and other agencies. Neither the above named sponsors, nor any of their employees, makes any warranty, expressed or implied, or assumes any legal liability or responsibility for the accuracy, completeness, or usefulness of any information, apparatus, product, or process disclosed, or represents that its use would not infringe privately owned rights. Reference herein to any specific commercial product, process, or service by trade name, mark, manufacturer, or otherwise, does not necessarily constitute or imply its endorsement, recommendation, or favoring by

the United States Government or any agency thereof or any other sponsor. Results reported in the LLE Review should not be taken as necessarily final results as they represent active research. The views and opinions of authors expressed herein do not necessarily state or reflect those of any of the above sponsoring entities.

The work described in this volume includes current research at the Laboratory for Laser Energetics, which is supported by New York State Energy Research and Development Authority, the University of Rochester, the U.S. Department of Energy Office of Inertial Confinement Fusion under Cooperative Agreement No. DE-FC52-08NA28302, and other agencies.

Printed in the United States of America

Available from

National Technical Information Services

U.S. Department of Commerce

5285 Port Royal Road

Springfield, VA 22161

Price codes: Printed Copy A04

Microfiche A01

For questions or comments, contact Jonathan D. Zuegel, Editor, Laboratory for Laser Energetics, 250 East River Road, Rochester, NY 14623-1299, (585) 275-4425.

Worldwide-Web Home Page: <http://www.lle.rochester.edu/>

LLE Review

Quarterly Report



Contents

In Brief	iii
Cryogenic Targets: Current Status and Future Development	57
Multiple-FM Smoothing by Spectral Dispersion— An Augmented Laser Speckle Smoothing Scheme	73
Monoenergetic Proton Radiography Measurements of Implosion Dynamics in Direct-Drive Inertial Confinement Fusion	81
High-Dynamic-Range, Single-Shot Cross-Correlator Based on an Optical Pulse Replicator	86
Application of Phase Retrieval for Characterizing a High-Intensity Focused Laser Field	94
Optimization of Laser-Damage Resistance of Evaporated Hafnia Films at 351 nm	103
Publications and Conference Presentations	

In Brief

This volume of the LLE Review, covering January–March 2008, features “Cryogenic Targets: Current Status and Future Development,” by D. R. Harding, D. H. Edgell, M. D. Wittman, L. M. Elasky, S. J. Verbridge, A. J. Weaver, L. D. Lund, W. Seka, W. T. Shmayda, R. T. Janezic, M. J. Shoup III, M. Moore, R. Junquist, and A. V. Okishev. In this article (p. 57), the authors report on the status of layering cryogenic DT and D₂ targets at LLE for inertial confinement fusion (ICF) targets. This critical effort achieves the important milestone of routinely providing cryogenic DT targets that meet the 1.0- μm (rms) OMEGA ice-quality-surface specification. The best D₂-ice layers produced so far (rms roughness of 1.1 μm) are approaching the quality typically achieved in DT targets. Efforts to improve the consistency of this process are reported along with investigations supporting the National Ignition Campaign studying issues relevant to indirect-drive and direct-drive cryogenic targets.

Additional highlights of recent research presented in this issue include the following:

- J. A. Marozas, T. J. B. Collins, and J. D. Zuegel present an improved laser speckle smoothing scheme that augments the current NIF 1-D SSD system by using multiple-FM modulators (MultiFM 1-D SSD) (p. 73). With a judicious choice of modulator frequencies, MultiFM 1-D SSD smoothes resonances produced at the higher spatial frequencies and can attain similar or even faster smoothing rates compared to the baseline NIF 2-D SSD system. *DRACO* simulations have shown that MultiFM 1-D SSD beam smoothing is sufficient for the direct-drive-ignition targets and pulse shapes analyzed thus far, and may even allow reducing the bandwidth enough to eliminate the need for dual-tripler frequency conversion on the NIF.
- C. K. Li, F. H. Séguin, J. R. Rygg, J. A. Frenje, M. Manuel, and R. D. Petrasso (Plasma Science Fusion Center, MIT), along with R. Betti, J. A. Delettrez, J. P. Knauer, F. J. Marshall, D. D. Meyerhofer, V. A. Smalyuk, and C. Stoeckl (LLE), D. Shvarts (Nuclear Research Center Negev), O. L. Landen and R. P. J. Town (LLNL), and C. A. Back and J. D.ilkenny (General Atomics) describe time-gated, monoenergetic proton radiography that provides unique measurements of implosion dynamics of spherical targets in direct-drive inertial confinement fusion (ICF) (p. 81). Radiographs obtained at different implosion times, from acceleration, through coasting, deceleration, to final stagnation, display a comprehensive picture of spherical ICF implosion. Critical information inferred from such images characterizes the spatial structure and temporal evolution of self-generated fields and plasma areal density.
- C. Dorrer, J. Bromage, and J. D. Zuegel describe a single-shot cross-correlator based on a pulse replicator that produces a discrete sequence of sampling pulses that are nonlinearly mixed with the pulse under test (p. 86). The combination of a high reflector and partial reflector replicates an optical pulse by multiple internal reflections and generates a sequence of spatially displaced and temporally delayed sampling pulses. This principle is used in a cross-correlator characterizing optical pulses at 1053 nm, where a dynamic range higher than 60 dB is obtained over a temporal range larger than 200 ps. The dynamic range can be extended with standard optical-density filters and the temporal range extended with larger optics.

- S.-W. Bahk, J. Bromage, I. A. Begishev, C. Mileham, C. Stoeckl, M. Storm, and J. D. Zuegel present a novel focal-spot diagnostic developed for OMEGA EP that will be used to characterize on-shot focal spots to support high-quality laser–matter interaction experiments (p. 94). The complex fields in the region of the high-energy focus are calculated using high-resolution measurements of the main beam wavefront using the focal-spot diagnostic (FSD) located on the short-pulse diagnostic package and a careful calibration of the transfer wavefront between the FSD instrument and target chamber center. The concept of this calibration procedure is experimentally verified in the Multi-Terawatt (MTW) Laser System, which serves as a development platform for OMEGA EP. A technique based on phase retrieval is employed for the transfer-wavefront calibration since the OMEGA EP infrastructure cannot be replicated in the MTW laser; however, this approach also shows promise as an alternative method for OMEGA EP.
- J. B. Oliver, S. Papernov, A. W. Schmid, and J. C. Lambropoulos report on a systematic study to improve the laser-damage resistance of multilayer high-reflector coatings for use at 351 nm on the OMEGA EP Laser System (p. 103). A series of hafnium dioxide monolayer films deposited by electron-beam evaporation with varying deposition rates and oxygen backfill pressures were studied using transmission electron microscopy (TEM), x-ray diffraction (XRD), and refractive index modeling. These exhibit microstructural changes for sufficiently slow deposition rates and high oxygen backfill pressures, resulting in an absence of crystalline inclusions and a lower refractive index. This process was used to fabricate reduced-electric-field-type multilayer, high-reflector coatings that achieved laser-damage thresholds as high as 16.6 J/cm^2 , which represents exceptional improvement over previous damage thresholds measured at this wavelength of the order of 3 to 5 J/cm^2 .

Jonathan Zuegel
Editor

Cryogenic Targets: Current Status and Future Development

Introduction

Twenty years ago the beta-layering mechanism was proposed for achieving a uniformly thick deuterium–tritium (DT)-ice layer in an inertial confinement fusion (ICF) capsule.¹ Experiments with DT-filled capsules confirmed the feasibility of that mechanism,² but only now have DT cryogenic targets been demonstrated to be reliably produced with the inner surface of the DT layer possessing the quality required for achieving ignition: a roughness better than 1.0- μm root mean square (rms). Importantly, these results were accomplished in equipment that interfaces with the OMEGA laser, which enables the targets to be imploded in ignition-relevant experiments. Achieving the ice-quality milestone demonstrated the feasibility and adequacy of the beta-layering method, but repeatedly achieving high-quality ice layers is equally important since it allows ICF implosion experiments to be performed where other critical parameters can be varied.³ This article discusses the process and presents the important issues that affect the quality of the ice layer.

While targets with DT-ice layers are required to achieve ignition, targets with pure-deuterium (D_2)-ice layers make it possible to (1) diagnose the areal density³ and (2) increase the throughput of cryogenic targets for experiments that could otherwise be achieved with DT because of the radiological complications with handling tritium. In the absence of heating from the decay of tritium, an alternative volumetric heating technique in D_2 is based on the absorption of IR radiation.⁴ However, achieving uniform illumination of the capsule while minimizing the effect of energy absorbed in the support structure of the target made it substantially more difficult to achieve the 1.0- μm -rms specification for D_2 than for DT. Nevertheless, as our understanding of the ice layer's sensitivity to the thermal environment has improved, so has our ability to better control the D_2 -ice quality; currently we are very close to the ice-quality requirement. The issues and complexities associated with layering D_2 are discussed here.

As our ability to reliably provide high-quality cryogenic targets for implosion experiments has progressed to a produc-

tion process, new technical challenges for producing cryogenic targets have presented themselves. The greatest challenge is to provide new types of targets for use on the National Ignition Facility: plastic shells that incorporate a foam ablator, targets that are filled through a fill tube rather than by permeation, and targets that are sub-cooled below the liquid–solid transition (19.7 K). These new research opportunities and issues associated with them are presented in this article.

Cryogenic Target Production and Characterization

The design philosophy, equipment, capabilities, and operations used to produce cryogenic targets have been reviewed extensively.⁵ In summary, 0.9-mm plastic shells (2- to 10- μm wall) are mounted on very thin (1- μm -diam) spider silks and filled with D_2 , or DT, via permeation at 300 K, to a pressure of 1000 atm. The targets are subsequently cooled to 20 K, where the gas pressure is <1 atm, and transferred individually at cryogenic temperatures to portable equipment that contains the functionality to form the ice layer (60 to 100 μm thick) shown schematically in Fig. 114.1. Those aspects of the process

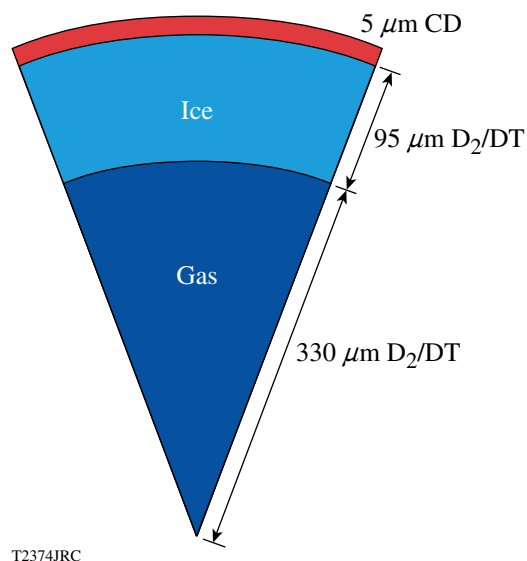


Figure 114.1
Schematic of an OMEGA-scale cryogenic target.

that relate directly to the quality of the ice layer are expounded upon in more detail in the following sections.

The method used to image and quantify the smoothness of the ice layer has also been reported previously,⁶ but the salient points are summarized because they are relevant to this discussion. The cryogenic target is rotated around its north–south axis and is viewed by two cameras elevated 12° and 26° above the equator and displaced 100° azimuthally. These viewing angles are defined by the pre-existing viewing angles for the OMEGA target chamber. Typically an image of the target is acquired for each 15° rotational increment, as shown in Fig. 114.2(a). Two concentric circles are evident—the outer circle is the limb of the plastic capsule and the inner circle corresponds to the interface between the ice layer and the inner gas void. From these images the radial position of the ice and plastic surfaces is measured to better than $1\text{-}\mu\text{m}$ precision. By combining all the images, the center of the sphere can be calculated, and the rms deviation of the measured position of the ice-layer position from the averaged sphere radius is the first estimate of the ice roughness [see Fig. 114.2(b)]. A more precise analysis involves fitting the data to spherical-harmonic coefficients to determine the power in the low ℓ modes ($\ell < 12$) [see Fig. 114.1(c)]. This analysis is inappropriate for quantifying higher-mode roughness because the surface is not uniformly sampled, and the northern and southern poles of the surface ($<6\%$ by area) are not sampled at all. Both conditions are a consequence of the inclined viewing angles of the camera and the rotational axis of the target. These higher modes are determined by averaging the Fourier modes obtained from the individual images. Together, a representative power spectrum is determined for the whole surface.

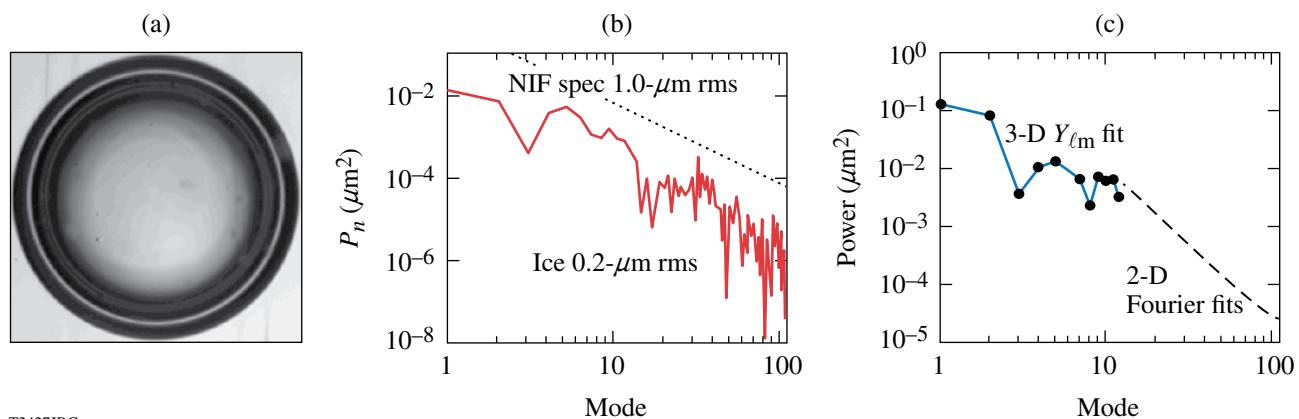
Cryogenic DT Targets

The ice-roughness specification for a NIF cryogenic target is shown in Fig. 114.2(b). This value along with the associated power spectrum presumes that the outer-surface ice layer is substantially smoother than the inner surface, so the roughness value is effectively a measure of the uniformity of the ice wall thickness.

Achieving the roughness specification requires forming a high-quality ice crystal to (1) minimize light scattered within the crystal that degrades the sharpness and continuity of the bright band and affects the accuracy of the shadowgraphic analysis and (2) achieve a constant thermal conductivity throughout the shell. A high-quality crystal is one without any features in the shadowgram image that are either crystallographic dislocations (facets, grain boundaries) within the ice or cracks at the inner surface of the ice, both of which can develop during the crystal growth phase.

1. Seed Crystal and Ice-Layer Formation

Crystal formation involves initially freezing the liquid and then allowing 1 h for the beta-layering process to establish an ice layer, which invariably has a polycrystalline structure. That layer is melted (temperature raised in 0.050-K increments at 1-h intervals) until only a small ice crystal ($<200\text{-}\mu\text{m}$ diam) remains at the north pole, as shown in Fig. 114.3. The temperature ramp is rapidly reversed (lowered 0.08 K in one step) and then lowered 0.02 K at the rate of 0.001 K every ~ 20 min. The time lapse between the decrements is a qualitative judgment that is based on the rate the crystal grows. When the layering process appears to have stalled, the temperature is lowered

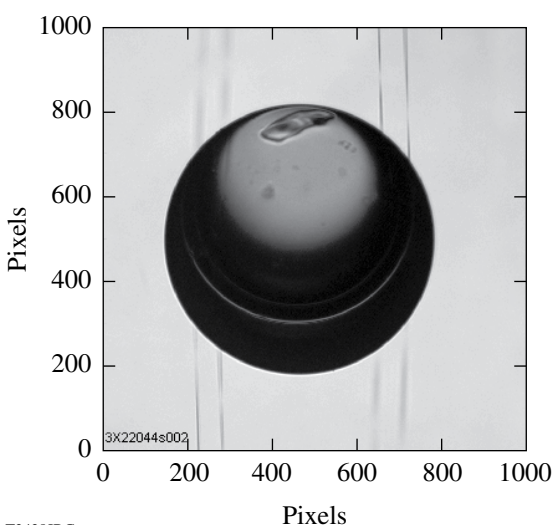


T2427JRC

Figure 114.2

(a) A shadowgraph image of a cryogenic target and (b) the Fourier power spectrum of the ice layer (the dotted line is the specification and the solid line the best recorded result of a single view of the target). (c) The spectral analysis of the 3-D surface is shown using a spherical-harmonic fit for the lower modes and an average of the 2-D Fourier fits for the higher modes.

another 0.02 K at the same rate. Once a contiguous ice layer exists, the temperature is decreased another 0.05 K at a constant rate (1 mK every 30 min), leaving an ice layer that is a single crystal, as shown in Fig. 114.4. Once all the liquid has solidified, the target is cooled another 0.1 K to complete the formation of a uniformly thick ice layer. The timing of the reversal of the temperature ramp is critical: if the seed crystal expands too rapidly, multiple dislocations and grain boundaries will develop



T2428JRC

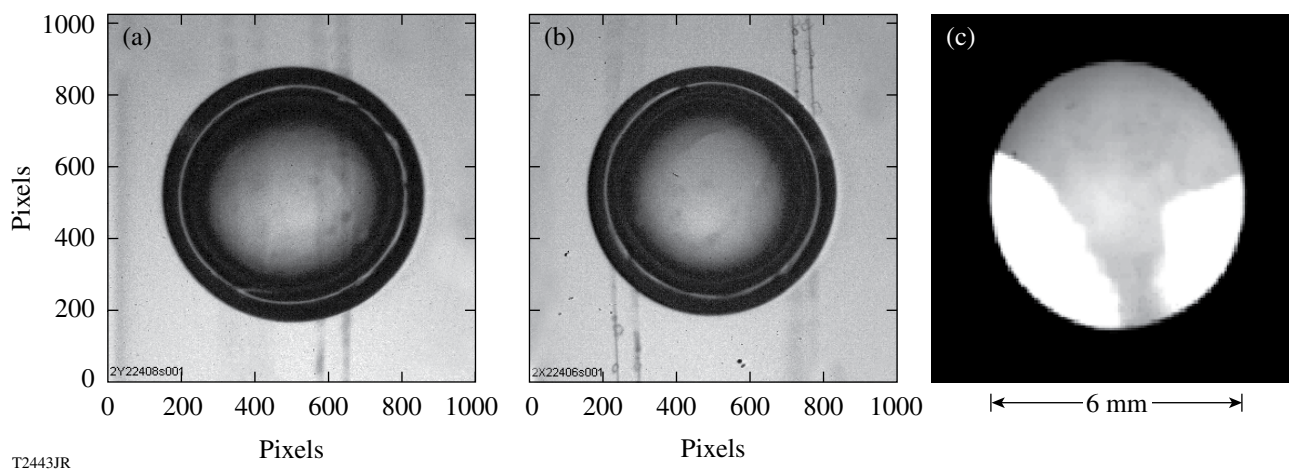
Figure 114.3
A cryogenic target containing liquid DT is shown at the beginning of the crystal formation phase. The small crystal at the top of the target seeds the ice layer.

within the ice; alternatively, reversing the temperature ramp too late will melt the seed crystal because there is a thermal lag between the target and the layering sphere, which is the temperature-controlled surface.

While the protocol described above has been demonstrated to produce a desirable crystal structure, the dynamics of the crystal-growth phase is dependent on the environment around the target, the dimensions of the target and the layering sphere, and the amount of DT inside the capsule. A different protocol will be needed for forming ice layers in NIF-scale targets, especially when using the cryogenic equipment envisioned for the NIF, which requires that targets be filled through fill tubes. In the future, a NIF-scale target will be permeation filled with DT to determine whether the geometry and isothermal characteristics of the present layering sphere are sufficient for achieving the ice-roughness specification for the larger target. Separately, a newly constructed cryogenic system will be used to determine how to process targets possessing a fill tube (see **Future Development**, p. 69). Together, these data will guide the design of the front end of the NIF's Target Insertion Cryostat to field direct-drive targets.

2. DT-Ice-Layer Quality

Since DT cryogenic operations began in 2006, 21 target-filling operations have been undertaken and 39 targets have been produced for implosions and to study the layering process. The average ice roughness of 31 targets studied (without foam ablators) is 1.0 μm (rms) with a range from 0.6 μm to

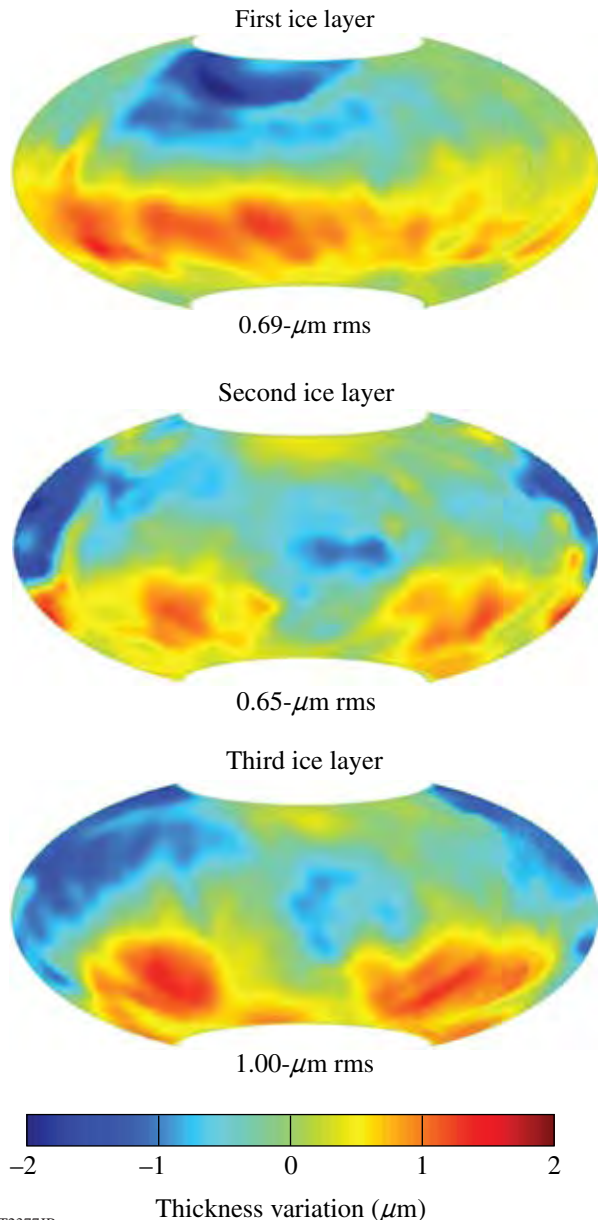


T2443JR

Figure 114.4
Images of the target shown in Fig. 114.3 after layering were acquired using polarized light. The absence of any contrast suggests that the ice layer is composed of a single crystal. Images (a) and (b) are from separate cameras looking at the same target. Image (c) is an ice crystal grown in a cylindrical cell viewed through polarizing optics and showing three separate grains.

2.0 μm . The protocol for forming and then characterizing the ice requires approximately 12 h to complete, and there is a 60% probability that the ice-roughness specification can be achieved within 24 h of receiving the target.

Good repeatability of the layering process was demonstrated by repeatedly melting and re-layering the ice in the same capsule using the same protocol, as shown in Fig. 114.5,



T2377JR

Figure 114.5

The variation in the thickness of three separate ice layers (shown in an Aitoff projection) formed in the same cryogenic target shows the repeatability of the process.

and then repeating this with different capsules. The variation in the ice roughness when the layer was melted and reformed was very small ($<0.4 \mu\text{m}$), and the location of the thicker and thinner regions of the ice in each layer was different after the melt–relayer cycle. The residual roughness present in all of the targets studied showed that there was no statistical correlation between the ice roughness and the plastic capsule or the thermal environment surrounding the target.

3. Fractionation

A consideration when using DT is the possibility that the deuterium and tritium fractions in the fuel will solidify at different temperatures because the heavier isotopes freeze at a slightly higher temperature (pure T_2 at 20.62 K and DT at 19.79 K). We may expect tritium (T_2 and DT) to freeze disproportionately early on during the cooling ramp, leaving excess tritium at the top of the target and closer to the plastic. This effect would be observed as a repeatable thickness variation in the ice (regions with excess tritium would be thinner due to heat generation from the tritium decay). The lack of any pattern in the ice-thickness distribution suggests that any fractionation that may occur is very small or that subsequent solid diffusion may minimize early-time fractionation.

4. Effect of Tritium Decay to ^3He

The decay of tritium to form ^3He can affect both the ice-layer quality and implosion performance. If helium entrapped within the ice has sufficient mobility to agglomerate into bubbles larger than $0.5 \mu\text{m}$, the resulting perturbation will seed instabilities during the implosion.⁷ These larger-sized bubbles may also buckle the ice, adding to the intrinsic roughness. Alternatively, helium that diffuses through the ice into the central void will increase the gas density, and the additional work required to compress the gas during implosions can have a marginal effect on the performance of ignition experiments. While either possibility has an adverse effect, the time scale over which these events occur is important and the data presented here are an attempt to better understand what happens to the ^3He produced.

A cryogenic-DT-ice layer was aged for 19 days at a temperature close (within 0.2 K) to the triple-point temperature (19.79 K). Figures 114.6(a) and 114.6(b) show the ice-layer distribution before and after the aging, respectively. No bubbles or voids were observed. Another set of experiments were performed by lowering the temperature to induce grain boundaries, dislocations, and fractures into an ice layer. Inducing disturbances in the ice is expected to enhance ^3He diffusion and provide voids where the gas could accumulate.

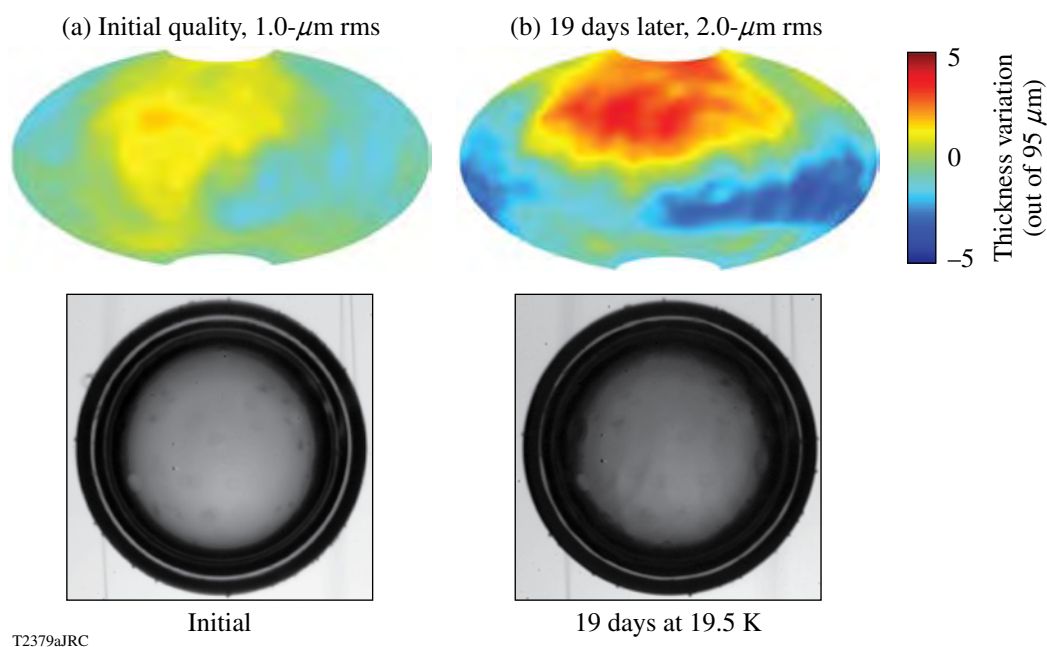


Figure 114.6

Images of a cryogenic DT target and the associated ice-thickness distribution (a) initially and (b) after 19 days.

Moreover, lowering the temperature increases the strain in the ice-crystal structure, which enhances the diffusivity of helium within the crystal.⁸ A cryogenic-DT layer aged for two days at 2 K below the triple point [Fig. 114.7(a)] showed no evidence of bubble formation, but small clusters of voids attributed to ^3He were observed in another cryogenic-DT-ice layer [shown in Figs. 114.7(b) and 114.7 (c)], aged for seven days under the same conditions.

The appearance of bubbles many days after the ice layer was formed, and only when the ice was strained and fractured, suggests that the helium has limited mobility within a DT-ice crystal. The other possibility is that helium is highly mobile within the ice and diffuses rapidly to the center void; that eventuality would require helium atoms to be more mobile in defect-free, unstrained ice, which is counter to the observations and the general understanding of how gases diffuse through crystalline structures.⁸

Helium has very low solubility in hydrogen ice,⁹ and the size of the helium atom (0.3 Å) relative to the open structure of the DT-ice crystal (hexagonally close-packed structure with a 2.2-Å interstitial radius) is expected to allow rapid diffusion. However, there are data that may support the notion that helium is effectively trapped in the ice, which would be very desirable since the unavoidable decay of tritium may not have the deleterious effect on the ICF implosion described at the beginning of the

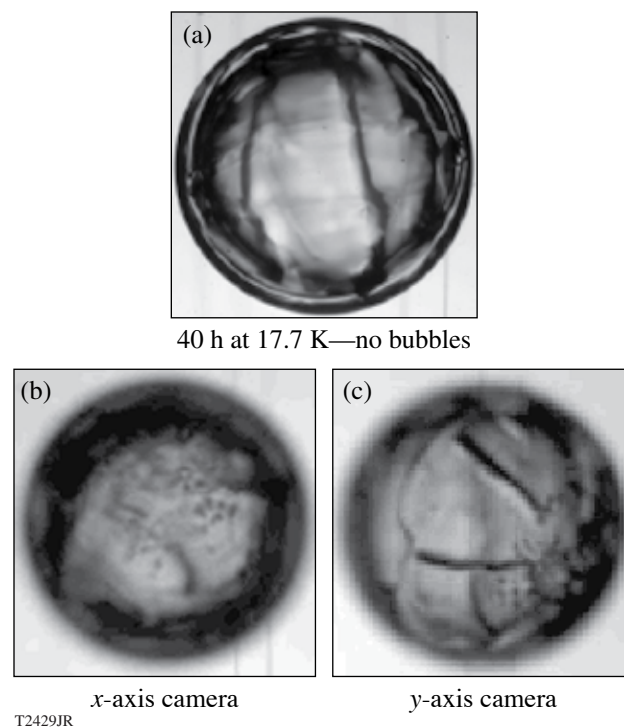


Figure 114.7

(a) A fresh DT-ice layer was cooled 2 K below the formation temperature and aged for two days. (b) and (c) When aged for seven days, 2 K below the formation temperature, black spots presumed to be ^3He bubbles were observed.

section. The decay product of tritium is a (${}^3\text{HeD}$)⁺ or (${}^3\text{HeT}$)⁺ ion (Ref. 10) that initially remains bonded to neighboring DT, D₂, or T₂ molecules in the lattice. A fraction of these ions will be neutralized by the electrons produced by the decay of nearby tritium atoms (which have a range of $\sim 0.6 \mu\text{m}$ in the ice), and then dissociate into ${}^3\text{He}$ and T or D atoms. The latter two atoms rapidly recombine and are re-adsorbed into the lattice. The remainder of the ${}^3\text{HeT}^+$ (and ${}^3\text{HeD}^+$) ions may become incorporated into the lattice at interstitial octahedral sites and unable to migrate.¹⁰ Experimental evidence for this eventuality is from muon-catalyzed fusion studies¹¹ that measure the time-dependent change of the fusion–neutron disappearance rate in ice and liquid-DT mixtures. The disparity in the neutron disappearance rate between the liquid (where there was no change) and ice (where the change increased with time) was attributed to the accumulation of ${}^3\text{He}$ within the ice lattice.¹¹

To provide a scale to the helium production rate, approximately 10^{10} ${}^3\text{He}$ atoms are produced per second in the 0.18-mm^3 ice volume of an OMEGA-scale target; that equates to $\sim 5 \times 10^4$ He atom/s in every $10\text{-}\mu\text{m}^3$ voxel, which collectively would form a $0.1\text{-}\mu\text{m}$ -diam bubble every second. The $10\text{-}\mu\text{m}$ scale length was chosen to reflect the limited diffusion path of helium atoms and is based on the range of β electrons in the ice to neutralize ionic species into more-mobile neutral atoms. After 19 days, 1.6×10^{16} helium atoms would have been produced and bubbles that are clearly visible would be expected. (The size of the bubble depends on the Laplace pressure and permeability of the ice.) As observed, there were fewer than 10^3 bubbles (with a less than $10\text{-}\mu\text{m}$ -diam size) after the ice was aged for seven days, and then only when the ice was faceted and strained. The most likely inference from all the data is that He has limited mobility. Because this inference has far-reaching implications for the acceptable “shelf-life” of a DT-ice layer, this interpretation needs to be supported with direct measurements of the diffusivity of the ${}^3\text{He}$ by-product of tritium decay through hydrogenic ice.

What was noticeable in the DT target that had been allowed to age [see Fig. 114.7] was the progressive deterioration in the quality of the ice layer. Interestingly, the power in the added roughness was in the lower Legendre modes ($\ell < 10$). This phenomenon is attributed to the constant rearrangement of the DT structure caused by the high-energy β -decay electrons breaking and reforming the crystal bonding structure. Approximately 10^{10} tritium atoms disintegrate every second in an OMEGA-scale DT target, produces high-energy electrons (up to 18 keV) with each electron capable of rupturing up to 10^5 molecular bonds that hold the lattice together. Clearly these

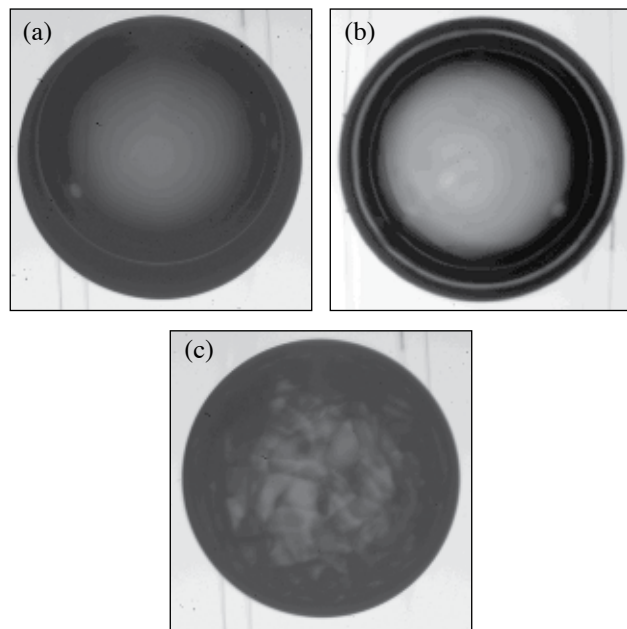
bonds reform rapidly, as the lattice remains intact, but this constant realignment of the crystal will allow for sizeable diffusivity of deuterium and tritium through the lattice and, with time, a possible re-ordering, or fractionation, of the isotopes. If, due to gravity, the heavier tritium atoms diffuse away from the north pole, the resulting lower volumetric heating there would make the ice thicker—which is what was observed. Not only would this increase the rms roughness of the ice but it would also create a variable areal density around the target that would affect the dynamics of the implosion.

5. DT-Ice Layers in Foam Ablator Targets

Efforts to characterize ice layers formed in foam targets using the same protocol that worked for standard plastic ablaters were unsuccessful because the resulting ice/foam layer was opaque and the ice/gas interface could not be imaged. Although the foam alone was transparent (it possesses a small pore size, $< 0.2 \mu\text{m}$) and remained transparent when filled with liquid, the target became opaque once the ice layer formed. The transparency was improved by minimizing the number of freeze/melt cycles and not cooling the target below 18 K. This minimized mechanical damage to the foam structure (maintained the pore sizes) from the shear forces that develop due to the different densities of the ice and liquid phases.¹²

It remains critically important to form the ice layer slowly in order to preserve the single-crystal structure of the ice. The presence of the foam does not appear to change how the layer grows provided that the process proceeds in a sufficiently controlled manner with a stable and gradual temperature ramp. This greater sensitivity to the cooling rate compared to non-foam targets is presumed to be due to the viscous drag that the foam has on the movement of the liquid. If the target is cooled too rapidly, the liquid does not have enough time to move to the ice/liquid interface (the void that can develop there is caused by the density mismatch), and the liquid can nucleate a crystal at a foam filament rather than attaching to the existing crystal, which results in a higher void content and greater opacity. At the extreme—flash freezing the target—there is a 13% decrease in the molar volume of DT due to the phase change and the ice turns instantly opaque. The transparency improves marginally as the layering mechanism functions to redistribute and densify the ice, but the resulting small-grain polycrystalline structure cannot be annealed into a single crystal and the inner ice surface cannot be imaged using shadowgraphy. Figure 114.8 shows a series of images of a DT-filled foam target containing initially (a) liquid and then an ice layer formed slowly (b) or rapidly (c). The quality of the ice layer when properly formed is approaching what is achievable in non-foam DT targets: 0.9- to

2.6- μm rms. Current development is directed at understanding how imperfections and variability in the foam structure affect the quality of the ice layer and the ability to characterize it.



T2430JR

Figure 114.8

DT in a foam target (840- μm diameter; 0.5- μm -rms outer surface roughness; 0.73- μm -rms inner foam layer roughness; 47- μm -rms inner foam layer thickness): (a) liquid DT, (b) single-crystal ice layer, 54 μm thick, 1.2- μm rms, (c) rapidly cooled polycrystalline ice layer.

6. DT-Gas Density at Implosion

A special challenge with DT targets is to preserve the ice layer when the shrouds are retracted to shoot the target. A complication arises because the helium gas that surrounds the target to remove the heat from the target must be removed prior to the shrouds retracting, and its elimination results in the target warming. While the shroud retraction process can be extremely rapid⁵ (<1 s total with the target exposed to ambient radiation for <60 ms), slower shroud retraction rates are used to allow more time for the mechanical impulses from the retraction process to attenuate in order to minimize target vibration. Currently there is a 6-s time lapse between the helium gas being exhausted and the target being imploded. During this time the temperature of the ice rises from 19.4 K to 19.7 K (the triple-point temperature). If the target is not initially sufficiently cold, the ice will begin to melt.

Cryogenic D₂ Targets

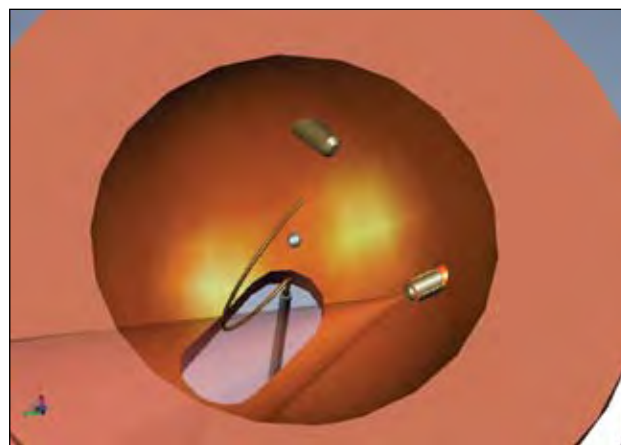
Despite the success in providing DT cryogenic targets that meet ice-roughness specifications, D₂ targets are still required for implosion experiments to measure the areal density generated

in the implosion³ and to support additional cryogenic implosion experiments as the radiological issues associated with handling tritium complicates and slows the production of DT cryogenic targets. The best D₂-ice layers produced so far are approaching the quality typically achieved in DT targets, but the process is subject to more variability. Improving D₂ target layering has been a high priority and is described in this section.

Recent experiments with D₂ cryogenic targets and the experience with DT targets, which provides a benchmark for comparison, strongly suggest that ice-roughness variation in D₂ targets is caused by (1) nonuniform volumetric heating of the target and (2) the target-support structure distorting the spherical isotherms around the target. A surprising sensitivity of the ice roughness to even small thermal perturbations around the target has been observed. The sources of these perturbations must be identified and eliminated to reliably produce high-quality D₂ targets.

Lacking the intrinsic beta-decay heating method of tritium, volumetric heating of deuterium targets is achieved by irradiating the target with mid-infrared (mid-IR) light at the wavelength of a strong D₂ absorption resonance (3.16 μm) (Ref. 13). Uniform illumination is essential to achieve uniform volumetric heating required for high-quality ice layers, so the D₂ targets are located at the center of an integrating sphere that also sets the spherical isotherms.

Figure 114.9 shows a schematic of the “layering sphere.” Mid-IR light is introduced by an optical fiber so that it does



T2431JRC

Figure 114.9

A schematic of the lower hemisphere of the layering sphere showing the target mounted on the beryllium “C” support and two IR fibers projecting into the sphere. The cone of light from one of the fibers is projected and shown to intersect the beryllium support.

not directly illuminate the target. The inner surface of the layering sphere is deliberately roughened and coated with gold to provide a highly reflective scattering surface. Ideally, this scattering would be isotropic and would uniformly illuminate the target after a few bounces. Subsequent experiments showed that the surface forward scatters the light with a $\cos^9\theta$ angular distribution.¹⁴

Another limitation to forming high-quality D_2 -ice layers is the nonuniform thermal environment surrounding the target. Mid-IR light absorbed by the target support, the plastic ablator, and the glue used to hold the target perturbs the spherical isotherms sufficiently to exceed the $1\text{-}\mu\text{m}$ -rms-roughness specification. Efforts to mitigate these effects have improved the ice-layer quality and are presented here.

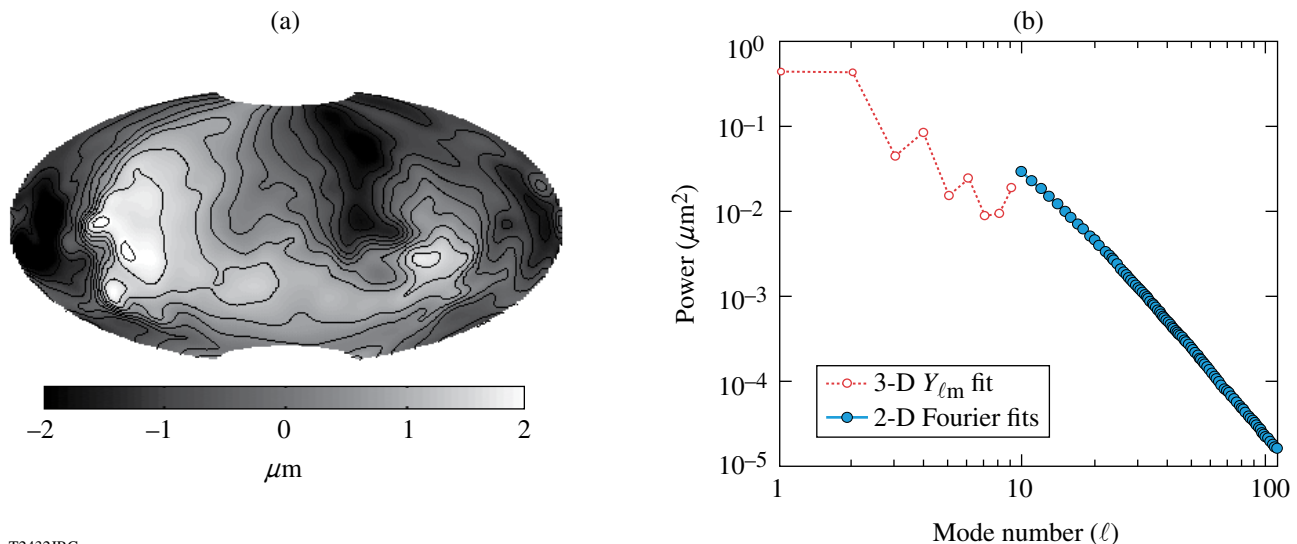
The result of these efforts produced a D_2 -ice layer with an rms roughness of $1.1\ \mu\text{m}$. This best D_2 -ice layer, shown in Fig. 114.10, was achieved in a layering sphere that had received all the upgrades described in subsequent sections. Importantly, this good quality was not an isolated event; similar targets that were layered using the same protocol achieved ice layers that ranged from 1.5- to $2.5\text{-}\mu\text{m}$ rms roughness, considerably better than the historical 3- to $5\text{-}\mu\text{m}$ rms roughness. A necessary requirement for improved ice smoothness is the plastic capsule itself, specifically, the thinness of the walls ($2.0\ \mu\text{m}$ —the thinnest requested) and the composition of the plastic (low oxygen

content) because this reduces the sensitivity of the target to nonuniform illumination.

1. Effect of IR Heating on Ice-Layer Quality

The strongest absorption bands in D_2 correspond to the $Q_1(1)+S_0(0)$ and $Q_1(0)+S_0(0)$ transitions that overlap at $3.16\ \mu\text{m}$ and have a combined 10-nm bandwidth.¹³ The $Q_1(1)$ and $Q_1(0)$ components of the absorption band are due to vibration-only transitions in ortho- and para-deuterium, respectively, while the $S_0(0)$ component is a rotation-only transition. Absorption is due to a dipole moment induced by motion in two neighboring D_2 molecules, where one molecule rotates (change in the rotational quantum number, $\Delta J = 2$) and the other vibrates (change in the vibrational quantum, $\Delta v = 1$). The absorption band possesses fine structure that varies according to the ratio of ortho- and para-deuterium (deuterium is 67% ortho and 33% para). The absorption coefficient is $4\ \text{cm}^{-1}$, corresponding to $\sim 7\%$ of the incident IR power being absorbed by the ice in a standard OMEGA-scale cryogenic target.

The current IR layering source is a tunable optical parametric oscillator (OPO)¹⁵ with a bandwidth (0.03 to $0.3\ \text{nm}$) that is narrow compared to the D_2 absorption band.¹³ The wavelength of the OPO can be adjusted in 10-nm steps that are comparable to the bandwidth of the strongest D_2 absorption band at $3.16\ \mu\text{m}$. This combination of narrow OPO bandwidth and coarse tuning can result in the output wavelength being offset



T2432JRC

Figure 114.10

(a) The variation in the thickness of a $99\text{-}\mu\text{m}$ deuterium ice layer ($860\text{-}\mu\text{m}$ -diam, $2.0\text{-}\mu\text{m}$ wall capsule) is shown (b) with the associated power spectrum for the entire surface. The rms roughness value for all modes is $1.1\ \mu\text{m}$.

from the deuterium absorption peak, which would reduce the heat deposited in the ice and make the volumetric heating very dependent on the spectral stability of the OPO. The stability of the wavelength depends on the temperature stability of the lithium niobate crystal in the OPO, where a 5°C change corresponds to a 1-nm change in wavelength. The wavelength is not locked to a specific value; instead, the temperature of the crystal is closed-loop controlled using a chromel–alumel thermocouple. Consequently the spectral output depends on how well the crystal is thermally connected to the temperature sensor, the standard error limits of the sensor (2.2°C), the bandwidth on the temperature control circuit logic (2°C), and the sensitivity of the temperature measurement (a millivolt thermocouple signal) to external noise.

OPO output power and wavelength must both be stable since both affect the volumetric heat load during the initial crystal growth phase (15-min duration), and the rate of growth of the crystal determines whether single, or multiple, crystals form, and the presence of facets and low-angle grain boundaries in an ice layer with multiple crystals increases the ice roughness.

Once the layer is formed and the target is transported to the OMEGA target chamber, small drifts in wavelength and power may result in the ice layer melting (a 1% change in OPO power will slump the ice layer in 30 min).

The effect of OPO wavelength on ice-layer quality was determined by forming a layer at one wavelength and at maximum OPO output power and then changing the wavelength. The data are shown in Figs. 114.11 and 114.12. Operating the OPO wavelength closer to the peak of the D₂ absorption band produces targets with lower roughness. At wavelengths where D₂ does not absorb (3.15 and 3.21 μm), there is sufficient heat absorbed in the plastic to form a thermal gradient sufficient to give a rudimentary ice layer. These layers possess a dominant vertical P₁ mode that is symptomatic of insufficient heat being coupled into the ice. Separate experiments in which the power of the OPO was deliberately varied show that a minimum of 3 μW must be absorbed in the ice to form a uniformly thick ice layer. Higher heat loads in the target increase the speed at which a layer forms but only marginally improves the ice roughness. It has been impossible to explore the benefit of high

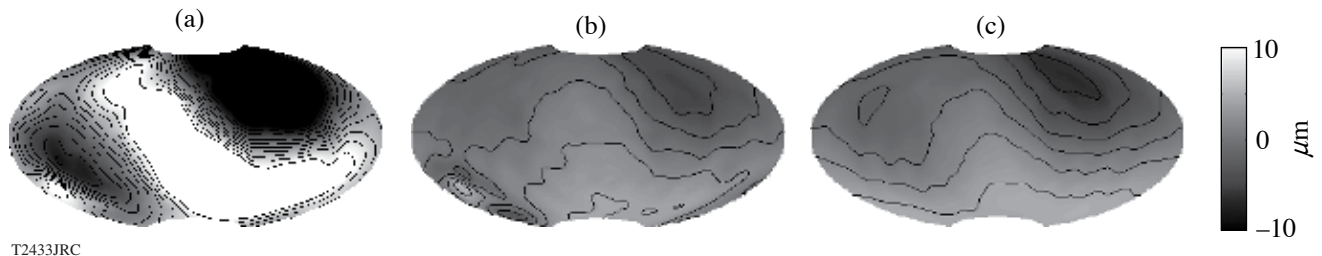


Figure 114.11 Variation in the thickness of the ice layer when just the wavelength of the optical parametric oscillators (OPO's) is varied: (a) $\lambda = 3.21 \mu\text{m}$, roughness is 10.5- μm rms; (b) $\lambda = 3.17 \mu\text{m}$, roughness is 2.4- μm rms; (c) $\lambda = 3.16 \mu\text{m}$, roughness is 3.0- μm rms,

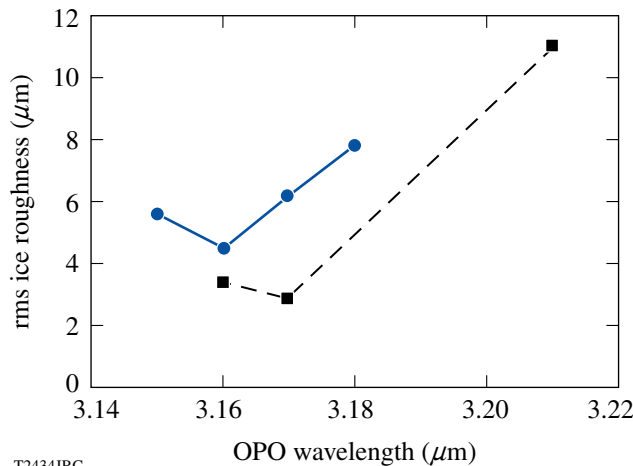


Figure 114.12 The dependency of ice roughness on the wavelength of the IR source is shown for two OPO's. The variability in roughness depends on whether sufficient heat is coupled into the ice layer to complete the layering process. The output power of the OPO's was constant.

IR power because the maximum power that can be achieved in the ice is $\sim 20 \mu\text{W}$, which is twice the heat from beta decay in a comparably sized DT target.

2. IR Illumination Uniformity

From the beginning the importance of uniform IR illumination throughout the layering sphere was recognized, so the surface of the layering sphere was treated to provide Lambertian reflectance.¹⁶ The observed behavior of the D_2 (and not DT) ice layers questioned that assumption of Lambertian reflectance, and tests of the layering sphere showed that the surface has a preferred forward scattering angle. Subsequent ray-trace modeling¹⁷ showed large regions of the layering sphere volume where the IR intensity is substantially greater than elsewhere (see Fig. 114.13). A portion of these regions overlap the beryllium support, which is 22 mm long with a 7-mm radius of curvature and intersects a large portion of the cross-sectional area of the void in the layering sphere. The heat deposited in the beryllium structure perturbs the spherical isothermal structure around the target and, depending on how hot the beryllium becomes, determines how it will affect the ice (see **Effect of the Target Support on the Ice-Layer Quality**, p. 68).

IR uniformity was improved by adding a diffusive reflector in front of the injection fiber to scatter the incident beam (5 to 20 mW) over a larger fraction of the layering-sphere surface and reduce the intensity of each subsequent reflection. This successfully eliminated the thermal influence of the beryllium support on the ice layer, but the new

IR illumination pattern introduced a different and smaller perturbation to the ice layer that suggests that the target is no longer being uniformly illuminated—it appears that one of the multiple initial reflections of the beams is striking the target directly. This conclusion was reached by rotating the target and seeing the same ice-distribution pattern in the ice layer relative to the surface of the layering sphere regardless of the rotational position of the capsule. A similar ice distribution pattern is observed, at different magnitudes, in all the moving cryostats that were retrofitted with this modification to the IR injection fiber.

To estimate the ice layer's sensitivity to nonuniform illumination a finite-volume thermal calculation (*FLUENT*¹⁸) applied a 20%-larger volumetric heating load over two opposing sides of the target that total 14% of the target's volume. That non-uniformity redistributed the ice and the resulting roughness was 17- μm rms. The pattern of roughness and distribution of power in the low Fourier modes was similar to experimentally observed ice layers (see Fig. 114.14), which shows that the ice layer is very sensitive to illumination uniformity.

3. Effect of the Plastic Ablator's Composition on the Ice Layer

The effect of nonuniform IR illumination on the ice roughness is compounded if appreciable light is absorbed by the ablator. If the heat absorbed in the plastic is uniform, the main effect is to increase the temperature difference between the layering sphere and the target; however, as the ratio of heat in the plastic relative to the heat required to form an ice layer

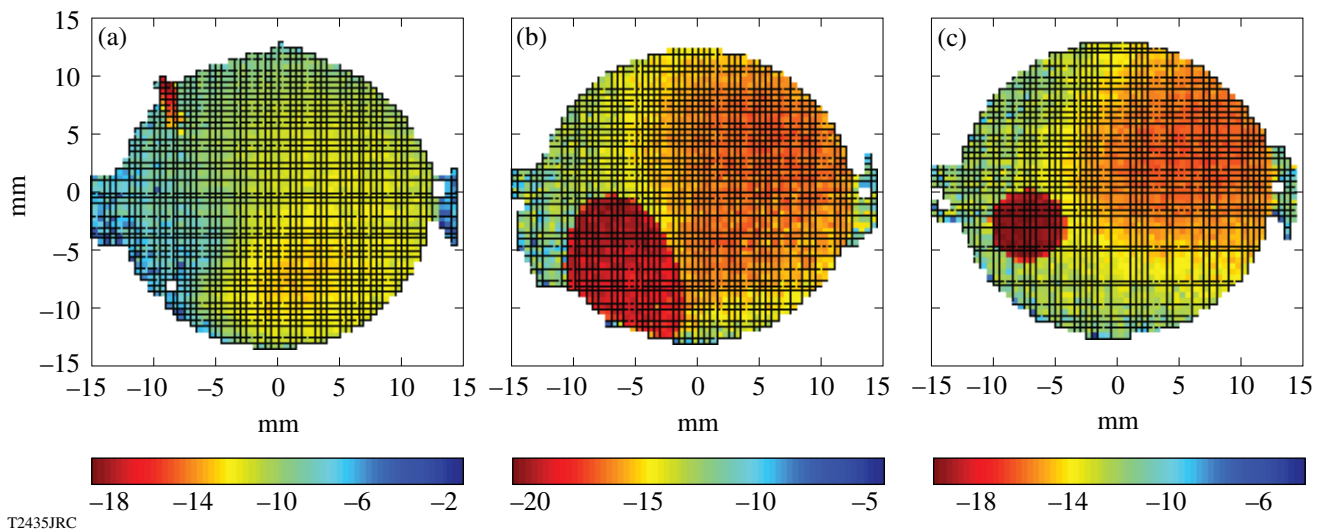


Figure 114.13

Calculated IR intensity distribution patterns shown in a logarithmic plot for discrete vertical planes through the layering sphere (a) 0° , (b) 60° , and (c) 120° (angles refer to OMEGA coordinates).

($\sim 3 \mu\text{W}$, or $1/3 Q_{DT}$) increases and is not uniform throughout the plastic, the distortion to the spherical uniformity of the isotherms around the target increases.

The plastic ablator strongly absorbs IR light over the wavelength range of 2.85 to $3.4 \mu\text{m}$, which includes the deuterium

absorption band at $3.16 \mu\text{m}$. This absorption increases with time, as shown in Fig. 114.15(a), due to the uptake of ambient moisture and oxygen that become chemically bonded in the plastic as a hydroxyl molecule.¹⁹ The absorption coefficient increases markedly when a silicon dopant is added to the ablator, as shown in Fig. 114.15(b) (Ref. 20).

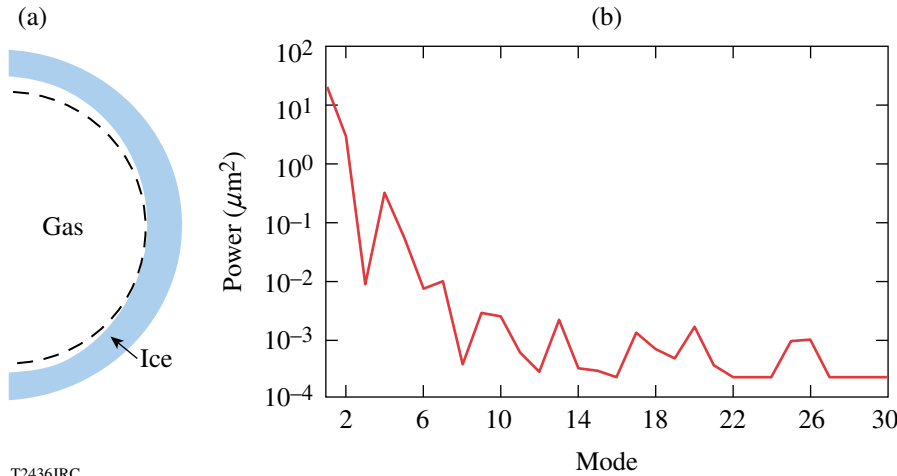


Figure 114.14
The calculated effect of 20% illumination nonuniformity on the ice-thickness distribution for a large volumetric heat load over a 14% volume at the north and south poles. (a) The ice is thinner at the poles (dashed line is a surface of constant radius for reference). (b) The Fourier power spectrum shows that the low-mode roughness (P1 through P4) is the greatest. The shape of the PSD is comparable to measured ice layers but the magnitude is $\sim 50\%$ larger.

T2436JRC

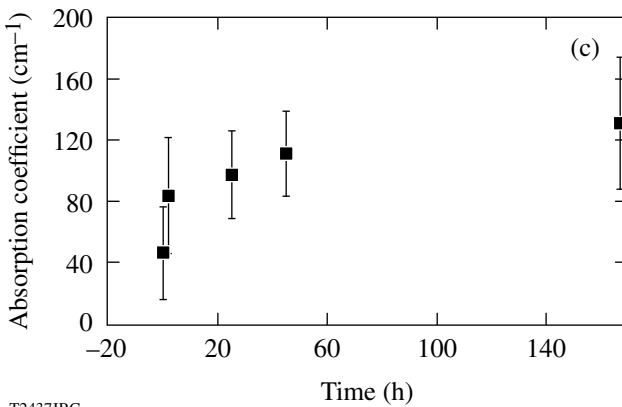
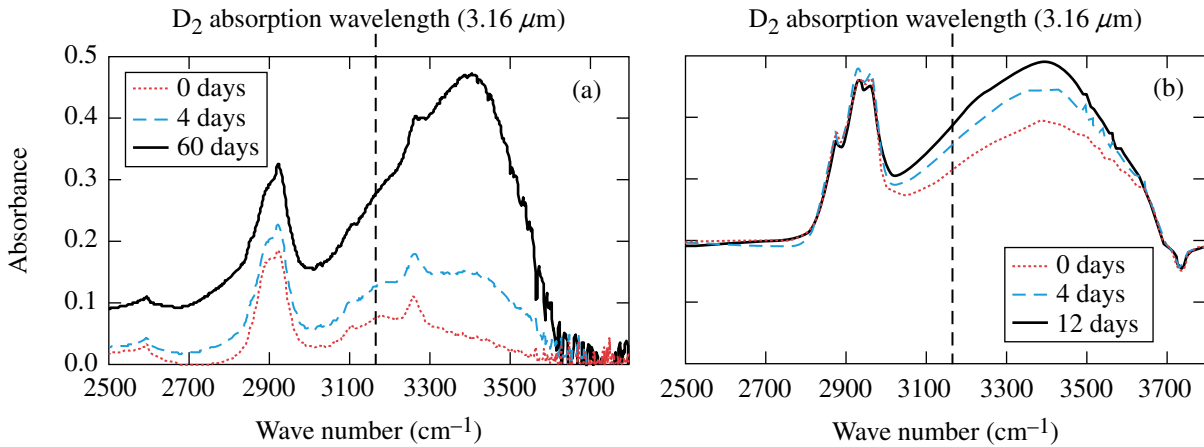


Figure 114.15
(a) Infrared absorption spectrum of an $8\text{-}\mu\text{m}$ -thick carbon-deuterium plastic film. The spectrum overlaps the solid-deuterium spectrum and absorption increases with time due to the adsorption of moisture. (b) Adding silicon (6 at.%) to a $1.5\text{-}\mu\text{m}$ -thick plastic film increased the IR absorption. (c) The absorption coefficient of a silicon-doped plastic shell ($5\text{-}\mu\text{m}$ wall, 6-at.% silicon) increases steadily with time.²⁰

T2437JRC

The absorption coefficient of a standard plastic capsule is 5 to 26 cm^{-1} (one to six times that for D_2) as fabricated and increases to 16 cm^{-1} and 35 cm^{-1} after 4 and 60 days, respectively.^{19,20} Absorption is due to the presence of the hydroxyl ($-\text{OH}$) species that possess a strong dipole moment that allows them to effectively absorb radiation. These species derive from the adsorption of moisture, or in the case of silicon-doped plastic, from the reaction of silicon free radicals present in the polymer with atmospheric oxygen. Free radicals within the plastic result from the plasma polymerization process. The presence of silicon in the CH ablator increases the absorption coefficient by a variable amount, depending on the fabrication conditions, up to a maximum measured value of $\sim 6000 \text{ cm}^{-1}$, where 95% of the IR light is absorbed by the plastic ablator, effectively shielding the ice from the IR source. The problem with the presence of high-reactive silicon atoms was mitigated by heating the plastic to 300°C immediately following fabrication. Heat treatment reduces the number of reactive sites in the plastic, and the measured absorption coefficients were reduced to ~ 40 to 140 cm^{-1} , depending on how long the capsules are exposed to the atmosphere [Fig. 114.15(c)]. Currently there remains a sizeable variability in the magnitude of the absorption coefficient of the plastic.

The effect of the enhanced IR absorption in the plastic ablator on the ice-layer roughness is two-fold: (1) If the ablator absorbs the light so effectively that too little heat is absorbed in the ice, then insufficient heat density is available to drive the layering process, resulting in a roughness of $\sim 10\text{-}\mu\text{m}$ rms, as seen in Fig. 114.16(a). This behavior was also observed in deuterium-tritium targets with a low (0.1 and 1 at.%) tritium content where the heat from tritium decay was insufficient to form a symmetrical ice layer, as well as when the OPO wavelength was detuned

from the D_2 absorption maximum. Heat treating significantly improved the silicon-doped target ($2.5\text{-}\mu\text{m}$ rms) ice roughness [Figure 114.16(b)]. (2) If the ablator is not uniformly thick, or the IR illumination is not uniform over the surface of the target, the variable volumetric heating load will be accentuated by a high absorption in the plastic and will degrade the uniformity of the ice layer. Since the thickness of the plastic wall is measured interferometrically to vary less than $0.2 \mu\text{m}$, illumination uniformity is the greatest concern. Figure 114.16(c) shows a silicon-doped target with two opposing regions of thinner ice that is presumed to be caused by a higher IR flux illuminating the target along this direction.

4. Effect of the Target Support on Ice-Layer Quality

The target is attached to four spider silks ($<1\text{-}\mu\text{m}$ diam) on a beryllium wire ($250\text{-}\mu\text{m}$ diam) that is bent into a semicircle (7-mm radius). The beryllium wire was shown in earlier experiments²¹ to affect the ice layer: the thinnest region of the ice faced the beryllium support and this correlation was maintained when the target was rotated in the layering sphere, and when different targets were used. The cause was the beryllium support absorbing IR light, as shown in Fig. 114.9, and heat from the hot wire imprinting into the ice. Conclusive proof of the IR-induced heating effect of the beryllium is the absence of any similar imprint in DT-ice layers for targets that use the same support structure.

Glue is used to attach the capsule to the spider silk. Manipulating extremely small quantities of glue is difficult as surface tension rapidly wicks the glue from the dispenser to the surface. The glue strongly absorbs IR light and becomes a localized heat source on the capsule. To test the effect, a capsule was mounted in silk and four glue spots of different sizes were

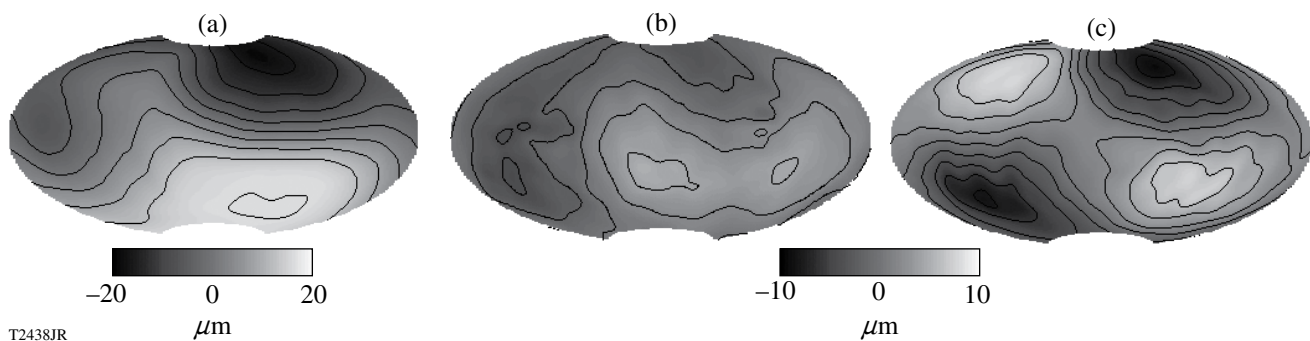


Figure 114.16

D_2 -ice thickness distribution in a silicon-doped plastic capsule. A large P1 vertical mode is present when (a) the capsule is not heat treated to minimize adsorption of water ($10\text{-}\mu\text{m}$ rms) and is reduced when (b) the capsule is heat treated ($2.5\text{-}\mu\text{m}$ rms). (c) A third target shows two opposing thin regions of ice that lie on an inclined axis (30° from north and 50° azimuthally, in OMEGA coordinates), which suggests that the target is more strongly illuminated along this axis.

applied, as shown in Fig. 114.17. Glue spots smaller than 30- μm diam and 3 μm high (<1 ng) did not affect the ice, whereas a glue spot \sim 100- μm diam and 7 μm high (47 ng) generated a 20- μm -deep hole in the ice and a 26-ng glue spot generated a 10- μm -deep crater. The two smallest glue spots had no observable effect on the ice layer. An alternative to using glue is to overcoat the target and silks with a thin film of parylene less than 1 μm thick. The capsule is held without glue between four silks during the vapor-deposition process. Experience shows that this satisfactorily supports the capsule and eliminates the need for glue.

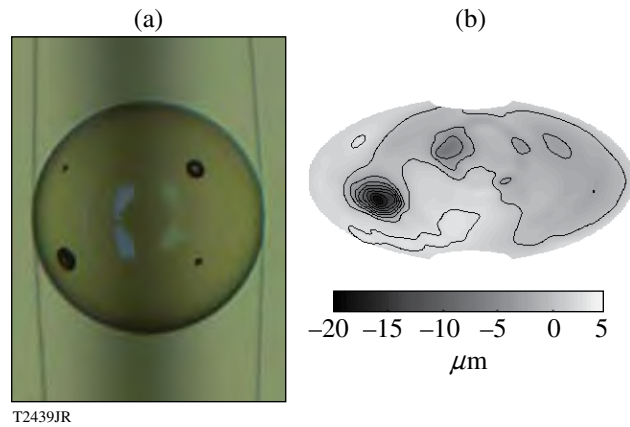


Figure 114.17
(a) A target is shown mounted on silk with four glue spots of varying size. Starting in the top left-hand corner and proceeding clockwise, they have masses of <1, 26, 1, and 47 ng. (b) The variation in the thickness of a 95- μm ice layer is shown as an Aitoff projection. The 47-ng glue mass (height of the glue is 7 μm) causes a 20- μm crater. Diagonally opposite this feature is a 10- μm crater caused by the 26-ng glue spot. The smaller glue masses had no effect.

5. Current Status

Smooth D_2 -ice layers are feasible when sufficient heat is deposited in the ice, minimal heat is deposited in the plastic ablator, and the target is uniformly illuminated. We have no diagnostic to evaluate these phenomena that is more sensitive to these effects than the target itself. So only by accumulating statistics of the ice layer for different targets and layering-sphere environments is it possible to evaluate and improve the performance of cryogenic equipment for producing high-quality ice layers. Anytime one of the critical components is changed, the performance of the equipment can change, and it requires over a month to reestablish the performance of the system. These critical components are the IR injection fiber, the layering sphere, and the target type (wall thickness, ablator composition). Currently there is one moving cryostat that produces good-quality ice layers and two cryostats that produce

moderate-quality layers. A concerted effort is underway to improve the design of a reflective optic for the injection fiber to improve the uniformity of IR illumination. Such a device should improve the repeatability of the layer quality in all the moving cryostats used for implosion experiments.

Future Development

1. Achieving 0.3-mg/cc Gas Density in a Cryogenic Target

Experience shows that the ice-roughness specification can be achieved only by forming the ice layer at the triple point (0.5 mg/cc at 19.7 K for DT). Implosions performed using a low-adiabat ($\alpha < 2$) laser pulse shape would benefit by lowering the gas density to 0.3 mg/cc, which corresponds to a temperature of 18 K for DT.²² The consequence of cooling the target by the required 1.7 K raises the density of the ice by 0.8%, which induces a strain of 0.1% along the a axis and 0.2% along the c axis of the hexagonally closed packed crystal. This strain exceeds the yield stress¹² and plastically deforms the ice.

Experiments reported that this behavior can be minimized by rapidly cooling the ice layer, thereby creating a brief “time window” where the gas has the desired density (0.3 mg) and the ice-layer smoothness is preserved.²³ Repeating those experiments here with the OMEGA Cryogenic System suggests that the solution is not so straightforward. Rapidly cooling a target with a thick ablator wall (10 μm) and a 95- μm D_2 -ice layer showed that a 10-s period existed during which the ice layer retained its roughness and the temperature was 1.7 K below the triple-point temperature, as seen in Fig. 114.18(a). The temperature of the target is calculated from the measured temperature of the layering sphere and the thermal diffusivity of helium. The heat capacity and heats of fusion and sublimation of the D_2 ice were included in the analysis.

Repeating this experiment with targets with thinner plastic ablators (2 to 5 μm) produced contradictory data. Features and roughness were observed in the ice once the temperature had dropped 1 K, as shown in Fig. 114.18(b). Sometimes the increased roughness was observed along only one viewing axis; other times the outer plastic surface roughened while the ice layer retained its smoothness. This observation confirms that the stresses induced when the ice contracts are substantial, as witnessed by the plastic and/or ice buckling. This raises the question of why targets with thicker plastic ablators did not show as rapid a degradation of ice quality as the targets with thinner ablators since the stresses should be similar. One possible explanation is that the ice layer may detach from the thicker plastic walls because the plastic is less likely to buckle to relieve the stress; the resulting higher thermal resistance

between the wall and ice layer may cause the actual temperature of the ice and gas to be higher than calculated.

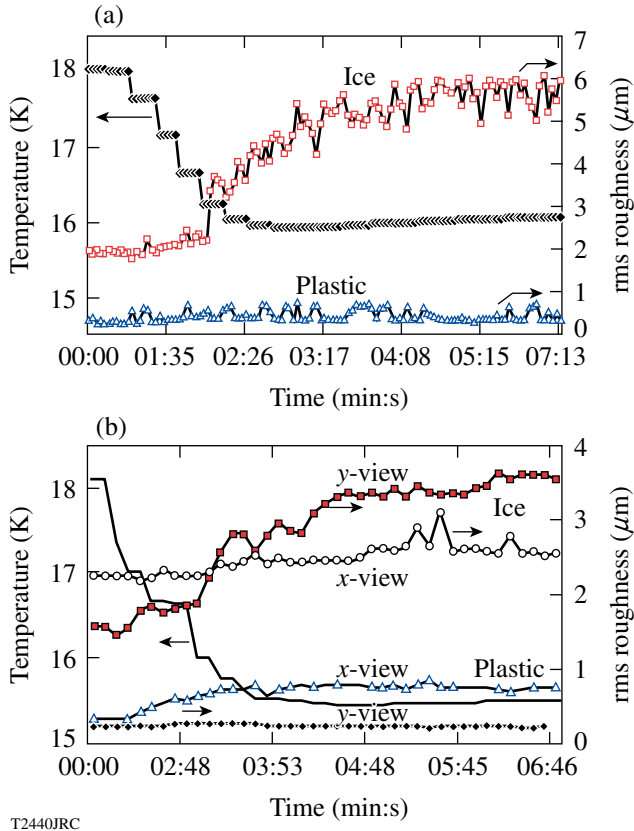


Figure 114.18 (a) Rapidly cooling a target with a 10- μm plastic wall shows that there is little change in the ice roughness until the temperature is 1.7 K below the triple point. Simultaneously there is no change in the roughness of the plastic ablator. In contrast, (b) rapidly cooling a thinner-wall (5 μm) capsule shows the ice roughness increased in one camera view and not the other. Concomitantly, the roughness of the plastic ablator increased in the camera view where the ice did not roughen and visa versa.

Current experience requires that we assume that dislocations and grain boundaries will develop in the ice as it cools and before it is imploded. What needs to be resolved is whether these features are crystallographic fractures within the ice or cracks at the inner ice surface. If they are the former, they would have nanometer scale lengths and would not be expected to affect the implosion; if they are the latter, they could affect the implosion if the total void volume due to the cracks were large. The current NIF specification for indirect-drive targets is that the void-volume in the cracks be less than 0.2% of the total ice volume. The features that form when the target is rapidly cooled appear circumferentially around portions of the target in discrete regions, as shown in Fig. 114.19, that appear to be correlated to a crystalline axis. Should there be a strong correlation between the

position and direction of these features and the crystallographic axis, then it is reasonable to assume that the features are a benign facet or low-angle grain boundary rather than a larger-scale crack at the inner ice surface. Current emphasis is to acquire those statistics to see if there is a correlation between the orientation of the growth crystal as determined from the solidification process and the fracture features observed during cooling.

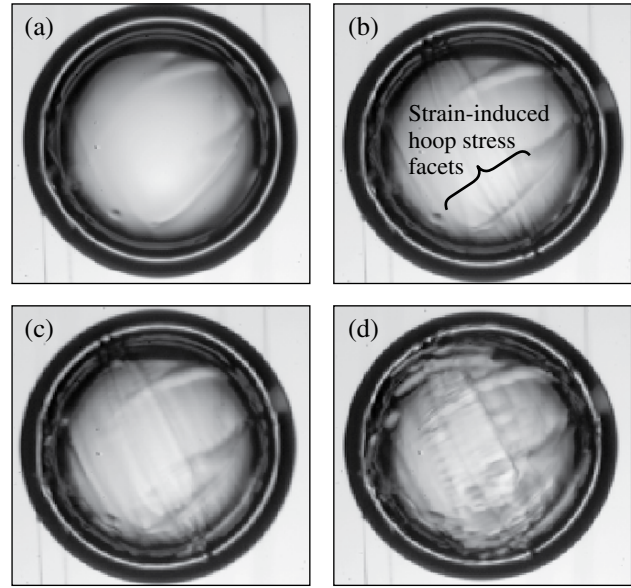


Figure 114.19 Images of the ice layer when it is rapidly cooled showing preferred orientation of cracks: (a) initial rms roughness is 2.2 μm ; (b) +145 s and -1.4 K, 2.2 μm ; (c) +180 s and -2 K, 2.3 μm ; (d) +300 s and -2.6 K, 2.6 μm .

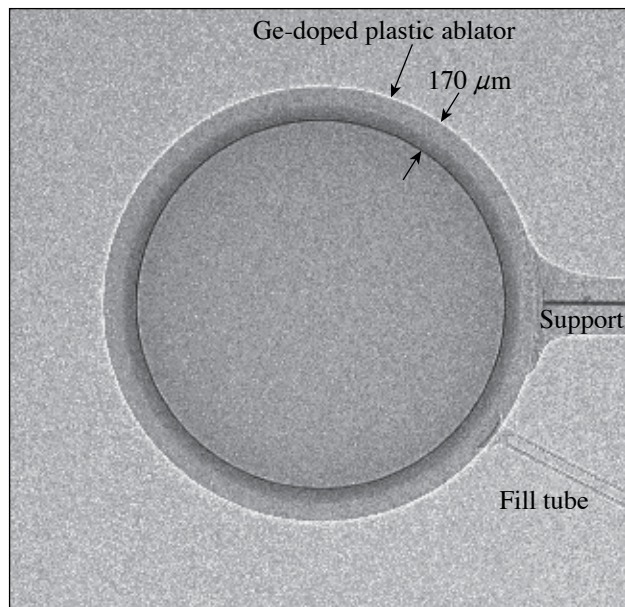
2. Cryogenic Fill-Tube Test Facility

Two new cryogenic systems designed specifically to study targets that are filled via a tube are now operational. This capability is needed to study cryogenic-target science issues that cannot be addressed with the existing OMEGA Cryogenic Target Handling System (CTHS). Two goals for the system will be (1) to prototype the environs surrounding a NIF-scale target and demonstrate that the design of the layering sphere is suitable for producing NIF-scale targets that meet the ice-thickness and ice-roughness specifications, and (2) to support specific studies of cryogenic targets that cannot be performed using the OMEGA CTHS.

The new equipment has capabilities and features not available on the CTHS, including (1) the ability to characterize a D₂-ice layer using both x-ray phase contrast (see Fig. 114.20) and shadowgraphy to cross-calibrate these techniques; (2) a cryogenic rotation stage small enough to be included in the NIF CTHS to preserve the ability to rotate a target through the

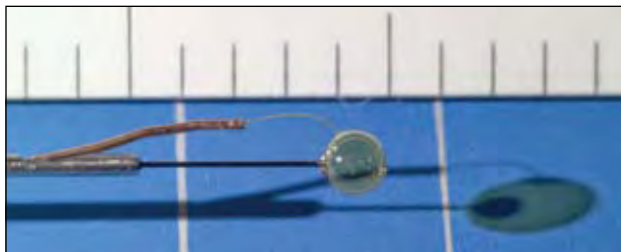
field of view of the diagnostics to compile a 3-D analysis of the entire surface of the target; and (3) a layering sphere environment that incorporates the target support structure and fill-tube accessories that will be used to field cryogenic targets on the National Ignition Facility (Fig. 114.21) (Ref. 24).

Targets to be tested in this equipment include fast-ignition, cone-in-shell OMEGA-scale targets; indirect-drive NIF-scale targets mounted in a transparent hohlraum; and foam NIF-scale targets in standard support structures and “Saturn-ring” support structures.²⁴



T2442JR

Figure 114.20
X-ray phase-contrast image of a 2.2-mm-diam NIF indirect-drive-scale capsule with a germanium-doped plastic ablator. The support for the target is horizontal and below it is the tube for filling the target.



T2444JRC

Figure 114.21
NIF-scale, 3.0-mm-diam direct-drive target showing the horizontal support and fill tube.

The planned experiments include qualifying a thermal environment and protocol for forming targets that meet NIF specification, evaluating the dynamics of the targets’ support to ensure accurate pointing and target stability, and optimizing the trade-off between these competing requirements.

Conclusion

The ability to form cryogenic targets with radioactive DT ice that meet the exacting specifications, and to deliver those targets for implosion experiments, demonstrates a substantial advancement in the capabilities of the OMEGA system. Current emphasis is on supplying these targets for experiments and on improving the operation, while simultaneously improving the consistency of D₂ cryogenic target quality.

Beyond the scope of supporting ongoing experiments, we are supporting the National Ignition Campaign by studying issues relevant to indirect-drive cryogenic targets. We are also extending our capability to studying the requirements for making larger-sized targets intended to achieve ignition on the NIF using direct illumination.

ACKNOWLEDGMENT

This work was supported by the U.S. Department of Energy Office of Inertial Confinement Fusion under Cooperative Agreement No. DE-FC52-08NA28302, the University of Rochester, and the New York State Energy Research and Development Authority. The support of DOE does not constitute an endorsement by DOE of the views expressed in this article.

REFERENCES

1. J. K. Hoffer and L. R. Foreman, *Phys. Rev. Lett.* **60**, 1310 (1988).
2. J. Sater *et al.*, *Fusion Technol.* **35**, 229 (1999); J. D. Sheliak and J. K. Hoffer, *Fusion Technol.* **35**, 234 (1999).
3. T. C. Sangster, J. A. Delettrez, R. Epstein, V. Yu. Glebov, V. N. Goncharov, D. R. Harding, J. P. Knauer, R. L. Keck, J. D. Kilkenny, S. J. Loucks, L. D. Lund, R. L. McCrory, P. W. McKenty, F. J. Marshall, D. D. Meyerhofer, S. F. B. Morse, S. P. Regan, P. B. Radha, S. Roberts, W. Seka, S. Skupsky, V. A. Smalyuk, C. Sorce, J. M. Soures, C. Stoeckl, K. Thorp, J. A. Frenje, C. K. Li, R. D. Petrasso, F. H. Séguin, K. A. Fletcher, S. Padalino, C. Freeman, N. Izumi, J. A. Koch, R. A. Lerche, M. J. Moran, T. W. Phillips, and G. J. Schmid, *Phys. Plasmas* **10**, 1937 (2003).
4. G. W. Collins *et al.*, *J. Vac. Sci. Technol. A* **14**, 2897 (1996).
5. D. R. Harding, T. C. Sangster, D. D. Meyerhofer, P. W. McKenty, L. D. Lund, L. Elasky, M. D. Wittman, W. Seka, S. J. Loucks, R. Janezic, T. H. Hinterman, D. H. Edgell, D. Jacobs-Perkins, and R. Q. Gram, *Fusion Sci. Technol.* **48**, 1299 (2005).
6. *LLE Review Quarterly Report* **109**, 46, Laboratory for Laser Energetics, University of Rochester, Rochester, NY, LLE Document No. DOE/SF/19460-739 (2006).

7. T. J. B. Collins, A. Poludnenko, A. Cunningham, and A. Frank, *Phys. Plasmas* **12**, 062705 (2005); *LLE Review Quarterly Report* **100**, 227, Laboratory for Laser Energetics, University of Rochester, Rochester, NY, LLE Document No. DOE/SF/19460-578, NTIS Order No. PB2006-106672 (2004). (Copies may be obtained from the National Technical Information Service, Springfield, VA 22161.)
8. S. H. Leiden and F. A. Nichols, *J. Nucl. Mater.* **38**, 309 (1971).
9. M. J. Hiza, *Fluid Phase Equilib.* **6**, 203 (1981).
10. S. Raynor and D. R. Herschbach, *J. Phys. Chem.* **87**, 289 (1983); R. H. Scheicher *et al.*, *Bull. Am. Phys. Soc.* **48**, 434 (2003), Paper H12.005.
11. N. Kawamura *et al.*, *Phys. Lett. B* **465**, 74 (1999).
12. P. C. Souers, *Hydrogen Properties for Fusion Energy* (University of California Press, Berkeley, 1986).
13. A. Crane and H. P. Gush, *Can. J. Phys.* **44**, 373 (1966).
14. M. Alexander, *2002 Summer Research Program for High School Juniors at the University of Rochester's Laboratory for Laser Energetics*, University of Rochester, Rochester, NY, LLE Report No. 329, LLE Document No. DOE/SF/19460-479 (2003).
15. Aculight Corporation, Bothell, WA 98021.
16. Labsphere, Inc., North Sutton, NH 03260.
17. *FRED*, Photon Engineering, LLC, Tucson, AZ 85711.
18. ANSYS, Inc., Lebanon, NH 03766.
19. R. C. Cook *et al.*, *Fusion Sci. Technol.* **45**, 148 (2004).
20. A. Nikroo, General Atomics, private communication (2008).
21. D. R. Harding, D. D. Meyerhofer, S. J. Loucks, L. D. Lund, R. Janezic, L. M. Elasky, T. H. Hinterman, D. H. Edgell, W. Seka, M. D. Wittman, R. Q. Gram, D. Jacobs-Perkins, R. Early, T. Duffy, and M. J. Bonino, *Phys. Plasmas* **13**, 056316 (2006).
22. E. Mapoles, Lawrence Livermore National Laboratory, private communication (2008).
23. M. Martin *et al.*, *Fusion Sci. Technol.* **49**, 600 (2006).
24. R. S. Craxton and D. W. Jacobs-Perkins, *Phys. Rev. Lett.* **94**, 095002 (2005).

Multiple-FM Smoothing by Spectral Dispersion—An Augmented Laser Speckle Smoothing Scheme

Introduction

Polar-drive (PD)^{1–4} implosions on the National Ignition Facility (NIF) require smoothing of the laser-imposed nonuniformities. The spot shape on target is controlled by employing distributed phase plates (DPP's).^{5,6} Smoothing by spectral dispersion (SSD)^{7–9} smoothes the far-field speckle pattern in a time-integrated sense by continuously changing the near-field phase front of the laser beam. The current configuration of the NIF has SSD in only one dimension (i.e., 1-D SSD), which is insufficient for directly driven targets. A two-dimensional (2-D) SSD system with a 1-THz ultraviolet bandwidth and two color cycles proposed for the NIF provides the requisite smoothing but it is an expensive option that adds considerable complexity.¹⁰ An idea originally suggested by Rothenberg¹¹ further improved beam smoothing of all spatial frequencies by augmenting the 2-D SSD system with multiple-FM modulators in both dimensions at the expense of both increased complexity and cost. An alternative laser speckle smoothing scheme proposed here employs multiple-FM modulators in a single dimension (MultiFM 1-D SSD) with minimal cost increase and added system complexity since the added modulation can be applied in the all-fiber-optic front-end system. In addition, this system concentrates beam-smoothing improvements on the lower end of the spatial frequencies that most limit direct-drive implosions with a low in-flight aspect ratio.

MultiFM 1-D SSD employs multiple color cycles to improve the smoothing of lower-spatial-frequency nonuniformities without producing resonances at higher spatial frequencies because multiple modulators interact and effectively average the resonant features with a judicious choice of modulator frequencies. MultiFM 1-D SSD attains similar or even faster smoothing rates compared to the full 2-D SSD system, albeit with shorter asymptotic times. Two-dimensional hydrodynamic simulations using *DRACO*¹² show that MultiFM 1-D SSD is sufficient for the targets and pulse shapes analyzed thus far, even for smaller overall bandwidth (in the 0.5-THz range), which means that a single frequency-conversion crystal system can be used for the NIF with significant cost and complexity savings.

MultiFM Coherence Time

When SSD is employed, smoothing for any spatial frequency can be characterized by an inverse coherence time (or smoothing rate) and an asymptotic nonuniformity. The rms average of the inverse coherence times over all spatial frequencies is equivalent to the effective bandwidth applied to the laser beam; however, this bandwidth is not uniformly distributed over the spatial frequencies imposed in the far-field plane, which range from zero to the highest spatial frequency determined by the diffraction limited spot. The SSD system does not continue to smooth forever but is limited to the characteristic asymptotic level that is determined by the angular divergence of the near field imposed by SSD. Both of these characteristics can be represented by a fitted functional form

$$\sigma^2(t, \ell) = \sigma_0^2(\ell) \frac{t_c(\ell)}{t + t_c(\ell)} + \sigma_{\text{asym}}^2(\ell), \quad (1)$$

where $\sigma_0^2(\ell) \equiv \sigma^2(0, \ell)$ is the initial value of the nonuniformity and $\sigma_{\text{asym}}^2(\ell) \equiv \sigma^2(\infty, \ell)$ is the asymptotic level of the nonuniformity for the spatial mode given by ℓ .

After a few coherence times and prior to reaching the asymptotic level, Eq. (1) can be approximated by

$$\sigma^2(t, \ell) \approx \sigma_0^2(\ell) \frac{t_c(\ell)}{t}, \quad t_c < t < t_{\text{asym}}. \quad (2)$$

During this time, the coherence time proportionally affects the level of nonuniformity, whereas the “slope” is given by t^{-1} . If the coherence time can be decreased by modifying the SSD design, the nonuniformity for a given mode will decrease proportionally. The asymptotic nonuniformity level σ_{asym} is determined by the angular divergence of the SSD system because this determines the number of independent modes in the far field. Increasing the angular divergence reduces σ_{asym} .

The smoothing performance of any SSD system, including MultiFM, is accurately calculated using a specialized, time-dependent far-field simulation, like *Waasikwa'*.¹³ Figure 114.22 shows the smoothing performance of the ℓ -mode range $30 < \ell < 60$ for the NIF 1-D SSD system with 10.8 Å of applied IR bandwidth yielding 878 GHz of ultraviolet bandwidth.^(a) The figure also indicates the relative improvements that could be made for this ℓ -mode range by increasing the applied bandwidth $\Delta\lambda$ or the angular divergence $\Delta\theta_{SSD}$. For ℓ modes lower than the first local maximum in the distributed inverse coherence time (roughly $\ell < 100$ for systems in this article; see Fig. 114.25), the inverse coherence time is approximately given by $t_c^{-1} \propto \ell \Delta\lambda N_{cc}$, where N_{cc} is the effective number of color cycles. The angular divergence of one dimension is given approximately by $\Delta\theta_{SSD} \propto \Delta\lambda N_{cc} / \nu_m$, where ν_m is the modulator frequency.

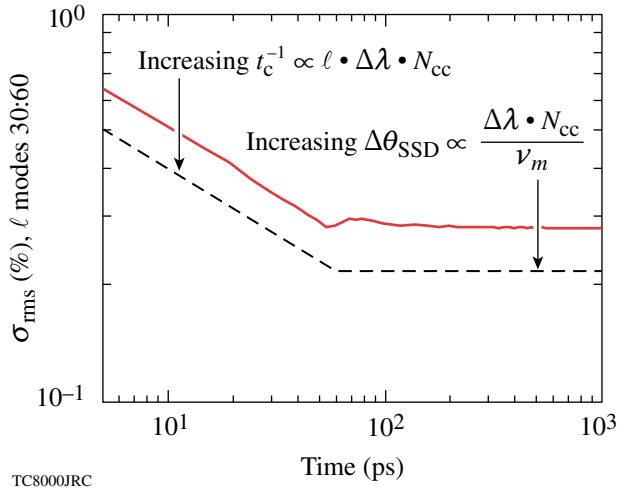


Figure 114.22 Time evolution of the nonuniformity summed over the ℓ -mode range $30 < \ell < 60$ for the NIF 1-D SSD system with 10.8 Å of applied bandwidth (878-GHz UV). The solid line represents the result of a *Waasikwa'* far-field simulation. The dashed line indicates the improvements possible by altering the coherence time and/or the angular divergence: (1) decreasing the coherence time of a mode proportionally decreases the level of nonuniformity during $t_c < t < t_{asym}$ and (2) increasing the angular divergence will decrease the asymptotic level σ_{asym} .

Figure 114.23 shows the smoothing effect on the lower ℓ modes by increasing the number of color cycles while holding the bandwidth and angular divergence constant. For early times in the laser pulse (not shown), the initial nonuniformity is the same [$\sigma^2(t, \ell) \rightarrow \sigma_0^2(\ell)$ as $t \rightarrow 0$] for each case. However,

increasing the number of color cycles delivers asymptotic smoothing performance at earlier times. This illustrates that as the inverse coherence time is increased for this ℓ -mode range, the far field can be smoothed faster and the asymptotic level can be reached earlier.

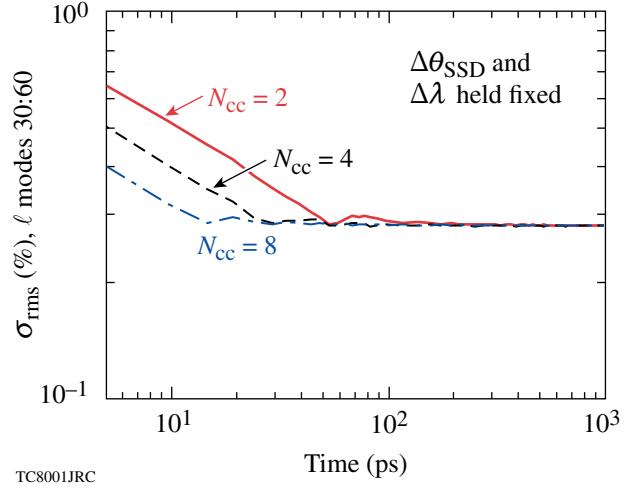


Figure 114.23 Time evolution of the nonuniformity rss-summed over the ℓ -mode range $30 < \ell < 60$ for three different realizations of a 1-D SSD system. The applied bandwidth and angular divergence are held fixed at 10.8 Å and 100 μ rad, respectively, while the number of color cycles is varied as 2, 4, and 8, which correspond to modulator frequencies of 17.5, 35.5, and 70.5 GHz, respectively. All three traces represent full *Waasikwa'* far-field simulations. The effective bandwidth is 1.1 THz.

As previously noted, the inverse coherence time is not constant over the entire ℓ -mode range of the far-field intensity pattern. The inverse coherence time for each ℓ mode and the values of $\sigma_0^2(\ell)$ and $\sigma_{asym}^2(\ell)$ can be calculated by fitting Eq. (1) to time-dependent *Waasikwa'* far-field simulations, but this is a computationally intensive process. A simplified phenomenological formulation is desirable for evaluating or designing many SSD system variations. However, it is essential that the simple mathematical model given here is verified against a full far-field simulation prior to performing the even-lengthier hydrodynamic simulation. This is done by verifying a final MultiFM system design using the simple t_c^{-1} model against a time-dependent *Waasikwa'* simulation fitted to Eq. (1).

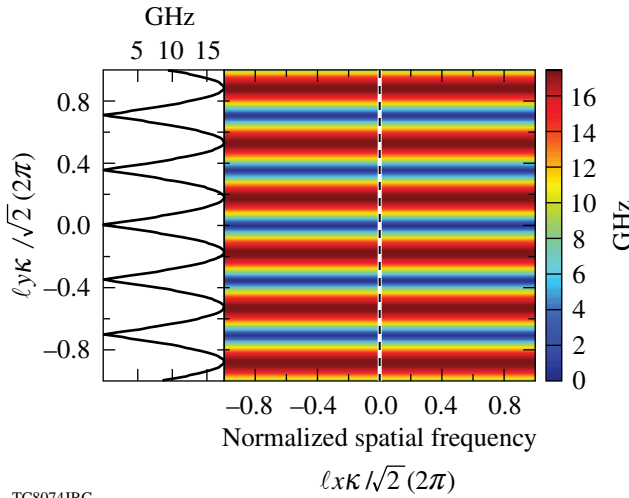
For a 1-D SSD system the inverse coherence time along a single spatial dimension¹¹ is given by

^(a)Conventionally, the applied laser bandwidth is specified in two different units to distinguish to which end of the frequency-converted laser system the bandwidth refers. When the bandwidth is given in angstroms (Å), it refers to the bandwidth in the front-end IR system and when the bandwidth is specified in GHz or THz, it refers to the bandwidth following the frequency-conversion crystals in the UV range. An IR bandwidth of 12.3 Å corresponds to 1.0 THz in the UV.

$$t_c^{-1}(\ell_x) = 2\Delta\lambda \sin\left(\frac{1}{2}\ell_x \kappa N_{cc,x}\right) \quad (3)$$

along one of the two spatial-frequency directions, where $\ell_x \equiv k_{x_{\text{ff}}} r_{\text{tar}}$, $\kappa \equiv f_{\text{NIF}} \lambda_{\text{UV}} / (r_{\text{tar}} D_{\text{NIF}})$, and $k_{x_{\text{ff}}}$, f_{NIF} , λ_{UV} , r_{tar} , and D_{NIF} are the NIF spatial frequency, focal length, laser wavelength, target radius and near-field diameter, respectively. A similar functional form represents the second dimension for a 2-D SSD system; if no second dimension is included, then $t_c^{-1}_y = 0$. For a single-modulator 1-D SSD system, a 2-D plot of the inverse coherence time is shown in Fig. 114.24 for the two-color-cycle, 10.8 Å, 1-D SSD system described in Fig. 114.23. Note that in Fig. 114.24 the inverse coherence time periodically goes to zero for spatial frequencies where no beam smoothing is achieved. Equation (3) defines the inverse coherence time in only a single spatial-frequency dimension, but an azimuthal average is standard practice for comparing the effectiveness of different SSD systems (including MultiFM and 2-D SSD). The inverse coherence time for an effective ℓ mode in the 2-D plane is defined as

$$t_c^{-1}_{\text{rss}}(\ell) \equiv \sqrt{(t_c^{-1}_x)^2 + (t_c^{-1}_y)^2}, \quad (4)$$



TC8074JRC

Figure 114.24

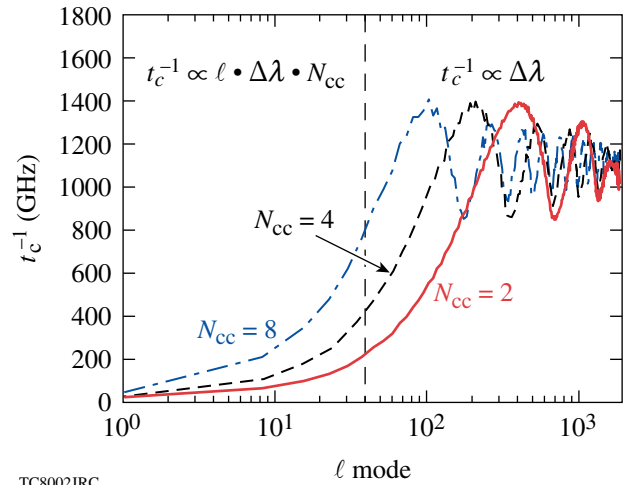
The inverse coherence time t_c^{-1} (in GHz) plotted in two dimensions as a function of the normalized-spatial-frequency, two-color-cycle system in Fig. 114.23 (1.1 THz, 100 μrad). Note that the number of zeros counted along the positive or negative axis for non-zero frequencies up to the effective round-aperture cut-off frequency yields the number of color cycles. In this case, there are two zeros along the positive or negative vertical axis. The axis has been normalized to a square NIF aperture and therefore is lengthened by $\sqrt{2}$ relative to a round aperture. A lineout in the SSD dispersion direction illustrates how the inverse coherence time periodically goes to zero. No beam smoothing is experienced at these spatial frequencies.

where $\ell \equiv \ell(\theta) = \sqrt{\ell_x^2 + \ell_y^2}$ is the radial ℓ mode. In addition, it is necessary to account for the effect of the near-field beam envelope on the resultant inverse coherence time because the envelope affects the relevant weighting of the contribution of each spatial frequency in the 2-D spatial-frequency plane. The mathematical model of a 1-D or 2-D SSD system is then given by

$$t_c^{-1}(\ell) = \frac{\oint t_c^{-1}_{\text{rss}}(\ell) \text{PSD}_0(\ell) \ell d\theta}{\oint \text{PSD}_0(\ell) \ell d\theta}, \quad (5)$$

where $\text{PSD}_0(\ell)$ is the spatial-frequency power spectrum of the diffraction-limited spot or single speckle pattern.^{16,17} Note that the $\text{PSD}_0(\ell)$ can be used to analyze the effect of partially filled near-field apertures.

Equation (5) is employed to calculate the inverse coherence time versus ℓ mode for the three realizations of the 1-D SSD system, as shown in Fig. 114.25. These curves illustrate distinct behavior for the large ℓ -mode and low ℓ -mode regions. The mean value of the inverse coherence time yields a measure of the effective bandwidth. For the 1-D SSD systems the



TC8002JRC

Figure 114.25

The inverse coherence time t_c^{-1} (in GHz) plotted as a function of the spatial ℓ -mode number for the three different 1-D SSD systems described in Fig. 114.23. The number of color cycles is varied as 2, 4, and 8. The divergences are fixed at 100 μrad . Note that the average inverse coherence time for the large ℓ modes is approximately 1.25 \times the applied bandwidth of 878 GHz and that the inverse coherence time for the lower ℓ modes ($\ell <$ first local maximum) is given by $t_c^{-1} \propto \ell \Delta\lambda N_{cc}$. The resultant effective bandwidth is 1.1 THz. The vertical dashed line indicates the approximate distinction between low ℓ and high ℓ modes.

effective bandwidth is 1.1 THz, which is roughly $1.25\times$ the applied bandwidth for a single modulator system. In the large ℓ -mode range, the inverse coherence time is given roughly by the effective bandwidth. The peak of the first local maximum is $1.1\sqrt{2}$ of the applied bandwidth, as related to the maximum of Eq. (3) that is azimuthally averaged around the 2-D plane. In the ℓ -mode range lower than the first local maximum, the inverse coherence time is given by

$$t_c^{-1}(\ell) = \Delta\lambda\ell\kappa N_{cc}, \quad (6)$$

which can be understood by taking the small angle approximation to Eq. (3).

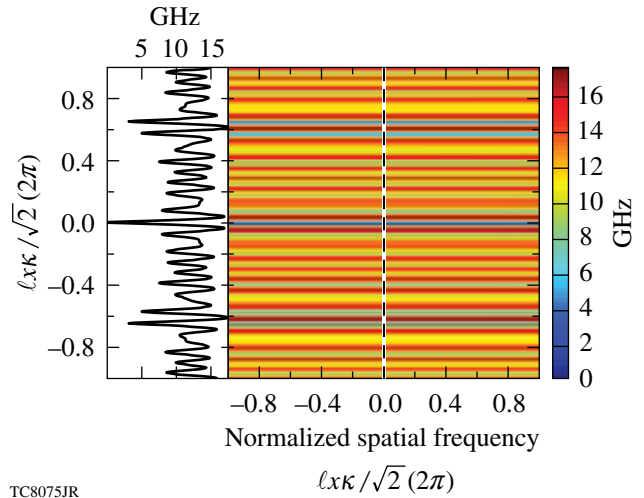
Another feature in Fig. 114.25 is the series of strong resonances in the large ℓ -mode range. This is due to the coherent effect of having multiple color cycles across the near-field plane. Each color cycle is a copy of its neighbors and does not lend to smoothing at the corresponding spatial frequency, which leads to the zeroes of Eq. (3). The zeroes of the resonant features are a 1-D effect, and their relative effect is lessened due to the azimuthal averaging of Eq. (5); however, the zeroes are still present in the 2-D plane and represent spatial frequencies that experience no smoothing and are a potential threat in an ICF implosion due to hydrodynamic instabilities. The only smoothing that these modes get is from multiple beam overlap on target.

The resonant features caused by multiple color cycles can be mitigated with MultiFM if the modulator frequencies are judiciously chosen. The effect of multiple overlaid patterns dramatically reduces the range of spatial frequencies that do not benefit from beam smoothing, as illustrated in Fig. 114.26. In the near field, the application of MultiFM in 1-D takes the form

$$E(x, y) = E_0(x, y) \prod_{n=1}^N e^{i3\delta_n \sin[\omega_n(t + \xi_x x)]}, \quad (7)$$

where $E_0(x, y)$ is the near-field beam envelope and δ_n , ω_n , and ξ_x are modulation depth, frequency, and grating dispersion for the n th modulators, respectively.

To calculate the inverse coherence time for the MultiFM case, Eq. (3) can be generalized by root-sum-square (rss) summing the values for each modulator. This approximation is valid when the modulation frequencies are incommensurate and the mixing of the modes in the far field temporally integrates to zero since terms like $\cos(\omega_m t) \cdot \cos(\omega_n t)$ average to zero



TC8075JR

Figure 114.26

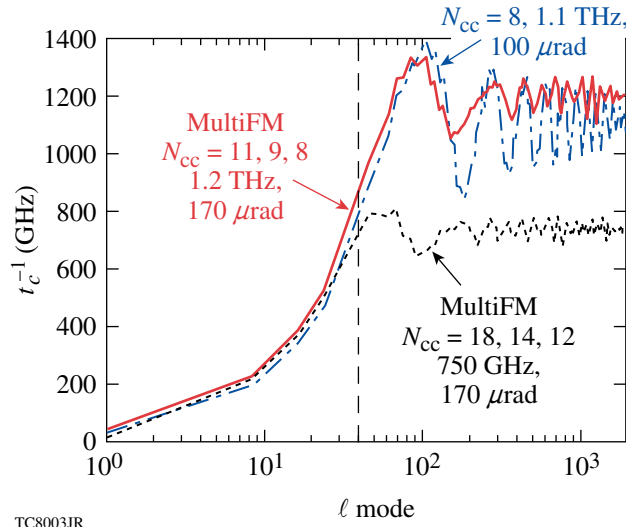
The inverse coherence time t_c^{-1} (in GHz) plotted in two dimensions as a function of normalized spatial frequency for a MultiFM 1-D SSD system employing three modulators at frequencies of 65, 75, and 95 GHz ($N_{cc} = 8, 9, \text{ and } 11$, respectively) with a combined divergence of $175 \mu\text{rad}$ and effective ultraviolet bandwidth of 1.2 THz. A lineout in the 1-D SSD dispersion direction illustrates the significant improvement in beam smoothing compared to Fig. 114.24. Note that the inverse coherence time goes to zero for all modulators at the origin by definition.

when m is not equal to n . A three-modulator MultiFM case is compared in Fig. 114.27 to a single-modulator, eight-color-cycle case. Three modulators at frequencies of 65, 75, and 95 GHz ($N_{cc} = 8, 9, \text{ and } 11$, respectively) produce a combined divergence of $175 \mu\text{rad}$ and effective ultraviolet bandwidth of 1.2 THz. Beam-smoothing rates are comparable for low ℓ modes, but the MultiFM configuration outperforms the single modulator for high ℓ modes due to the overlapped effect of multiple modulators, each with multiple color cycles. The effective color-cycle number is weighted by the bandwidth of each modulator,

$$N_{cc_{mFM}} \simeq \frac{\sqrt{\sum_{n=1}^N (N_{cc_n} \Delta\lambda_n)^2}}{\sqrt{\sum_{n=1}^N \Delta\lambda_n^2}}, \quad (8)$$

while the effective bandwidth and angular divergence can be estimated by rss-summing the contributions from each modulator. The total angular divergence, however, can have significant energy in the wings of the distribution as far out as the linear sum of the individual divergences.

An important observation is that improved lower ℓ -mode performance can also be achieved while decreasing the total

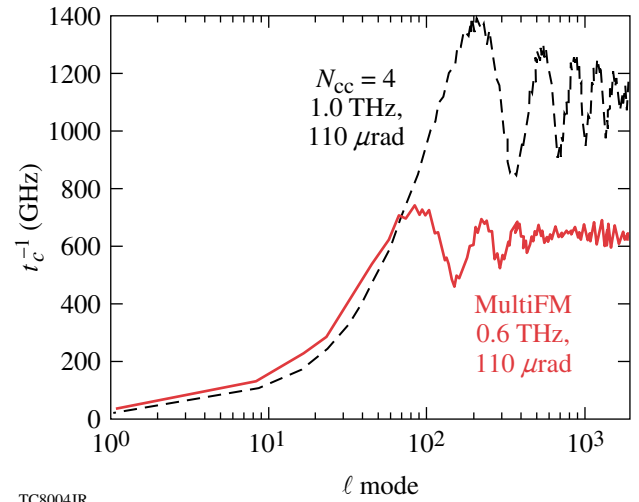


TC8003JR

Figure 114.27

Azimuthally averaged inverse coherence time plotted as a function of spatial ℓ -mode number for an eight-color-cycle, 1-D SSD system (eight color cycles, 1.1 THz, $100 \mu\text{rad}$) and MultiFM 1-D SSD system (8, 9, and 11 color cycles, 1.2 THz, $170 \mu\text{rad}$). Another MultiFM 1-D SSD realization is also shown (12, 14, and 18 color cycles, 750 GHz, $170 \mu\text{rad}$) using three modulators at 68, 77, and 94 GHz, respectively, but a smaller effective bandwidth of 750 GHz. The vertical dashed line indicates the approximate distinction between low ℓ and high ℓ modes.

applied bandwidth, as long as the product $\Delta\lambda \cdot N_{cc}$ and the angular divergence $\Delta\theta$ are held constant. In general, high ℓ -mode nonuniformities decouple much sooner from directly driven targets with low in-flight aspect ratios than lower ℓ modes, which implies that the larger ℓ modes do not utilize all the potential smoothing of these modes. MultiFM 1-D SSD makes it possible to reduce the total bandwidth applied while maintaining the same performance of the lower ℓ modes. This phenomenon is depicted in the third plot (dashed) in Fig. 114.27, where a different set of modulation frequencies and color cycles achieves the same performance with a lower effective bandwidth of 750 GHz. Likewise, the two-modulator MultiFM 1-D SSD system shown in Fig. 114.28 matches the low ℓ -mode performance with only 600-GHz effective bandwidth and $110 \mu\text{rad}$ of divergence. Two-dimensional hydrodynamic DRACO simulations of NIF direct-drive targets with $1\text{-}\mu\text{m}$ (rms) inner ice roughness, 30-ps (rms) mistiming, $50\text{-}\mu\text{m}$ (rms) beam mispointing, and 8% (rms) energy imbalance for a 1.5-MJ CH-foam target in a symmetric-drive configuration show that this MultiFM system provides sufficient beam smoothing to achieve ignition. Further research is underway to determine if the bandwidth and the total energy delivered to target can be reduced, as well as to investigate MultiFM 1-D SSD for polar-drive implosions. Significant costs and complexity could be avoided on the NIF



TC8004JR

Figure 114.28

The inverse coherence time plotted as a function of spatial ℓ -mode number for a four-color-cycle, 1-D SSD system and a low ℓ -mode-matching MultiFM 1-D SSD system with two modulators and lower applied bandwidth. This realization of a MultiFM 1-D SSD system employs two modulators at frequencies of 55 and 60 GHz ($N_{cc} = 9$ and 10, respectively) and used a combined divergence of $110 \mu\text{rad}$ and only 600 GHz of effective UV bandwidth.

if the applied bandwidth can be reduced to 0.5 THz, since only a single frequency-tripling crystal would be required.

MultiFM Divergence

The asymptotic level of nonuniformity, σ_{asym} , of the lower ℓ modes is governed by the angular divergence because more-independent speckle modes are created. The angular divergence is ultimately limited by the smallest pinhole in the laser system. The primary concern is pinhole closure during the main drive pulse. Currently, the angular divergence $\Delta\theta_{\text{SSD}}$ for the NIF is limited to $100 \mu\text{rad}$ (full angle), which is set by a minimum pinhole size of $300 \mu\text{rad}$. Dynamic bandwidth reduction¹⁴ should allow the angular divergence to be increased without the risk of pinhole closure since simulations indicate that strong beam smoothing is required only during the initial low-power portion of the laser pulse when significant laser imprinting occurs.¹⁵ The angular divergence of SSD for a single modulator is given by

$$\Delta\theta_{\text{SSD}} \propto \frac{N_{cc}\Delta\lambda}{\nu_m}, \quad (9)$$

where ν_m is the modulator frequency. The angular divergence can be increased by increasing the $N_{cc}\Delta\lambda$ product and/or decreasing the modulator frequency ν_m . Current investigations of MultiFM have limited divergence to a maximum full angle of $170 \mu\text{rad}$, but increasing this limit could further improve

smoothing of these important modes. Detailed laser imprint experiments will be performed on OMEGA EP with a prototypical NIF beam-smoothing system to establish practical dynamic bandwidth reduction schemes. Additional experiments will also be performed to establish any lower limit of beam smoothing required late in the drive pulse to mitigate adverse laser-plasma interactions.

The asymptotic nonuniformity level and the time it takes to reach this level can be accurately calculated for a square pulse shape due to MultiFM 1-D SSD.¹⁸ The nonuniformity as a function of time can also be calculated for arbitrary pulse shapes and 2-D SSD system configuration but is beyond the scope of this article and will be discussed in a forthcoming article. The asymptotic nonuniformity due to a MultiFM 1-D SSD system is given by

$$\sigma_{\text{asym}}(\ell) = \frac{1}{2\pi} \oint \prod_{n=1}^N J_0[\zeta_n(\ell, \theta)] d\theta, \quad (10a)$$

where

$$\zeta_n(\ell, \theta) \equiv 6\xi_n \sin\left[\pi N_{\text{cc}_n} \frac{\ell}{\ell_c} \cos(\theta)\right], \quad (10b)$$

J_0 is a zeroth-order Bessel function of the first kind, and $\ell_c \equiv 2\pi r_{\text{tar}} D_{\text{NIF}} / (f_{\text{NIF}} \lambda_{\text{UV}})$ is the ℓ -mode cutoff. The angle θ is necessary because although the proposed MultiFM beam smoothing is applied only in a single direction, the spectrum is inherently 2-D and it facilitates the azimuthal average. The number of independent states is found by $N_{\text{states}} = 1 / \sigma_{\text{asym}}^2(\ell)$. If the coherence time is known for the ℓ mode, then the asymptotic time is given by $t_{\text{asym}} = t_c N_{\text{states}}$. The formulation represented in Eqs. (10) is appropriate for all ℓ modes.

The statement that increasing the angular divergence, given by Eq. (9), decreases the σ_{asym} , given by Eqs. (10), can be understood by examining the arguments of the Bessel function. This applies only to the lower ℓ modes due to the sine function as an argument to the Bessel function and to the multi-color-cycle effects. As the argument of the Bessel function increases, the peak envelope of the Bessel function decreases. For ℓ modes lower than the peak of the first maximum of the sine function, the argument of the Bessel function increases when the product $\delta_m N_{\text{cc}}$ increases. The product relates to the total angular divergence because $\delta_m N_{\text{cc}} \propto \Delta \lambda N_{\text{cc}} / (2\nu_m) \propto \Delta \theta$.

Beam-smoothing performance depends not only on the inverse coherence time and the total divergence but also on the shape of the spectral divergence. Some combinations of modulators yield excellent smoothing rates (inverse coherence time) for a given total divergence, but do not provide adequate beam smoothing due to the spectral distribution. The effectiveness of spectral modes is weighted by their amplitudes. The shape of the spectrum is found by taking the 2-D Fourier transform of the near-field beam with its associated SSD phase front applied but without a phase plate. In general, the shape of the far-field spectrum differs from the shape of the temporal frequency spectrum due to the near-field beam shape. Ideally, modes are evenly weighted for best smoothing performance, but edge-peaked spectra perform better than center-peaked spectra. An example is shown in Fig. 114.29, where the applied bandwidth and total divergences are identical for the two different MultiFM cases. The configuration with a more-uniform divergence but some edge peaking [Fig. 114.29(a)] gives better far-field simulation performance early in time than the strong, center-peaked divergence shown in Fig. 114.29(b), which is illustrated in Fig. 114.29(c).

Conclusion

Implementing MultiFM 1-D SSD beam smoothing on the NIF is a promising approach to meet the smoothing requirements for polar-drive implosions. It provides the flexibility to tailor the inverse coherence time spectrum to meet the target hydrodynamic-instability requirements while potentially reducing the overall bandwidth of the SSD system. Multiple color cycles are used to increase the performance of the lower ℓ modes and multiple modulators are used to reduce the resonant effects of multiple color cycles. Figure 114.30 shows how the MultiFM 1-D SSD system with 600-GHz effective bandwidth and 110 μrad of divergence described in Fig. 114.28 nearly attains the same target performance for a 1.5-MJ CH-foam target as the baseline 1-THz, 2-D SSD. Future work will extend these results to a 500-GHz MultiFM 1-D SSD system and a 1.0-MJ CH-foam target. It may require increasing the angular divergence and invoking dynamic bandwidth reduction.

ACKNOWLEDGMENT

This work was supported by the U.S. Department of Energy Office of Inertial Confinement Fusion under Cooperative Agreement No. DE-FC52-08NA28302, the University of Rochester, and the New York State Energy Research and Development Authority. The support of DOE does not constitute an endorsement by DOE of the views expressed in this article.

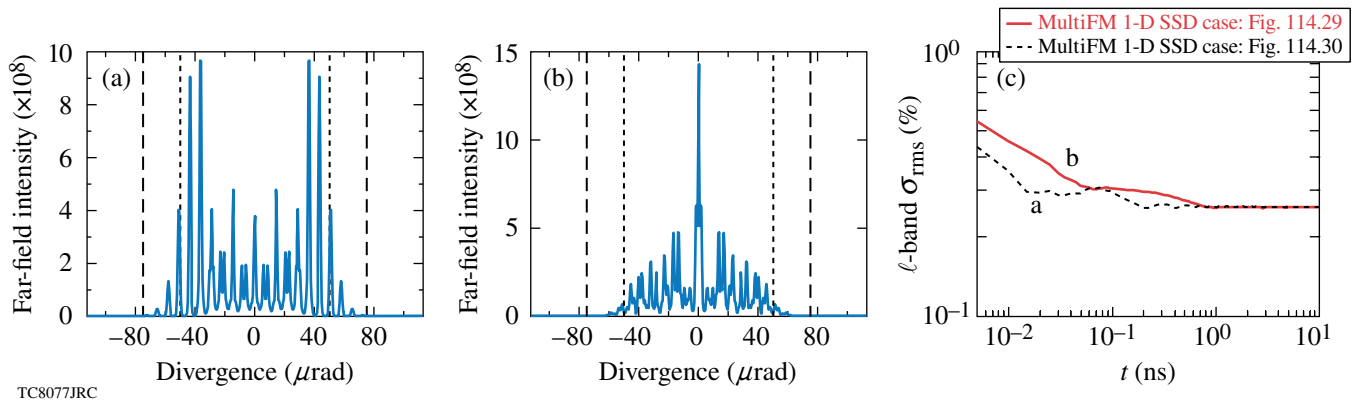


Figure 114.29

Angular divergence, plotted in the far field or pinhole plane, for two different MultiFM 1-D SSD systems with 820-GHz effective bandwidth and 110 μrad of divergence. The modulator frequencies were (a) 61 and 55 GHz with eight and seven color cycles, respectively, and (b) 61 and 45 GHz with eight and five color cycles, respectively. The thin dashed vertical line represents the 100- μrad specification and the thick dashed line represents the 150- μrad boundary. Note how the spectrum in (b) is more widely distributed and edge peaked relative to (a). (c) The nonuniformity calculated by *Waaasikwa'* is rss-summed over ℓ modes 30 to 60 and is plotted as a function of time. Both systems have the same resulting asymptotic value but the system with the edge-peaked spectrum has improved performance early in time.

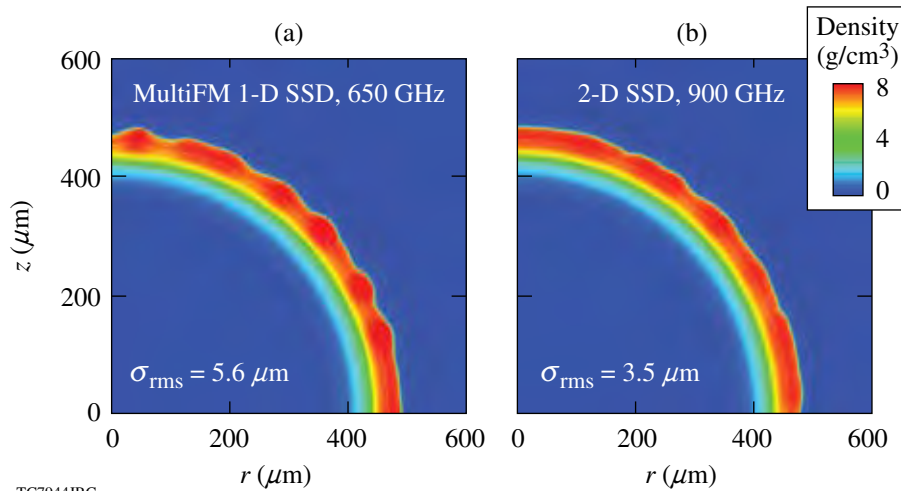


Figure 114.30

1.5-MJ CH-foam target at the end of the acceleration phase for three different SSD systems. (a) MultiFM 1-D SSD described in Fig. 114.28 and (b) 2-D SSD. Both the MultiFM 1-D SSD system and the 2-D SSD system attain nearly 1-D gain.

REFERENCES

1. S. Skupsky, J. A. Marozas, R. S. Craxton, R. Betti, T. J. B. Collins, J. A. Delettrez, V. N. Goncharov, P. W. McKenty, P. B. Radha, T. R. Boehly, J. P. Knauer, F. J. Marshall, D. R. Harding, J. D. Kilkenny, D. D. Meyerhofer, T. C. Sangster, and R. L. McCrory, *Phys. Plasmas* **11**, 2763 (2004).
2. J. A. Marozas, F. J. Marshall, R. S. Craxton, I. V. Igumenshchev, S. Skupsky, M. J. Bonino, T. J. B. Collins, R. Epstein, V. Yu. Glebov, D. Jacobs-Perkins, J. P. Knauer, R. L. McCrory, P. W. McKenty, D. D. Meyerhofer, S. G. Noyes, P. B. Radha, T. C. Sangster, W. Seka, and V. A. Smalyuk, *Phys. Plasmas* **13**, 056311 (2006).
3. R. S. Craxton and D. W. Jacobs-Perkins, *Phys. Rev. Lett.* **94**, 095002 (2005).
4. R. S. Craxton, F. J. Marshall, M. J. Bonino, R. Epstein, P. W. McKenty, S. Skupsky, J. A. Delettrez, I. V. Igumenshchev, D. W. Jacobs-Perkins, J. P. Knauer, J. A. Marozas, P. B. Radha, and W. Seka, *Phys. Plasmas* **12**, 056304 (2005).
5. J. A. Marozas, *J. Opt. Soc. Am. A* **24**, 74 (2007).
6. T. R. Boehly, D. L. Brown, R. S. Craxton, R. L. Keck, J. P. Knauer, J. H. Kelly, T. J. Kessler, S. A. Kumpan, S. J. Loucks, S. A. Letzring, F. J. Marshall, R. L. McCrory, S. F. B. Morse, W. Seka, J. M. Soares, and C. P. Verdon, *Opt. Commun.* **133**, 495 (1997).

7. S. Skupsky, R. W. Short, T. Kessler, R. S. Craxton, S. Letzring, and J. M. Soures, *J. Appl. Phys.* **66**, 3456 (1989).
8. *LLE Review Quarterly Report* **78**, 62, Laboratory for Laser Energetics, University of Rochester, Rochester, NY, LLE Document No. DOE/SF/19460-295 (1999).
9. S. P. Regan, J. A. Marozas, R. S. Craxton, J. H. Kelly, W. R. Donaldson, P. A. Jaanimagi, D. Jacobs-Perkins, R. L. Keck, T. J. Kessler, D. D. Meyerhofer, T. C. Sangster, W. Seka, V. A. Smalyuk, S. Skupsky, and J. D. Zuegel, *J. Opt. Soc. Am. B* **22**, 998 (2005); S. P. Regan, J. A. Marozas, J. H. Kelly, T. R. Boehly, W. R. Donaldson, P. A. Jaanimagi, R. L. Keck, T. J. Kessler, D. D. Meyerhofer, W. Seka, S. Skupsky, and V. A. Smalyuk, *J. Opt. Soc. Am. B* **17**, 1483 (2000).
10. S. Skupsky and R. S. Craxton, *Phys. Plasmas* **6**, 2157 (1999).
11. J. E. Rothenberg, *J. Opt. Soc. Am. B* **14**, 1664 (1997).
12. P. B. Radha, V. N. Goncharov, T. J. B. Collins, J. A. Delettrez, Y. Elbaz, V. Yu. Glebov, R. L. Keck, D. E. Keller, J. P. Knauer, J. A. Marozas, F. J. Marshall, P. W. McKenty, D. D. Meyerhofer, S. P. Regan, T. C. Sangster, D. Shvarts, S. Skupsky, Y. Srebro, R. P. J. Town, and C. Stoeckl, *Phys. Plasmas* **12**, 032702 (2005).
13. J. A. Marozas, S. P. Regan, J. H. Kelly, D. D. Meyerhofer, W. Seka, and S. Skupsky, *J. Opt. Soc. Am. B* **19**, 7 (2002).
14. *LLE Review Quarterly Report* **85**, 39, Laboratory for Laser Energetics, University of Rochester, Rochester, NY, LLE Document No. DOE/SF/19460-378, NTIS Order No. PB2006-106656 (2000).
15. P. W. McKenty, J. A. Marozas, V. N. Goncharov, K. S. Anderson, R. Betti, D. D. Meyerhofer, P. B. Radha, T. C. Sangster, S. Skupsky, and R. L. McCrory, *Bull. Am. Phys. Soc.* **51**, 295 (2006).
16. J. W. Goodman, *Introduction to Fourier Optics* (McGraw-Hill, New York, 1988).
17. J. W. Goodman, *Statistical Optics*, Wiley Series in Pure and Applied Optics (Wiley, New York, 1985).
18. J. A. Marozas and P. B. Radha, *Bull. Am. Phys. Soc.* **47**, 99 (2002).

Monoenergetic Proton Radiography Measurements of Implosion Dynamics in Direct-Drive Inertial Confinement Fusion

The goal of inertial confinement fusion (ICF) is ignition and high gain,¹⁻³ which require that a cryogenic deuterium–tritium (DT) spherical capsule be symmetrically imploded. This implosion results in a small mass of low-density, hot fuel at the center, surrounded by a larger mass of high-density, low-temperature fuel.^{2,3} Shock coalescence ignites the hot spot, and a self-sustaining burn wave subsequently propagates into the main fuel region. In the direct-drive approach to ICF, such an implosion occurs in response to a large number of high-power individual laser beams illuminating the surface of a capsule. Understanding and controlling implosion dynamics are essential to ensure the success of the entire implosion process.¹⁻³

Implosion dynamics have been studied experimentally with a number of diagnostics, including x-ray imaging,²⁻⁵ fusion-product spectrometry,⁶ and fusion-product imaging,^{7,8} but none of these provide a complete picture of the time evolution of mass assembly and self-generated electric (E) and magnetic (B) fields.

This article presents new nuclear observations of implosion dynamics for direct-drive spherical capsules on the OMEGA Laser System,⁹ using a novel method of monoenergetic proton radiography.^{10,11} The combination of characteristics in our approach allows us to, first, probe distributions of self-generated E + B fields; second, determine ρR by measuring the energy loss of backlighting protons; and third, sample all the implosion phases from acceleration, through coasting and deceleration, to final stagnation, to provide a more-comprehensive picture of ICF

spherical implosions. The result is the first use of proton radiography to study ICF implosion dynamics. We note that earlier work by Mackinnon *et al.*¹² successfully demonstrated the feasibility of imaging implosions with protons (produced, in his case, by laser–plasma interactions), backlighting plastic (CH) capsules that were imploded by six 1- μm -wavelength laser beams.¹³

The experiment is illustrated schematically in Fig. 114.31. A CH capsule—the imaged subject—had an 860- μm initial diameter, a 20- μm -thick shell, and a 15-atm H₂ gas fill. It was imploded through direct drive with 40 beams of frequency-tripled (0.35 μm) UV laser light. The laser pulse was square, with a 1-ns duration and a total energy of ~ 16 kJ. The individual laser beams were smoothed using a single-color-cycle, 1-THz, two-dimensional (2-D) smoothing by spectral dispersion (SSD), and polarization smoothing (PS).^{14,15} Implosions were backlit with monoenergetic protons (14.7 MeV) generated from D³He-filled, exploding-pusher implosions driven by 19 OMEGA laser beams (details of this technology have been reported elsewhere^{10,11}). The duration of the backlighting was ~ 130 ps, and the relative timing of backlighter and subject implosions was adjusted in each experiment so the proton radiograph would reflect the condition of the subject capsule at a desired time during its implosion. The effective FWHM of the backlighter was ≈ 40 μm (Ref. 10)—the primary limit on the intrinsic spatial resolution of the imaging system. In images of imploded capsules, spatial resolution was degraded somewhat by scattering of the imaging protons as they passed through the capsules.^{16,17}

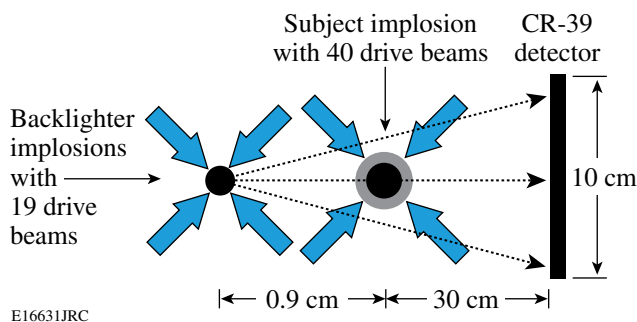


Figure 114.31
Experimental setup, with proton backlighter, subject implosion, CR-39 imaging detectors and laser beams. The field of view at the subject is ~ 3 mm.

Figure 114.32 shows a series of proton radiographs that cover a complete ICF implosion process from beginning through peak compression. Each individual image contains both spatial and energy information because the CR-39 detector records the position and energy of every individual proton. Such images can therefore be displayed to show either proton fluence versus position [Fig. 114.32(a)] or proton mean energy versus position [Fig. 114.32(b)], providing important information about field distributions and capsule compression.

A striking feature of Fig. 114.32(a) is that a central peak occurs in the fluence images during the early stages of implosion ($t = 0.8$ to 1.4 ns), while a fluence dip occurs at the centers at later times ($t = 1.6$ to 2.1 ns).¹⁹ This indicates that trajectories of imaging protons were deflected by radial E fields in the capsule. (Proton trajectories are also altered by scattering in the capsule shell, but this process cannot account for the observed fluence peaks and dips.²⁰) At early times the field must have been centrally directed in order to focus the protons passing within the capsule shell toward the center of the imaging detector. To account for the rapid change from a central fluence peak to a central fluence dip at ~ 1.5 ns, the radial field must have either reversed direction or suddenly become at least three times larger at that time (as shown by Monte Carlo simulations), in which case all protons would strike the detector outside the shadow of the capsule.

An E-field source that is consistent with the data is the gradient of plasma electron pressure ($E \approx -\nabla p_e / en_e$).^{21,22} Other possible sources do not fit as naturally with the data.²³ The pressure gradient has the correct sign at early times, and it reverses direction at about the correct time. This is illustrated in the electron pressure and density profiles at 0.8 ns and 1.9 ns, calculated by the *LILAC* hydro simulation program²⁴ and shown in Fig. 114.33. Using calculated ∇p_e and n_e at different times, we estimate the resultant E-field magnitude in the range $\sim -10^9$ to $\sim 10^8$ V/m, as shown in Fig. 114.34. Figure 114.34 also shows experimental field values deduced from the data of Fig. 114.32(a).²⁵ The predictions match the data in three crucial ways: the field strength and sign before the reversal ($\sim -10^9$ V/m, directed inward), the time of the field reversal (~ 1.5 ns), and the field strength after the reversal ($\sim 10^8$ V/m directed outward). This match leads to a high level of confidence that ∇p_e is the source of the observed phenomena. Note that the detailed structures of the fluence images in Fig. 114.32(a) are also modified, in ways that do not affect our conclusions, by the in-flight movement of the shell ($V_{\text{imp}} \sim -2.5 \times 10^7$ cm/s), which is $\sim 30 \mu\text{m}$ during the backlighter nuclear burn time (~ 130 ps).

Quantitative information about capsule sizes and ρR 's at different times is extracted from the lineouts through the centers of each of the individual images in Fig. 114.32(b); the mean

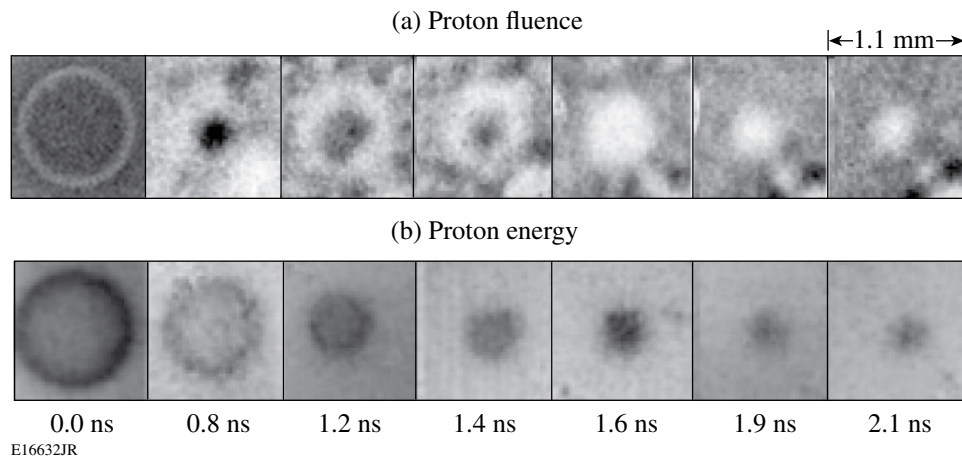
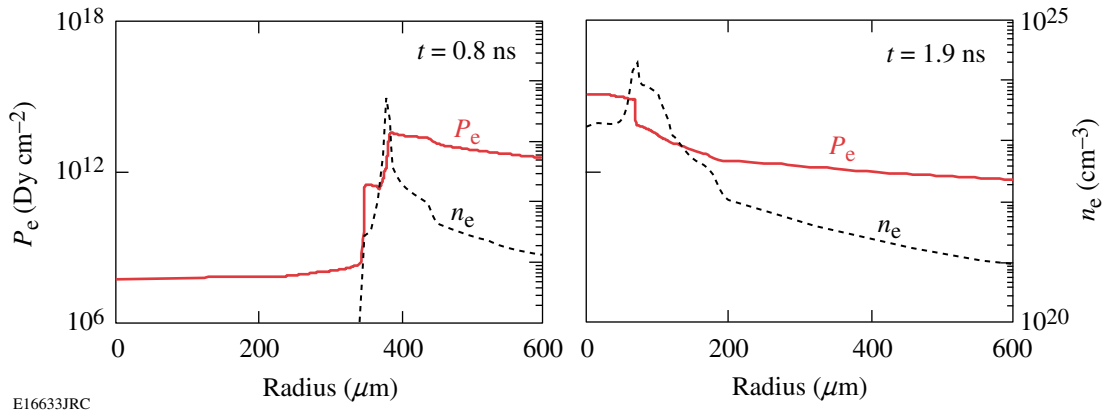


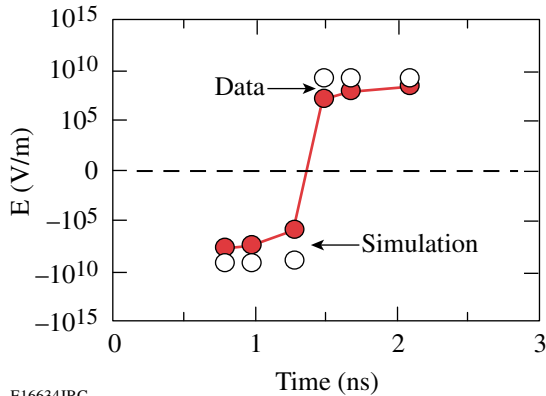
Figure 114.32

Proton radiographs of imploding capsules at different times. Images in (a) show proton fluence (within each image, darker means higher fluence), while images in (b) show proton energy (within each image, darker means more proton energy loss and more matter traversed). The gray-scale mapping for image display is different in each image. Note that the capsule-mounting stalk appears in the lower right corner of each fluence image. Note also that the field of view of these images is only part of the total indicated in Fig. 114.31; the area outside this region is the subject of another study of external fields.¹⁸



E16633JRC

Figure 114.33

 Profiles of electron pressure (solid lines) and density (dashed lines) at 0.8 ns and 1.9 ns, calculated by *LILAC*.


E16634JRC

Figure 114.34

 Radial E fields estimated from experimental measurements (open circles) and from *LILAC* simulations (solid circles) versus implosions times. The differences between simulation and data may result from effects of proton scattering.

width provides the averaged capsule size ($\approx 2R$), while the mean height indicates the total ρL ($\approx 2 \times \rho R$). The measurements are compared with *LILAC* simulations in Figs. 114.35(a) and 114.35(b), respectively. The simulations come reasonably close to matching the observed evolution of capsule convergence and ρR during the acceleration and coasting phases (~ 0 to 1.6 ns), but they predict somewhat smaller values of radius, and larger values of ρR , than measured at the times of nuclear burn (~ 1.9 ns) and peak compression (~ 2.1 ns). Overall, this indicates that the implosions had approximately 1-D performance, with little impact from hydrodynamic instabilities, before deceleration. It has been suggested that performance approaches 1-D because of full single-beam smoothing, which significantly improves the shell integrity during the acceleration phase, and because thickening of the shell during subsequent coasting further enhances shell integrity.¹⁵ The apparent degradation of capsule performance at later times relative to the 1-D simulation could be largely a consequence of fuel-shell mixing and implosion asymmetry.^{2,3}

It is worthwhile to compare these measured ρR values with a value obtained using a completely different method during an equivalent implosion. The open black data point in Fig. 114.35(b) was obtained by using proton spectrometry to determine the energy of self-emitted D^3He protons;²⁶ the downshift in the energy of these protons implies a ρR at bang time of ~ 25 mg/cm². This is slightly higher than the measurement made here but statistically consistent with it given the measurement uncertainties. On the other hand, the spectrometry-implied value is closer to the 1-D value, which raises the possibility that the radiography-implied value loses accuracy when the capsule becomes sufficiently compressed that images are seriously affected by proton scatter. This is currently being investigated, and we plan to develop a more accurate technique for deconvolving the effects of scatter in our analyses.

Finally, the residual mass during the implosion process can be estimated in terms of the measured R [Fig. 114.35(a)] and measured ρR [Fig. 114.35(b)]: $m/m_0 \approx C_r^{-2} \rho R(t) / \rho R(0)$,

where $C_r \equiv R(0)/R(t)$ is the target convergence ratio. This indicates that ~30%–40% of the shell has been ablated by bang time. Although the mass estimates have large uncertainties due to those associated with both R and ρR measurements, they are helpful for illustrating the dynamics of mass ablation during implosions.

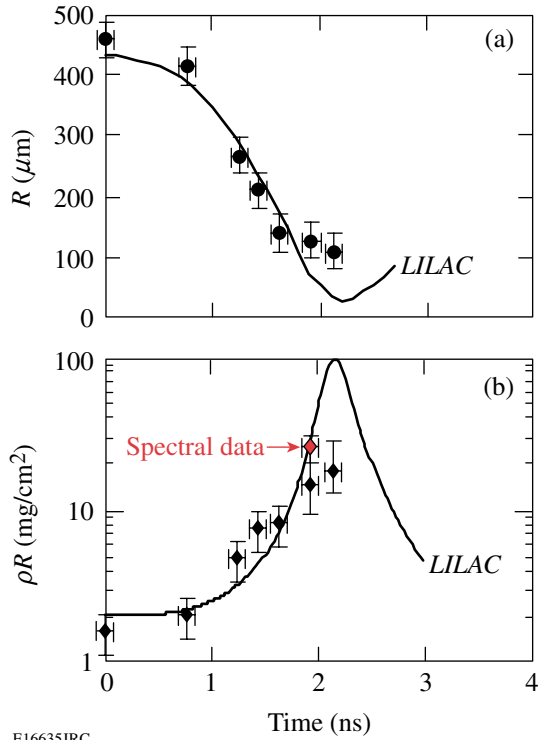


Figure 114.35

Measured capsule radii [(a) solid circles] and ρR [(b) solid diamonds] compared with LILAC 1-D simulations (solid lines). Horizontal error bars represent uncertainties in backlighter burn time. One data point [open diamond in (b)] represents the ρR of a comparable implosion of a D^3He -filled capsule at bang time, measured by several proton spectrometers in different directions; this completely different type of measurement is statistically consistent with the data derived here from radiography images.

In summary, new observations and measurements of direct-drive spherical implosions have been made with time-gated, monoenergetic proton radiography. Quantitative information inferred from proton images characterizes the spatial structure and temporal evolution of an imploding capsule, dynamically displaying a more-comprehensive picture of direct-drive ICF spherical implosions. The observations have also shown the first experimental evidence of radial E fields inside the imploding capsules, as well as their reversal in direction and their probable connection with plasma pressure gradients.

ACKNOWLEDGMENT

The work described here was performed at the LLE National Laser Users' Facility (NLUF) and was supported in part by U.S. DOE (Grant No. DE-FG03-03SF22691), LLE (subcontract Grant No. 412160-001G), LLNL (subcontract Grant No. B504974), the Fusion Science Center for Extreme States of Matter and Fast Ignition Physics at the University of Rochester, and GA under DOE (DE-AC52-06NA27279).

REFERENCES

1. J. Nuckolls *et al.*, *Nature* **239**, 139 (1972).
2. J. D. Lindl, *Inertial Confinement Fusion: The Quest for Ignition and Energy Gain Using Indirect Drive* (Springer-Verlag, New York, 1998).
3. S. Atzeni and J. Meyer-ter-Vehn, *The Physics of Inertial Fusion: Beam Plasma Interaction, Hydrodynamics, Hot Dense Matter*, International Series of Monographs on Physics (Clarendon Press, Oxford, 2004).
4. F. J. Marshall, J. A. Delettrez, R. Epstein, R. Forties, R. L. Keck, J. H. Kelly, P. W. McKenty, S. P. Regan, and L. J. Waxer, *Phys. Plasmas* **11**, 251 (2004).
5. R. S. Craxton, F. J. Marshall, M. J. Bonino, R. Epstein, P. W. McKenty, S. Skupsky, J. A. Delettrez, I. V. Igumenshchev, D. W. Jacobs-Perkins, J. P. Knauer, J. A. Marozas, P. B. Radha, and W. Seka, *Phys. Plasmas* **12**, 056304 (2005).
6. F. H. Séguin, J. A. Frenje, C. K. Li, D. G. Hicks, S. Kurebayashi, J. R. Rygg, B.-E. Schwartz, R. D. Petrasso, S. Roberts, J. M. Soares, D. D. Meyerhofer, T. C. Sangster, J. P. Knauer, C. Sorce, V. Yu. Glebov, C. Stoeckl, T. W. Phillips, R. J. Leeper, K. Fletcher, and S. Padalino, *Rev. Sci. Instrum.* **74**, 975 (2003).
7. L. Disdier, A. Rouyer, I. Lantuéjoul, O. Landoas, J. L. Bourgade, T. C. Sangster, V. Yu. Glebov, and R. A. Lerche, *Phys. Plasmas* **13**, 056317 (2006).
8. F. H. Séguin, J. L. DeCiantis, J. A. Frenje, S. Kurebayashi, C. K. Li, J. R. Rygg, C. Chen, V. Berube, B. E. Schwartz, R. D. Petrasso, V. A. Smalyuk, F. J. Marshall, J. P. Knauer, J. A. Delettrez, P. W. McKenty, D. D. Meyerhofer, S. Roberts, T. C. Sangster, K. Mikaelian, and H. S. Park, *Rev. Sci. Instrum.* **75**, 3520 (2004).
9. J. M. Soares, R. L. McCrory, C. P. Verdon, A. Babushkin, R. E. Bahr, T. R. Boehly, R. Boni, D. K. Bradley, D. L. Brown, R. S. Craxton, J. A. Delettrez, W. R. Donaldson, R. Epstein, P. A. Jaanimagi, S. D. Jacobs, K. Kearney, R. L. Keck, J. H. Kelly, T. J. Kessler, R. L. Kremens, J. P. Knauer, S. A. Kumpan, S. A. Letzring, D. J. Lonobile, S. J. Loucks, L. D. Lund, F. J. Marshall, P. W. McKenty, D. D. Meyerhofer, S. F. B. Morse, A. Okishev, S. Papernov, G. Pien, W. Seka, R. Short, M. J. Shoup III, M. Skeldon, S. Skupsky, A. W. Schmid, D. J. Smith, S. Swales, M. Wittman, and B. Yaakobi, *Phys. Plasmas* **3**, 2108 (1996).
10. C. K. Li, F. H. Séguin, J. A. Frenje, J. R. Rygg, R. D. Petrasso, R. P. J. Town, P. A. Amendt, S. P. Hatchett, O. L. Landen, A. J. Mackinnon, P. K. Patel, V. Smalyuk, J. P. Knauer, T. C. Sangster, and C. Stoeckl, *Rev. Sci. Instrum.* **77**, 10E725 (2006).
11. C. K. Li, F. H. Séguin, J. A. Frenje, J. R. Rygg, R. D. Petrasso, R. P. J. Town, P. A. Amendt, S. P. Hatchett, O. L. Landen, A. J. Mackinnon,

- P. K. Patel, V. A. Smalyuk, T. C. Sangster, and J. P. Knauer, *Phys. Rev. Lett.* **97**, 135003 (2006).
12. A. J. Mackinnon *et al.*, *Phys. Rev. Lett.* **97**, 045001 (2006).
 13. In Ref. 12, Mackinnon reported no fields surrounding the capsule, in contrast to the observations shown here, and this is not presently understood. There are, however, significant differences in the implosion conditions: for example, Mackinnon *et al.* used six beams at 1 μm to irradiate a 250- μm -radius capsule. Herein we used 36 beams at 1/3 μm to irradiate 430- μm -radius capsules. In addition, there are differences in their proton backlighter, such as the fact that the proton spectrum is broadband, a circumstance that will lead to some additional blurring and washout of field structures.
 14. S. Skupsky and R. S. Craxton, *Phys. Plasmas* **6**, 2157 (1999).
 15. D. D. Meyerhofer, J. A. Delettrez, R. Epstein, V. Yu. Glebov, V. N. Goncharov, R. L. Keck, R. L. McCrory, P. W. McKenty, F. J. Marshall, P. B. Radha, S. P. Regan, S. Roberts, W. Seka, S. Skupsky, V. A. Smalyuk, C. Sorce, C. Stoeckl, J. M. Sours, R. P. J. Town, B. Yaakobi, J. D. Zuegel, J. Frenje, C. K. Li, R. D. Petrasso, D. G. Hicks, F. H. Séguin, K. Fletcher, S. Padalino, C. Freeman, N. Izumi, R. Lerche, T. W. Phillips, and T. C. Sangster, *Phys. Plasmas* **8**, 2251 (2001).
 16. V. L. Highland, *Nucl. Instrum. Methods* **129**, 497 (1975).
 17. A simple analytic model¹⁶ can be used to estimate the characteristic scattering angle in radians for protons passing through a plasma with areal density ρL . It is $\langle\theta_{sc}\rangle = z(15\text{MeV}/p\beta c)(\rho L/\rho L_{rad})^{1/2}$, where $z = 1$ for protons, $p\beta c = 30$ MeV for 15-MeV protons, and $\rho L_{rad} = 4.34 \times 10^4$ mg/cm² for carbon. For example, if $\rho L \approx 20$ mg/cm², then $\langle\theta_{sc}\rangle \sim 0.6^\circ$.
 18. F. H. Séguin, C. K. Li, J. R. Rygg, J. A. Frenje, R. D. Petrasso, R. Betti, O. V. Gotchev, J. P. Knauer, F. J. Marshall, D. D. Meyerhofer, and V. A. Smalyuk, "Monoenergetic Proton Radiography Observations of E and B Field Evolution Outside Imploding, Direct-Drive ICF Capsules," in preparation.
 19. It has been confirmed by Monte Carlo simulations of the imaging system that, for a given amount of deflection, the character of focusing or defocusing in the image is relatively insensitive to the specific distance of the detector position.
 20. There are two reasons why scatter cannot account for the observed features: First, simulations show that the Coulomb scattering angles are not large enough to deflect protons to the image center at the earlier times. Second, scatter could not account for the level of fluence reduction seen in the center region at later implosion times. Monte Carlo simulations indicate that proton scattering at later times reduces the central proton fluence in radiographs by $\sim 30\%$ relative to values outside the capsule. The reductions in the actual images [Fig. 114.32(b)] are $\sim 90\%$, indicating that scattering is not the dominant mechanism behind the observed central fluence deficit.
 21. L. Spitzer, *Physics of Fully Ionized Gases*, 2nd rev. ed., Interscience Tracts on Physics and Astronomy (Interscience, New York, 1962).
 22. S. I. Braginskii, in *Reviews of Plasma Physics*, edited by Acad. M. A. Leontovich (Consultants Bureau, New York, 1965).
 23. For example, the charge separation around the convergent shock front due to the imbalance of ion mean free paths between the shocked and unshocked plasmas. This contribution can be ruled out as the dominant source because it will neither reverse direction nor suddenly increase as the data require. (We have ignored contributions from the outgoing shock front at later times due to its relatively weaker strength.)
 24. J. Delettrez, R. Epstein, M. C. Richardson, P. A. Jaanimagi, and B. L. Henke, *Phys. Rev. A* **36**, 3926 (1987).
 25. The electric field E was derived from the images by using $E \sim 2\zeta\epsilon_p(A+a)(eAaL)^{-1}$, where $\epsilon_p = 15$ MeV is the proton energy; e is electron charge; $a = 0.9$ cm and $A = 30.9$ cm are distances from backlighter to implosion and from backlighter to detector, respectively; $|\zeta| \sim (0.5-1) \times R$ is the apparent displacement of protons in the subject plane due to the effects of E on the proton trajectories; and $L \sim (0.5-2) \times R$ is the proton pathlength.
 26. C. K. Li, D. G. Hicks, F. H. Séguin, J. A. Frenje, R. D. Petrasso, J. M. Sours, P. B. Radha, V. Yu. Glebov, C. Stoeckl, D. R. Harding, J. P. Knauer, R. L. Kremens, F. J. Marshall, D. D. Meyerhofer, S. Skupsky, S. Roberts, C. Sorce, T. C. Sangster, T. W. Phillips, M. D. Cable, and R. J. Leeper, *Phys. Plasmas* **7**, 2578 (2000).

High-Dynamic-Range, Single-Shot Cross-Correlator Based on an Optical Pulse Replicator

Introduction

New temporal diagnostics are constantly being developed to match the evolution of optical sources and their applications. Laser systems can now generate optical intensities as high as 10^{21} W/cm² (Ref. 1), and short-pulse laser systems delivering energies higher than 1 kJ are currently being developed.² The characterization of high-energy laser systems is challenging because their repetition rate is usually low. Incoherent processes such as laser and parametric fluorescence can induce significant variations of the intensity from shot to shot. Large shot-to-shot variations preclude the use of averaging and scanning diagnostics. The interaction regime of an optical pulse with a target is set by the peak intensity on target, but the prepulse intensity can significantly influence the interaction. The temporal intensity of the pulse must be known over an extended temporal range (for example, hundreds of picoseconds before the main pulse) with a high dynamic range (for example, eight orders of magnitude below the peak intensity of the pulse). These requirements are currently beyond the capabilities of single-shot optical pulse characterization techniques.^{3–5}

Scanning nonlinear cross-correlators have been used for high-dynamic-range intensity measurements.^{6,7} These diagnostics gate the pulse under test using an instantaneous nonlinear interaction with another optical pulse. The representation of the intensity of the pulse under test is obtained by scanning the delay between the interacting pulses. The scanning range can be very large since it is limited only by the ability to scan the relative delay between optical pulses. The dynamic range is set for each time slot by adjusting the signal level on the detector. For example, a combination of variable attenuation at the input of the diagnostic and variable gain at the detection stage may be used to adapt the signal level before detection. These diagnostics are fundamentally multi-shot devices.

Single-shot cross-correlators using time-to-space encoding have been demonstrated.^{8,9} In these devices, nonlinear interaction in an appropriate arrangement maps the temporal intensity of the pulse under test onto a spatial-intensity distribution, which can be measured in a single shot. If the pulse-front tilt

from a diffraction grating is used,⁹ a large temporal coverage can be obtained. Since photodetectors and analog-to-digital converters are usually limited to a dynamic range of the order of 1000, the different temporal slices of the gated signal were selectively attenuated in Ref. 9 to make it possible to measure a 60-dB dynamic range using a low-dynamic-range detector. In practice, custom, continuous, spatially varying, neutral-density filters would be required to adjust the sensitivity of the device.

This article demonstrates a single-shot cross-correlator based on an optical pulse replicator. The replicator generates a discrete sequence of sampling pulses that are cross-correlated with the source under test in a nonlinear crystal. Advantages of this technique include (1) long temporal ranges, (2) sensitivity adjustments on the sampling pulses using standard neutral-density filters, and (3) constant temporal resolution over the full temporal range of the diagnostic. The remaining three sections describe the design of the cross-correlator, review various experimental results, and present conclusions.

Design of a Single-Shot, High-Dynamic-Range Cross-Correlator Based on a Pulse Replicator

1. General Principle

Following Fig. 114.36(a), the single-shot, high-dynamic-range cross-correlator correlates the pulse under test with a sequence of sampling pulses in a nonlinear crystal, and the spatial intensity of the resulting signal maps the temporal intensity of the input pulse. For the purpose of this explanation and demonstration, the following approximate optical frequencies apply: 1ω for the pulse under test, 2ω for the sequence of sampling pulses, and 3ω for the resulting nonlinear signal. The sampling pulses are temporally delayed and spatially displaced to ensure that the pulse under test is sampled at different times and the nonlinear signals corresponding to different times are spatially distinguishable. These pulses are generated by an optical pulse replicator (OPR) composed of a high reflector (HR) and a partial reflector (PR) appropriately aligned. This arrangement is an adjustable version of a Fabry–Perot etalon with an uncoated entrance window,¹⁰ which has

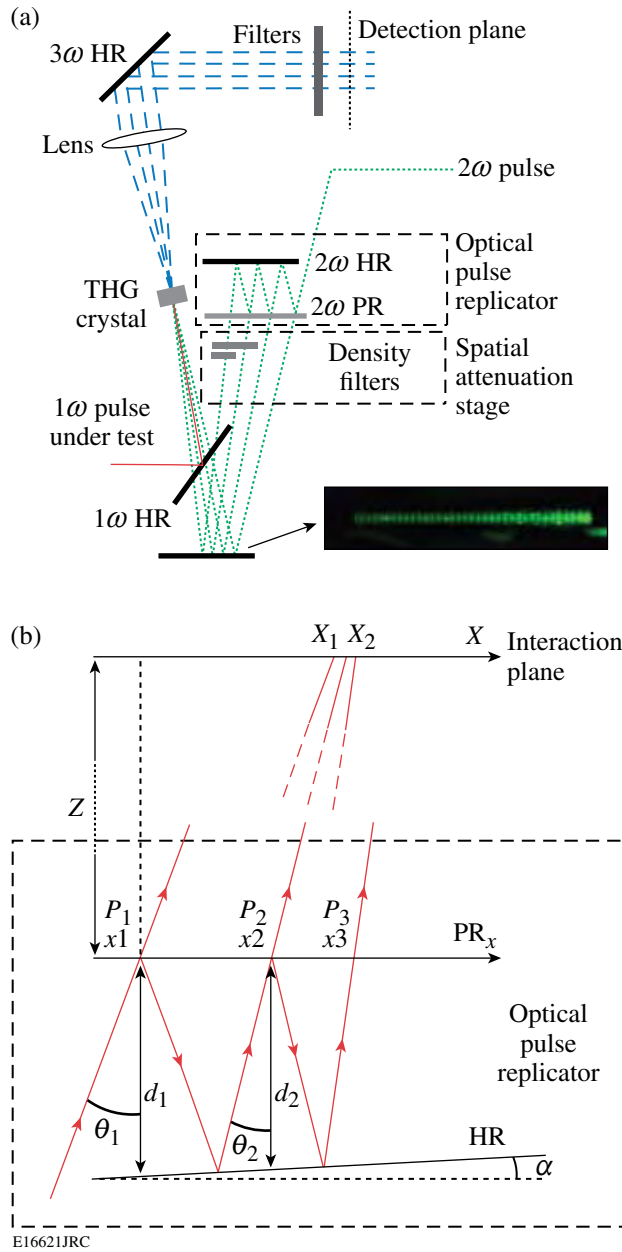


Figure 114.36 (a) Design of a single-shot cross-correlator based on the nonlinear interaction of the pulse under test with a sequence of sampling pulses from an optical pulse replicator. (b) Layout for the calculation of the spatial and temporal properties of the sequence of pulses from the optical pulse replicator. HR: high reflector; PR: partial reflector.

been used to generate discrete sequences of optical pulses.¹¹ In this demonstration, the pulse entering the OPR has an optical frequency of 2ω and has been obtained by doubling the input pulse under test. After the OPR, a set of neutral-density filters can selectively attenuate the sampling pulses corresponding

to high-intensity portions of the pulse under test. This allows one to balance the intensity of the nonlinear signals. The pulse under test and sampling sequence are combined in a quasi-collinear fashion and interact in a third-harmonic-generation (THG) crystal. The time-to-wave-vector encoding performed by the OPR at 2ω at the nonlinear crystal is converted into a time-to-space encoding of the 3ω signals with a lens of focal length f located a distance f away from the nonlinear crystal and the detection plane. This makes it possible to measure each individual signal corresponding to the nonlinear interaction of the pulse under test with each sampling pulse; i.e., the discrete temporal slices gated by the sequence of sampling pulses are located at discrete, spatially distinct locations of the detection plane.

2. Design and Characteristics of the Replicator

The pulse replicator is a combination of a high reflector (HR) and a partial reflector (PR) set to provide a sequence of sampling pulses after multiple reflections. Following Fig. 114.36(b), the input pulse is incident on the PR at point P_1 , and part of the pulse is transmitted, generating the first sampling pulse. The remaining part of the pulse is reflected toward the HR and reflected back by the HR. The beam reflected by the HR is incident on the PR at point P_2 . The pulse transmitted through the PR is the second sampling pulse, and the main part of the pulse is reflected again toward the HR to generate successive sampling pulses. For an energy E_0 at the input of the OPR, the energy of pulse n coming out of the OPR is $E_0 R^{n-1} T$, where R and T are, respectively, the intensity reflection and transmission coefficients of the partial reflector. Assuming $R = 99\%$ and a perfect high reflector, the energy of the first sampling pulse is 1% of the input pulse energy, while the energy of the 50th sampling pulse is 0.61%.

The replicator generates a sequence of sampling pulses that can be used either in the far field (i.e., the pulses are focused in the nonlinear crystal), or in a quasi near field (i.e., the pulses propagate in free space between the replicator and the nonlinear crystal). In the far-field implementation, the beams from the replicator are parallel in the near field and focused to a single point in the far field. This requires a good-quality lens with a large aperture (e.g., 2 in. for a 2-in. OPR). Care must also be taken to optimize the angular phase matching of focused beams. The overlap of multiple beams from the OPR with the pulse under test between beams might also be difficult to achieve. It was found that the sensitivity of the near-field implementation was satisfactory for the targeted application, so the near-field implementation described in the next paragraph was used.

A geometrical treatment of the near-field implementation is shown in Fig. 114.36(b). The two reflectors are set at an angle α . The existence of an optimal angle α for which all the beams from the replicator are in the same vicinity (with a tolerance associated to the beam size) at a given distance from the replicator must be proven. In practice, one of the reflectors can be set on a gimbal/kinematic mount. An interaction plane at a distance Z from the PR, where the nonlinear interaction will take place, is considered. The input beam is incident on the PR at an angle θ_1 in the point P_1 chosen as the spatial origin. The distance between the PR and the HR following a line perpendicular to the PR at point P_1 is d_1 . Naming θ_n and d_n the corresponding quantities for point P_n , one can show that

$$\theta_n = \theta_{n-1} - 2\alpha \quad (1)$$

$$d_n = d_{n-1} \frac{1 - \tan(\alpha)\tan(\theta_{n-1} - 2\alpha)}{1 + \tan(\theta_{n-1})\tan(\alpha)} \quad (2)$$

$$x_n = x_{n-1} + d_{n-1} \frac{\tan(\theta_{n-1}) + \tan(\theta_{n-1} - 2\alpha)}{1 + \tan(\alpha)\tan(\theta_{n-1})}. \quad (3)$$

The sampling pulse coming out of the replicator at point P_n crosses the plane parallel to the PR at a distance Z at the coordinate $X_n = x_n + Z \tan(\theta_n)$. The corresponding optical path length L_n relative to point P_1 is the sum of the length accumulated in the replicator and the length between the PR and the interaction plane. One has the relation

$$L_n = L_{n-1} + \frac{d_{n-1}}{[1 + \tan(\alpha)\tan(\theta_{n-1})]} \times \left[\frac{1}{\cos(\theta_{n-1})} + \frac{1}{\cos(\theta_{n-1} - 2\alpha)} \right] + \frac{Z}{\cos(\theta_n)} \quad (4)$$

with $L_1 = Z/\cos(\theta_1)$. Equations (1)–(4) allow one to calculate the position of the replicas at the interaction plane (i.e., the collection of X_n) and the delays between replicas (i.e., the delays calculated from the collection of L_n). The nonlinear crystal and the 1ω beam can be set to match the average value of the positions X_n of the sampling pulses, and the spatial performance of the OPR depends on the spreading of the X_n relative to their average value. The distance between the two reflectors sets the average delay between replicas (i.e., the sampling rate), and the temporal performance of the OPR depends on the nonuniformity of the sampling rate over the measured temporal range.

Figure 114.37 shows a simulation of the spatial characteristics of a pulse replicator with $\theta_1 = 20^\circ$ and $Z = 1$ m. The results are plotted as a function of the sampling pulse number (between 1 and 50) and angle α . This corresponds to the situation where the distance Z is fixed in the diagnostic and the angle α is tuned. For the particular value $Z = 1$ m, the sampling pulses optimally overlap for $\alpha = 0.31$ mrad. Figure 114.37(b) displays the values of X_n for this value of α . The intersections of the sampling pulses with the reference plane are spread within $300 \mu\text{m}$ of the mean position. Such spreading will have minimal impact provided that it is small relative to the

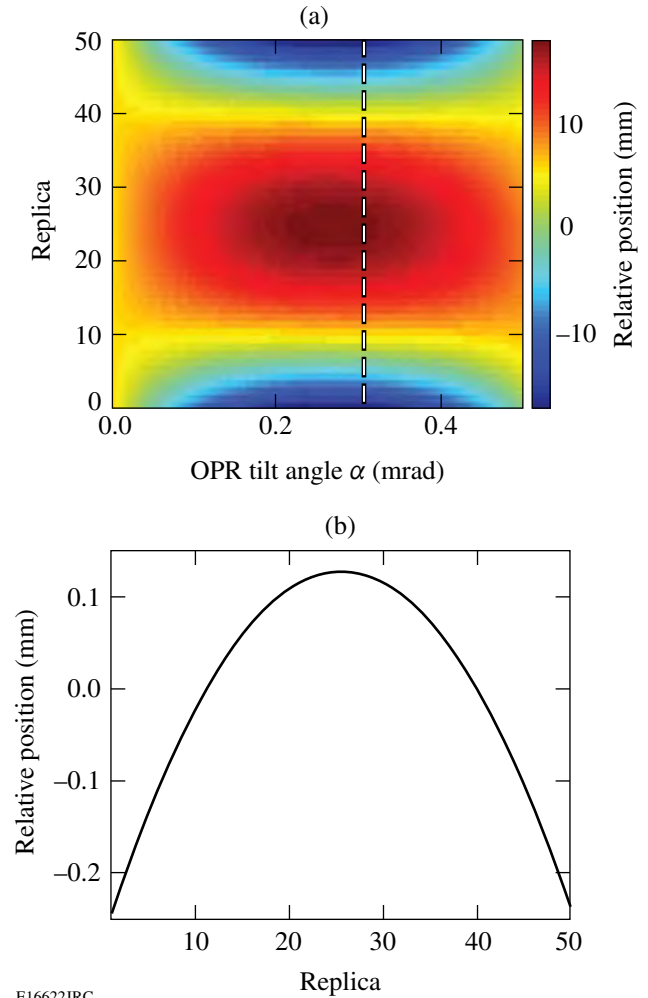
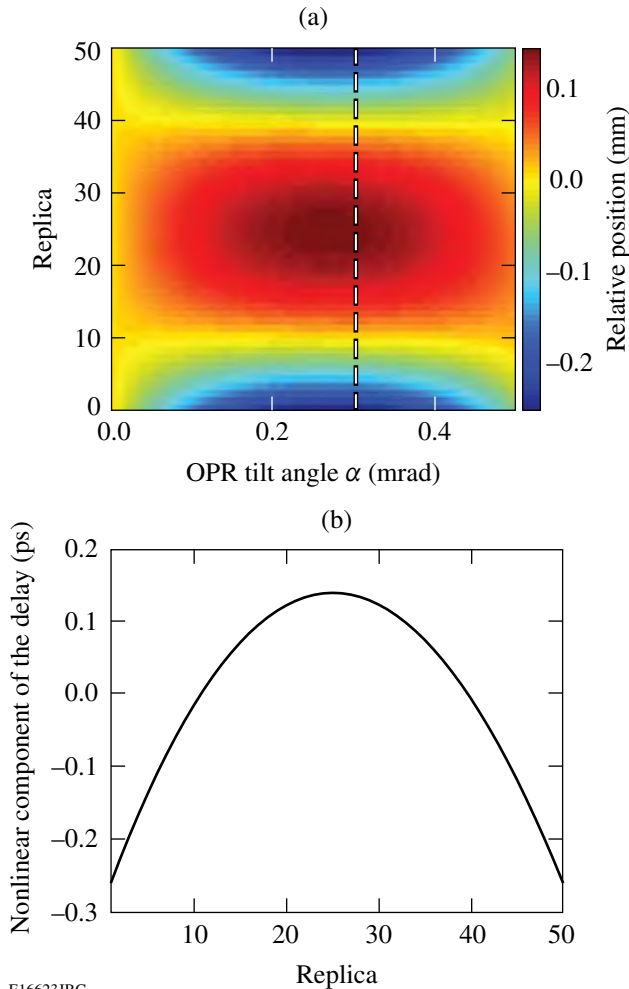


Figure 114.37
(a) Relative position (mm) of 50 replicas from the pulse replicator versus relative angle of the two reflectors of the OPR. The value of α minimizing the spread of the relative positions is indicated by a white dashed line. (b) Relative position of 50 replicas from the pulse replicator for the relative angle minimizing the standard deviation of the relative positions.

size of the interacting beams. Figure 114.38(a) shows the non-uniformity of the sampling rate versus the sampling pulse number. Figure 114.38(b) displays the delay for the value of α leading to the optimal overlap plotted in Fig. 114.37(a). The average delay between replicas is 6.26 ps, and an insignificant change of the sampling rate of 0.3 ps over the 50 replicas is observed. Signal variation due to imperfect spatial overlap can be calibrated, as described in the following section, since it is a property of the diagnostic for a specific input beam size that does not depend on the temporal characteristics of the pulse.



E16623JRC

Figure 114.38

(a) Nonlinear component of the delay (ps) for 50 replicas from the pulse replicator versus the relative angle of the two reflectors of the OPR. The value of α minimizing the spread of the relative positions is indicated by a white dashed line. (b) Nonlinear component of the delay for 50 replicas from the pulse replicator for the relative angle minimizing the standard deviation of the relative positions.

Experimental Results

1. Experimental Setup

A prototype single-shot cross-correlator was built with 2-in. reflectors. The off-the-shelf commercial reflectors have a surface figure of $\lambda/10$ at 633 nm. The partial reflector has $R = 99\%$ at 0° . The angle between the input beam and the reflectors is approximately 20° . The layout is similar to that of Fig. 114.36(a), with a metal mirror between the beam combiner and the THG crystal folding the 1ω and 2ω beam paths to reduce the footprint of the device. The horizontal width of the 2ω beam before replication was reduced by using a telescope to increase the number of replicas produced by the replicator. The distance Z between the OPR and nonlinear crystal is 130 cm. The nonlinear crystal is a 5-mm, type-II DKDP cut for THG ($\theta \sim 59^\circ$). The polarizations of the 1ω and 2ω beams are vertical and horizontal, respectively, and the crystal is oriented accordingly. The angular spread of the 2ω beams after the replicator is in the horizontal direction, which is aligned with the ordinary axis of the crystal to decrease the phase-matching angular variation. The 1ω and 2ω beams are multiplexed vertically with a small angle so that they overlap in the THG crystal.

Optical pulses from a diode-pumped regenerative amplifier (DPRA) operating at 1053 nm were used to demonstrate the single-shot, high-dynamic-range cross-correlator. The DPRA is seeded by a short optical pulse (sub-200 fs) from a mode-locked laser. After amplification and gain narrowing, the amplifier delivers an ~ 8 -ps pulse at 5 Hz with an energy per pulse of approximately $250 \mu\text{J}$. Second-harmonic generation is performed in a 10-mm, type-I lithium triborate (LBO) crystal. The 2ω energy before the replicator is $60 \mu\text{J}$. With the 5-mm DKDP crystal, the noise-equivalent input 1ω energy of the contrast diagnostic is approximately 7 pJ. The sampling pulses need not be derived from the pulse under test, and a low-energy pulse under test could be characterized using sampling pulses generated by another source.

The THG signal is measured with a video camera connected to a frame grabber. The 1ω and 2ω sources are blocked before detection with colored filters. The dynamic range of the diagnostic using this eight-bit frame grabber was determined by measuring the signal corresponding to a single 3ω replica versus input 1ω energy. For a spatially extended 3ω beam, the dynamic range is higher than at each point in the beam because lower-intensity parts of the beam can linearly contribute to the signal even when other parts are saturated. A dynamic range of the order of 30 dB was obtained (Fig. 114.39). Additionally, the 3ω signal versus input 1ω energy was measured when a

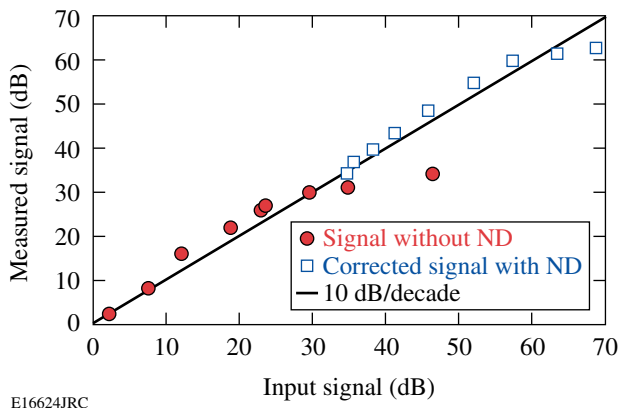


Figure 114.39 Measured 3ω signal versus 1ω signal without neutral-density (ND) filters on the sampling pulse (circles) and with a 30-dB attenuation on the sampling pulse after signal correction (squares). The solid line corresponds to the expected linear relation between the input and output signals.

neutral-density filter with an optical density of 3 was set in front of the 2ω replicas used for up-conversion. As expected from the THG process, the THG signal decreases by three orders of magnitude for the same input 1ω energy, and a 30-dB decrease in the 2ω sampling energy is compensated by a 30-dB increase in 1ω energy. This demonstrates the potential enhancement of the dynamic range of the diagnostic using density filters on specific sampling pulses that are known to correspond to high-intensity portions of the pulse under test. Thanks to the discrete spatial-intensity distribution of the sampling pulses, attenuation can be performed with off-the-shelf density filters. Attenuation of the sampling source, as opposed to the attenuation of the signal after interaction,⁹ was chosen to minimize scattering. Scattering of the sampling pulses at a non-detected wavelength before the nonlinear interaction is preferred over scattering of a high-intensity signal at the detected wavelength after the nonlinear interaction to preserve the high dynamic range of the diagnostic.

The sampling rate was calibrated by temporally scanning the 1ω pulse relative to the train of sampling pulses. The variations of the 3ω signal intensity in each time slot were calibrated using this scan to correct the measured signals. These variations potentially arise from the non-identical spatial overlap of the sampling pulses with the 1ω pulse in the crystal, from the 2ω energy-per-replica variation at the output of the OPR, and from the phase-matching variations in the tripling crystal among different 2ω pulses arriving at different angles.

2. Measurement of a Train of Pulses from a Fabry–Perot Etalon

The intensity and temporal calibration of the diagnostic were tested by inserting a Fabry–Perot etalon in the 1ω optical beam path. The etalon generates a sequence of optical pulses separated by the intracavity round-trip time, 40 ps in this case. Figure 114.40 shows the intensity histogram measured over 1000 shots, which is similar to the infinite-persistence mode of sampling oscilloscopes. Five pulses from the pulse train are well resolved by the diagnostic. As expected, the separation between pulses is approximately 40 ps, and their intensity decreases monotonically. Energy fluctuations from the DPRA can also be seen.

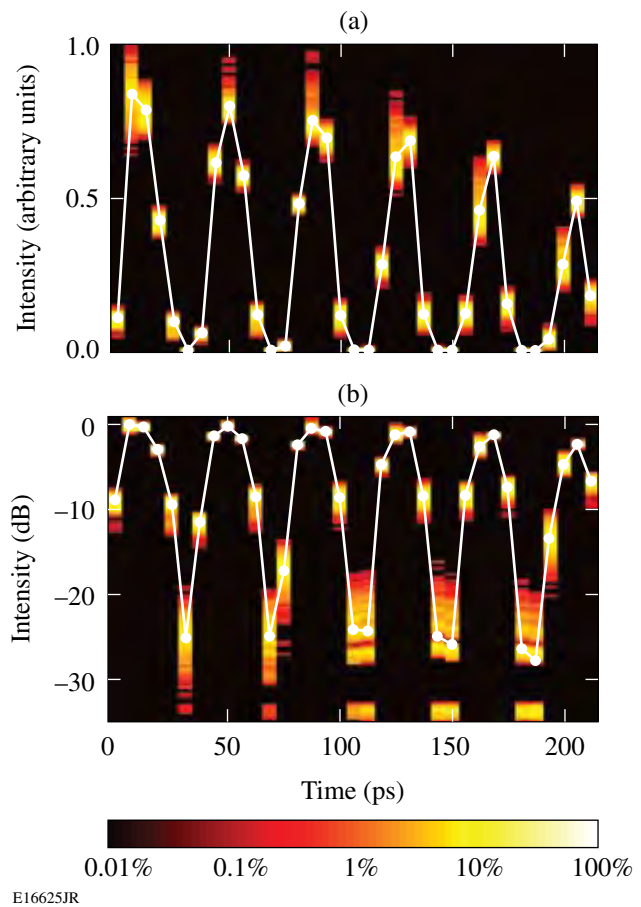


Figure 114.40 Intensity histogram of the output of a Fabry–Perot etalon on (a) a linear scale and (b) logarithmic scale. In each case, the average value of the intensity at each time slot is plotted with white circles.

3. High-Dynamic-Range Measurements

Figure 114.41 demonstrates the high dynamic range of the diagnostic. The sensitivity of the device was adapted to measure

the prepulse contrast. A neutral-density filter with an optical density of 3 at 2ω was set at the output of the pulse replicator to attenuate the seven last sampling pulses, which were timed to coincide with the main pulse from the DPRA. This effectively allows one to map the signal intensity over more than 60 dB onto the detector. The intensity histogram of 10,000 successive shots of the DPRA shows the presence of a prepulse approximately 100 ps before and 40 dB below the main pulse. Amplified spontaneous emission (ASE) has an average intensity approximately 45 dB below the peak intensity of the pulse, although there are large shot-to-shot intensity variations due to the incoherent nature of ASE. Figure 114.42(a) shows the intensity of one DPRA shot, while Fig. 114.42(b) shows the intensity averaged over 10,000 shots.

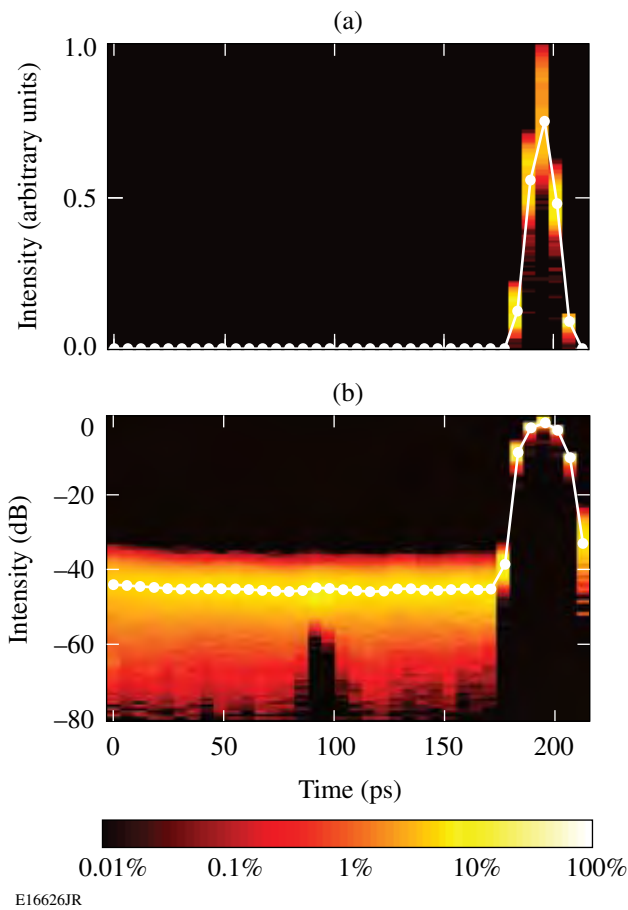


Figure 114.41 Intensity histogram of 10,000 successive shots of the DPRA on (a) linear and (b) logarithmic scales. In each time slot, brighter intensity corresponds to a larger proportion of samples in a given intensity bin. The average intensity is plotted with white circles. A prepulse can be observed approximately 100 ps before the main pulse.

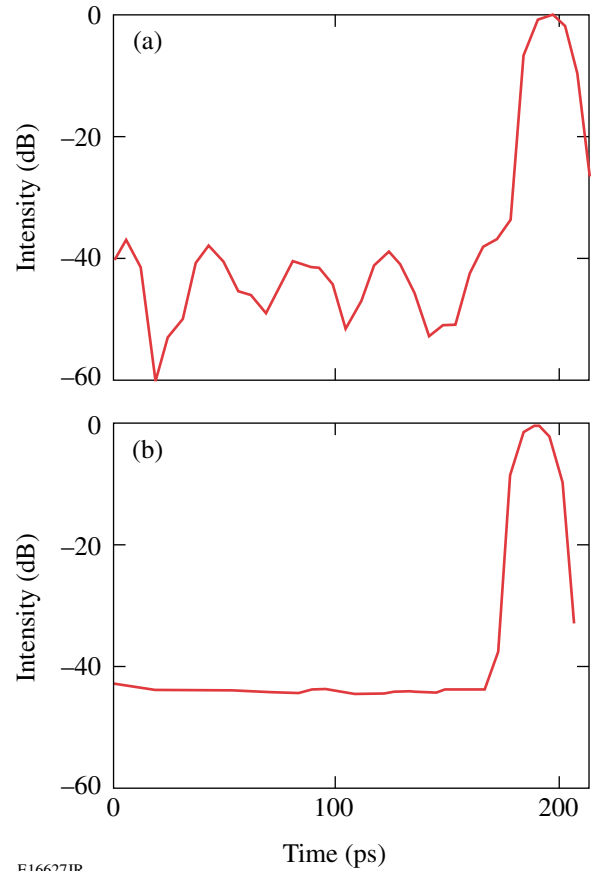


Figure 114.42 (a) Intensity of one DPRA shot and (b) intensity averaged over 10,000 shots.

4. Measurement of Amplified Spontaneous Emission

ASE is a time-stationary incoherent process, and one expects that its statistical temporal properties do not depend on time. The observation window of the cross-correlator was moved significantly in front of the pulse from the DPRA. Figure 114.43 shows the histogram of the measured intensity, with the average value plotted with white circles. Very uniform distribution of the intensity samples can be observed on the linear and logarithmic plots.

5. Statistical Analysis

Incoherent laser and parametric fluorescence are commonly present on high-energy laser pulses. The statistical properties of the intensity of ASE are well documented.¹² For ASE with a degree of polarization equal to 1 (i.e., linearly polarized ASE), the intensity probability density is

$$P(I) = \frac{1}{\langle I \rangle} \exp\left(-\frac{I}{\langle I \rangle}\right), \quad (5)$$

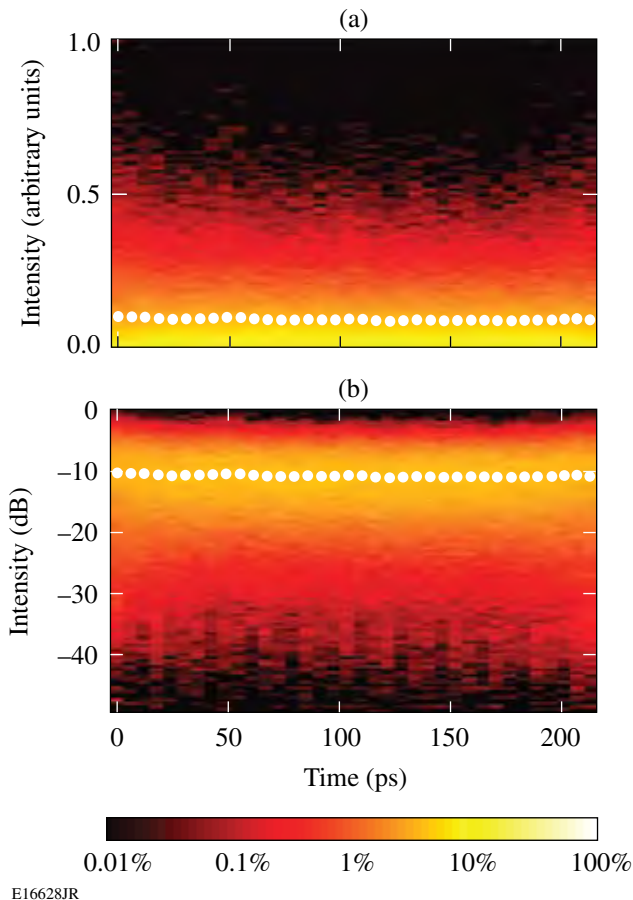


Figure 114.43
Intensity histogram of 10,000 realizations of ASE on (a) linear and (b) logarithmic scales. In each case, the average value of the intensity at each time slot is plotted with white circles.

where $\langle I \rangle$ is the average value of the intensity. Equation (5) is remarkable since it does not rely on any free parameter. A collection of samples of the intensity of an incoherent process should match this distribution and confirm that the measured variations are indeed on the signal under test and are not due to the diagnostic. Figure 114.44(a) shows the measured intensity probability distributions at each of the 36 measured time slots (i.e., 36 different probability density distributions are calculated, each of them using the 10,000 intensity samples measured at a given time). An excellent overlap of the distributions and a good agreement with the expected distribution of Eq. (5) are obtained. Figure 114.44(b) corresponds to the measured intensity probability distribution when all the collected samples (i.e., 36,000 samples) are considered as a single set. An excellent agreement with the expected distribution is again obtained. Figures 114.44(c) and 114.44(d) are logarithmic representations of the data plotted in Figs. 114.44(a) and 114.44(b), respectively. They reinforce the property that accurate intensity measurements are performed over a 30-dB dynamic range.

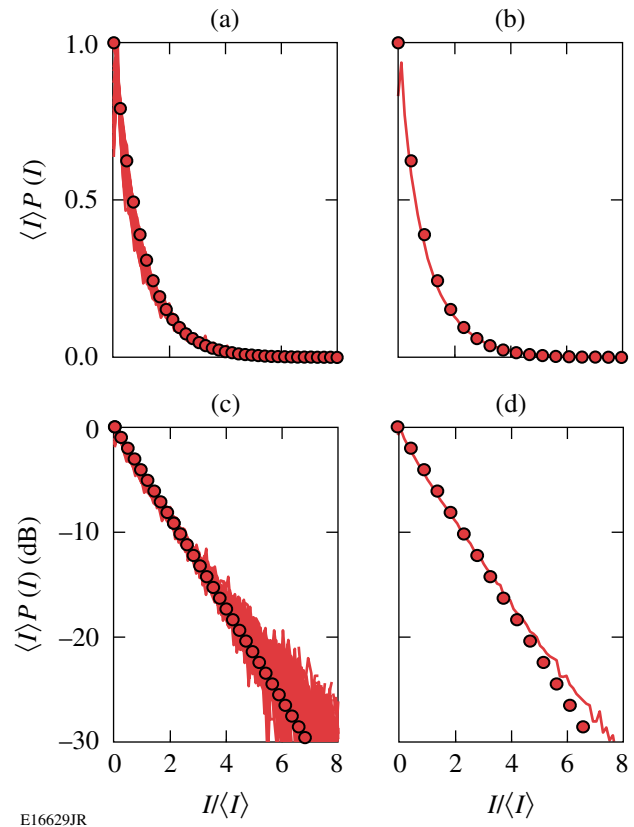
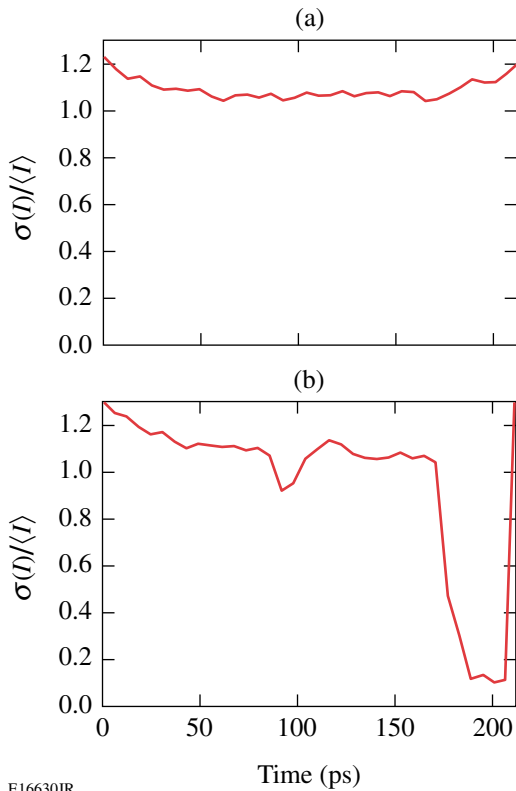


Figure 114.44
Intensity probability density distribution for amplified spontaneous emission. Plots (a) and (c) correspond to an overlap of the distributions obtained at each of the 36 time slots characterized by the diagnostic on a linear and logarithmic scale, respectively. Plots (b) and (d) correspond to the distribution calculated with all the measured samples on a linear and logarithmic scale, respectively. Experimental distributions are plotted with thin solid lines, and the theoretical prediction of Eq. (5) is plotted with circles.

Figure 114.45 displays the normalized quantity $\sigma_N(I) = \sigma(I)/\langle I \rangle$ for the data from Figs. 114.41 and 114.43. For the incoherent process described by Eq. (5), one expects $\sigma_N(I) = 1$. Values slightly higher than 1 are measured, with a slightly increased value at the edges of the measurement range [Fig. 114.45(a)]. Higher noise is attributed to photodetection noise. In these measurements, the signal corresponding to the outer replicas before intensity calibration is lower, and the relative detection noise would be higher. For a coherent process, it is expected that $\sigma_N(I) = 0$, while for a combination of a coherent and incoherent process, all values of $\sigma_N(I)$ between 0 and 1 are achievable. Figure 114.45(b) displays $\sigma_N(I)$ for the data in Fig. 114.41. This quantity is very close to 0 at times corresponding to the main pulse. It is essentially identical to its values in Fig. 114.45(a) at times corresponding to ASE only. The small prepulse approximately 100 ps before the main pulse corresponds to an observable decrease of $\sigma_N(I)$. While the noise at



E16630JR

Figure 114.45

Normalized intensity standard deviation as a function of time for amplified spontaneous emission (in relation to Fig. 114.43) and for a 200-ps window including the main laser pulse (in relation to Fig. 114.41).

these times is small relative to the main pulse, it is significant relative to the intensity of the prepulse.

Conclusion

A single-shot cross-correlator based on a discrete sequence of sampling optical pulses has been demonstrated. Versatile operation has allowed the characterization of different optical sources. The demonstrated high dynamic range (60 dB) and large temporal coverage (200 ps) make this temporal diagnostic a valuable tool to measure the temporal contrast of optical pulses. The capabilities of this cross-correlator can be extended

in various directions. The temporal range can be directly increased by using larger reflectors in the optical pulse replicator. The temporal dynamic range can be improved by increasing the dynamic range of the spatial-intensity measurement of the gated signal. For example, additional optical densities can be used after the pulse replicator to characterize optical sources with higher contrast requirements.

ACKNOWLEDGMENT

This work was supported by the U.S. Department of Energy Office of Inertial Confinement Fusion under Cooperative Agreement No. DE-FC52-08NA28302 and the University of Rochester. The support of DOE does not constitute an endorsement by DOE of the views expressed in this article.

REFERENCES

1. S.-W. Bahk, P. Rousseau, T. A. Planchon, V. Chvykov, G. Kalintchenko, A. Maksimchuk, G. A. Mourou, and V. Yanovsky, *Opt. Lett.* **29**, 2837 (2004).
2. J. D. Zuegel, S. Borneis, C. Barty, B. LeGarrec, C. Danson, N. Miyanaga, P. K. Rambo, C. LeBlanc, T. J. Kessler, A. W. Schmid, L. J. Waxer, J. H. Kelly, B. Kruschwitz, R. Jungquist, E. Moses, J. Britten, I. Jovanovic, J. Dawson, and N. Blanchot, *Fusion Sci. Technol.* **49**, 453 (2006).
3. D. J. Kane and R. Trebino, *Opt. Lett.* **18**, 823 (1993).
4. C. Dorrer, B. de Beauvoir, C. Le Blanc, S. Ranc, J.-P. Rousseau, P. Rousseau, and J.-P. Chambaret, *Opt. Lett.* **24**, 1644 (1999).
5. J. Bromage, C. Dorrer, I. A. Begishev, N. G. Usechak, and J. D. Zuegel, *Opt. Lett.* **31**, 3523 (2006).
6. S. Luan *et al.*, *Meas. Sci. Technol.* **4**, 1426 (1993).
7. E. J. Divall and I. N. Ross, *Opt. Lett.* **29**, 2273 (2004).
8. J. Collier *et al.*, *Laser Part. Beams* **19**, 231 (2001).
9. I. Jovanovic *et al.*, presented at the CLEO/QELS Conference, Baltimore, MD, 6–11 May 2007 (Paper JThD137).
10. C. Dufour, *Rev. Opt.* **24**, 11 (1945).
11. S. Xiao, J. D. McKinney, and A. M. Weiner, *IEEE Photonics Technol. Lett.* **16**, 1936 (2004).
12. L. Mandel and E. Wolf, *Optical Coherence and Quantum Optics* (Cambridge University Press, Cambridge, England, 1995).

Application of Phase Retrieval for Characterizing a High-Intensity Focused Laser Field

Introduction

Focal-spot diagnostics (FSD's) for a high-intensity laser is one of the basic diagnostic requirements for analyzing high-field laser-matter interaction experiments. Many different parameters of a focal spot might be of interest to an experimenter—encircled energy per a given radius, the peak power density of a focal spot, the evolution of local hot spots along the propagation direction, or a full two-dimensional complex-field distribution for a more-comprehensive laser-matter interaction study. The difficulties of implementing focal-spot diagnostics for high-power lasers lie mostly in the necessity of devising an indirect technique because no instrument can survive direct measurements. The indirect technique, therefore, needs thorough qualification regarding how closely it is capable of representing real focal spots.

One of the appealing approaches to FSD is to measure near-field amplitude and phase to predict the field at the focus. This approach can determine the full complex-field distribution at any plane near the focus using well-known diffraction theories. In addition, the on-shot focal spot can be calculated easily without interfering with target experiments. Since the focal-spot is more affected by wavefront error than by fluence error, it is important that the wavefront error be minimized in this approach. One source of wavefront error is the non-common-path aberrations (NCPA's)—the difference between the measured wavefront through the sample beam path and the on-shot wavefront. We designate this difference as “transfer wavefront.” We also designate the aberrations belonging only to the diagnostic path as “intrinsic NCPA's” and the aberrations not captured by the diagnostic setup as “extrinsic NCPA's.” The transfer wavefront is obtained by subtracting the intrinsic NCPA from the extrinsic NCPA.

Transfer wavefront is characterized by sending probe beams through the optical beam path under consideration. There are, in general, two approaches for characterizing transfer wavefront depending on the arrangement of probe sources and the number of wavefront-measurement locations. In the first approach a single probe source, or so-called reference beam, is sent out

to characterize both intrinsic and extrinsic NCPA's; but the wavefronts are measured at two different locations: at the end of the diagnostic beam path and after the final focusing optic in the experimental chamber. This approach was demonstrated in a 100-TW class laser.¹ In the second approach, two probe sources are used at each end of the diagnostic and on-shot path and the wavefront is measured at only a single location, which is at the end of the diagnostic beam path. These two approaches are conjugate to each other in concept. For convenience the first approach is called single-source FSD or FSD-1, and the second is called double-source FSD or FSD-2.

Schematics for both versions of FSD are shown in Fig. 114.46. The on-shot wavefront is measured by a wavefront sensor located at a diagnostic table. The intrinsic NCPA's (W_i) of the measured wavefront are the down-collimator aberrations and other aberrations in the optics located in the diagnostic table. The aberrations from the leaky mirror through the transport optics to the off-axis-paraboloidal (OAP) mirror are extrinsic NCPA's (W_e). In FSD-1, the calibration source as noted in Fig. 114.46(a) is a low-energy reference beam co-propagating with the main beam. The wavefront of this reference beam is measured at the diagnostic table and in the target chamber. The wavefront at location W_2 in the target chamber can be directly measured using a near-field imaging setup.¹ In our case, we chose to use a phase-retrieval method using multiple focal spots measured with a high-resolution focal-spot microscope (FSM) at different longitudinal locations.

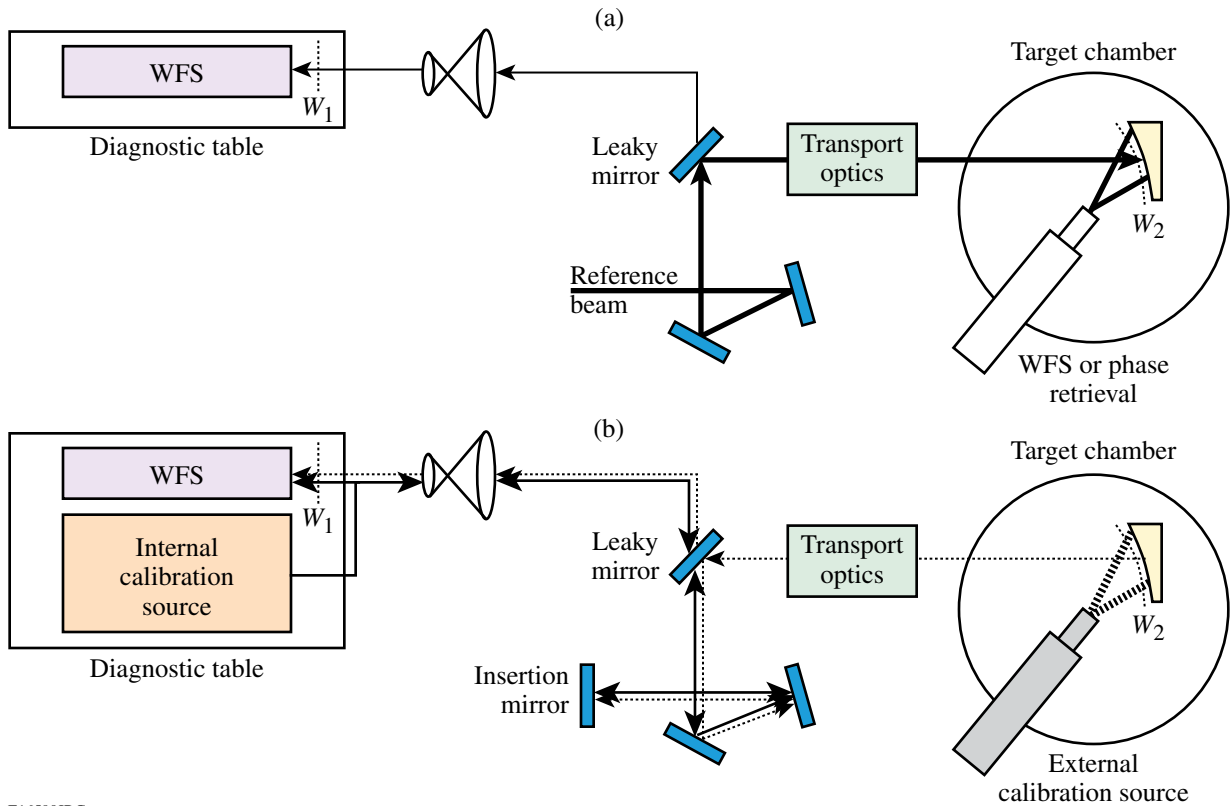
Using a reference beam, at W_1 ,

$$W_{r1} = W_{\text{ref}} + W_i, \quad (1)$$

where W_{ref} is the aberrations in the reference beam itself before the leaky mirror and W_{r1} is the wavefront measured at the sensor location.

At W_2 ,

$$W_{r2} = T(W_{\text{ref}} + W_e) - W_i, \quad (2)$$



E16590JRC

Figure 114.46

(a) FSD-1 uses one calibration source, and wavefronts are measured at two locations to calculate the transfer wavefront. (b) FSD-2 uses two calibration sources, and the wavefront is measured at only one location. WFS: wavefront sensor

where W_{r2} is obtained by the phase-retrieval method or by direct measurement. W_i is an instrument error either in the wavefront-sensor imaging system or in the focal-spot microscope used in the phase retrieval. $T(\cdot)$ is a transformation function describing the spatial coordinate difference and the image distortion after the reflection off of the off-axis paraboloid.² For a large f -number focusing, T can be a simple linear transformation because the distortion is negligible.

The transfer wavefront is

$$W_{\text{transfer}} = W_e - W_i = T^{-1}(W_{r2} + W_t) - W_{r1}, \quad (3)$$

and the on-shot wavefront in the target chamber is calculated as

$$W_{2, \text{on-shot}} = W_{1, \text{on-shot}} + W_{\text{transfer}}. \quad (4)$$

The locations of W_1 and W_2 are shown in Fig. 114.46.

In the FSD-2 approach, the wavefront sensor located at the diagnostic table measures the intrinsic term, characterized by sending a source twice through the diagnostic path reflected

by a temporary insertion mirror [Fig. 114.46(b)]. Let us refer to this quantity as W_s and the source as the “internal calibration source.” If we send another source located at the center of the target chamber backward through the system, the extrinsic term as well as the intrinsic term will be detected at the sensor location. We denote this measured quantity as W_p and call the calibration source “external calibration source”:

$$W_s = W_{i,0} + 2W_i, \quad (5)$$

$$W_p = T^{-1}(W_{e,0}) + W_e + W_i, \quad (6)$$

where $W_{i,0}$ and $W_{e,0}$ are the aberrations that are inherent to the intrinsic and extrinsic calibration sources, respectively. Each has to be measured separately. The inverse transformation is needed to remap the extrinsic source error in a planar space, whereas it is not necessary to apply the inverse transformation to $W_{i,0}$ because the internal calibration source is usually created by a simple on-axis beam collimator that does not distort the beam; it is easily measured by inserting an extra mirror close to the wavefront-sensor location.

The transfer wavefront is calculated as

$$W_{\text{transfer}} = W_e - W_i = (W_p - W_s) - [T^{-1}(W_{e,0}) - W_{i,0}]. \quad (7)$$

A concern with this calibration scheme is the necessity of using a high-power source during the measurement of W_s because of the energy loss associated with the double-pass transmission through the leaky mirror. The main signal might also suffer severe ghost reflections from other optics in the intermediate locations.

In either calibration procedure, the resulting transfer wavefront map should cover the on-shot main beam in the area for the calibration map to be meaningful. The advantage of FSD-2 is that beam registration is automatic and it is easy to subtract and add wavefronts from the internal or external source. However, in the presence of non-negligible aberrations in the external calibration source, the registration task becomes non-trivial and one might have to apply the distortion transformation. Also, the requirement that the two calibration beams should be co-propagating without a centering error poses some alignment challenges. FSD-1, however, has the advantage of being insensitive to the aberrations in the reference beam. It also allows a more direct adaptive-optic correction of the incoming beam as a whole due to the presence of a wavefront-sensing scheme after the final focusing optic.

OMEGA EP is a petawatt laser currently being built at LLE. The focal-spot diagnostics for OMEGA EP is based on the FSD-2 approach. Owing to the complexity of the system, there is always a risk that relying on only one approach might limit our capability to characterize the transfer wavefront under certain conditions. Along with the baseline OMEGA EP FSD development, we investigate the feasibility of implementing FSD-1, especially using a phase-retrieval method. In the **Phase-Retrieval Formalism** section that follows, the mathematical formalism of the phase-retrieval method will be discussed. In the **Off-line FSD Test-Bed Results** section (p. 97), the wavefronts at W_2 obtained by FSD-2 and by the phase-retrieval FSD will be compared and shown to agree well with each other, thus confirming the phase-retrieval method. In the **FSD Demonstration in the MTW Laser System** section (p. 99), phase-retrieval FSD will be applied to predict a focal spot in the Multi-Terawatt (MTW) Laser System, which is compared with the direct focal-spot measurements.

Throughout this article the criterion of FSD accuracy is measured in terms of R_{80} error. R_{80} is an encircle radius that captures 80% of the total energy at the focus. Although the true R_{80} value is not known, R_{80} from a direct focal-spot measure-

ment is considered as the true R_{80} for the purpose of R_{80} error calculation. Currently OMEGA EP requires less than 10% error in R_{80} prediction.

Phase-Retrieval Formalism

Phase retrieval is a calculation technique that retrieves phase information from available intensity measurements that are connected by an integral or differential form of a propagation equation. A phase profile is sought that recreates all the measured intensity profiles under the propagation constraint. One can systematically find a solution using one of the search methods typically available from commercial optimization packages. In this section we describe a phase-retrieval method based on multiple near-focus measurements and one near-field fluence measurement. Increasing the number of measurement planes improves the accuracy of the result as well as the dynamic range of the retrieved phase.³

In Fig. 114.47, the measurement schemes and notations are described. A complex near field $g(x,y)$ is focused by a focusing optic with a focal length of F . The focused intensity profiles are measured at N locations defocused from the focus by Δz_k . The complex field at the k th plane (G_k) is calculated by the Fourier transform after multiplying $g(x,y)$ with a defocusing term; $g(x,y)$ is described by the measured near-field intensity $I_0(x,y)$ and an unknown phase, which is to be retrieved. The phase term can be expressed as a sum of basis functions (ξ_n) multiplied by modal coefficients a_n :

$$g(x,y) = \sqrt{I_0(x,y)} \exp\left[i \sum_n a_n \xi_n(x,y)\right]. \quad (8)$$

Here we chose to use modal expansion instead of a point-by-point phase representation. If the two-dimensional phase map is allowed to vary point by point, the retrieved phase is susceptible

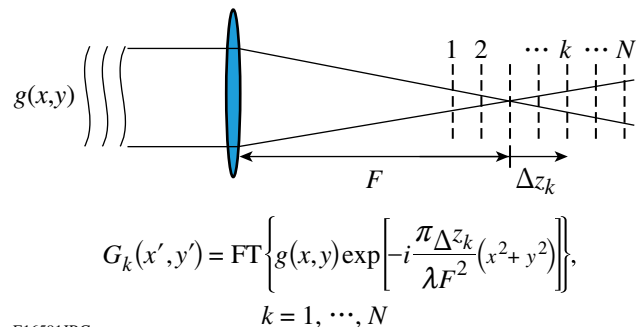


Figure 114.47

Phase retrieval using a multiple-focal-plane intensity measurement.

to discontinuities due to noise in the focal-spot measurements. A modal approach allows one to obtain a smooth phase map but sacrifices resolution for high-spatial-frequency terms not captured by the employed modes. The basis functions commonly used are Zernike polynomials for a circular beam shape or Legendre polynomials for rectangular shapes. For the actual laser beam, which is neither a perfect circle nor a rectangle, one chooses a circle or a rectangle whose size is just large enough to include the whole laser beam. The inner product, however, is defined only within the laser-beam boundary. As long as the beam shape is close to the ideal geometrical figure, this quasi-modal expansion closely represents the original surface.

The error metric to be minimized is

$$\varepsilon(\{a_n\}) = \sum_{k=1}^N \lambda_k \iint [|G_k(x', y')| - \sqrt{I_k(x', y')}]^2 dx' dy', \quad (9)$$

where λ_k is a weighting factor for the measurement plane k . Using the expression of the far field for the k th plane (G_k), the error metric can be seen as a function of the modal coefficients a_n , where we search for a set of coefficients that minimize the magnitude of the error metric. Generally the searching process can be made more efficient when the gradients of the error metric with respect to each search variable are available as an analytic form.⁴ In this case the gradient for the coefficient a_n is

$$\frac{\partial \varepsilon}{\partial a_n} = 2 \operatorname{Imag} \left\{ \iint \operatorname{IFT} \left[\sum_{k=1}^N \lambda_k (G_k - \sqrt{I_k} e^{i\psi_k}) \right]^* \xi_n g \, dx dy \right\}, \quad (10)$$

where IFT is the inverse Fourier transform, ψ_k is the phase of the complex field G_k , and I_k is the measured intensity at the k th plane. The measured intensity usually contains noise that can be negative after background subtraction, so the negative values are set to zero. To measure focal spots, it is ideal to measure intensity by placing a CCD (charge-coupled device) camera directly at the focal planes; however, for low- f -number focusing, a microscope imaging system is needed to resolve a small focal spot. For such a case, the aberrations in the microscope system should be negligible. The modal coefficients for tip and tilt terms are allowed to vary independently for each plane because the mechanical translation is not typically linear. That is, if the number of coefficients to be retrieved is M , the actual number of coefficients that are optimized is $M + 2(N-1)$.

With the error metric and the gradients given, a MATLAB[®] optimization routine (“fminunc”) is used to retrieve the modal coefficients. The routine uses a trust-region approach.⁵ The

typical number of iterations for successful retrieval is less than 20, using five measurement planes.

Off-line FSD Test-Bed Results

Before applying the phase-retrieval method in the MTW Laser System, it was first tested in an off-line FSD test bed where it is possible to compare a directly measured wavefront and a retrieved wavefront. The experimental setup is shown in Fig. 114.48. The setup is designed to mimic basic configurational features of OMEGA EP focal-spot diagnostics; it contains a wavefront sensor, a focal-spot microscope, transport optics, an OAP, down-collimation telescopes, a leaky mirror, and an insertion mirror as well as internal and external calibration sources [Fig. 114.46(b)]. The same wavefront sensor and focal-spot microscope were used in both the test-bed setup and the FSD demonstration in the MTW Laser System.

The wavefront sensor chosen for OMEGA EP is a Shack-Hartmann wavefront sensor—HASO—manufactured by Imagine Optic. It has a 128×128 lenslet array with a 14×14 -mm² CCD sensor area. The focal length of each microlens is 6.3 mm, which can measure local slopes up to 15 mrad. The accuracy of the defocus term was measured to be better than 0.01 waves at $1.053 \mu\text{m}$, and the relative error of astigmatism was found to be within 2%. Accuracy in higher-order aberrations was studied using custom-designed sinusoidal phase plates of one wave peak-to-valley. Wavefront measurements up to one quarter of the maximum spatial frequency were confirmed to be within less than 1% discrepancy with the interferometric measurements. Measurements at higher spatial frequency with the reference phase plates were limited by the maximum slope limit of the sensor.

The prototype FSM consists of a high-quality microscope objective (Mitutoyo, $10\times$, N.A. = 0.26, nominal focal length = 20 mm), a tube lens (nominal focal length = 200 mm), and a scientific-grade, 16-bit CCD camera (SI-800, Spectral Instruments). The microscope objective has a long working distance suitable for high-fluence measurements. The objective is infinity corrected, so a tube lens refocuses the image at the CCD. The actual dynamic range of the camera is reduced to 14 bits due to read noise. The camera was cooled at -35°C in all cases to minimize noise.

The thick black line in Fig. 114.48 represents the main beam line. W_s is measured by the external calibration source placed at the FSM image plane, and W_p is measured by the internal calibration source placed next to the wavefront sensor. W_2 is calculated according to Eq. (4). All the calibration beams and

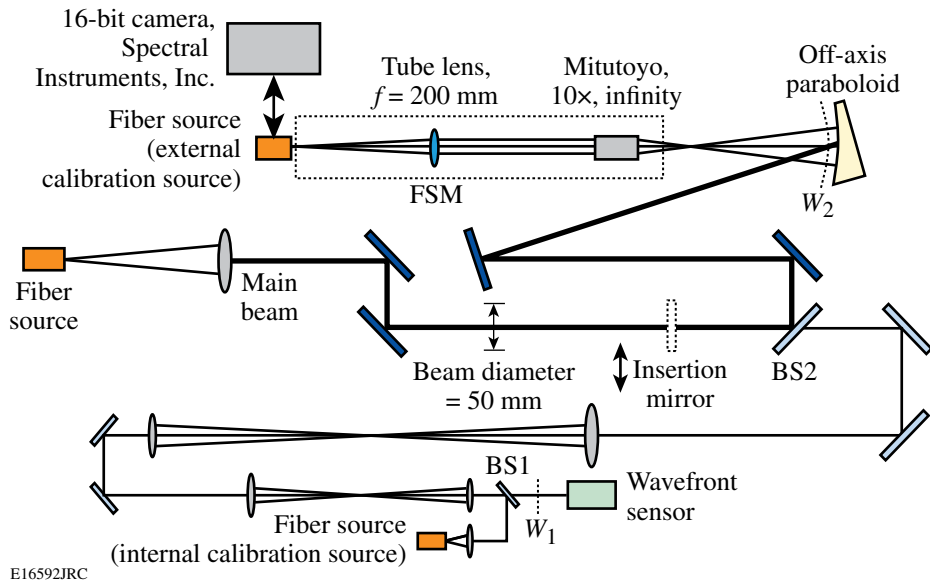


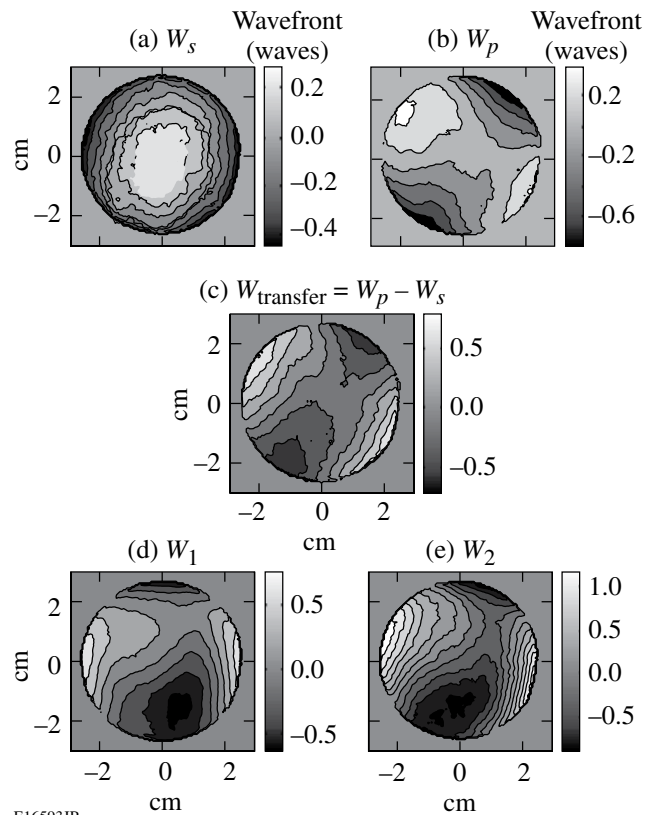
Figure 114.48

The test-bed setup with a geometry similar to the OMEGA EP FSD setup. BS: beam splitter; FSM: focal-spot microscope unit.

the main beam source are obtained from collimating the diverging beam from a single-mode fiber tip injected with a 1053-nm continuous-wave laser. The main beam is a 2-in.-diam round beam down-collimated at the sensor location by a factor of 5. The beam is attenuated before the fiber sources so there are no filter-induced aberrations in the setup. The whole setup was covered with acrylic glass to prevent measurement corruption from air turbulence. The lenses in the two down-collimators and the collimator lens for the main beam were intentionally tilted to introduce aberrations. The main beam is focused by a 200-mm effective-focal-length OAP mirror and the focus is imaged to the FSM.

Figure 114.49 summarizes the wavefronts measured by the FSD-2 procedure. The measured and the calculated focal spots are also shown in Fig. 114.50. The fine details of the calculated focal spot are in excellent agreement with those of the measurement, but the relative R_{80} discrepancy (12%) slightly exceeds the OMEGA EP accuracy requirement (10%) at the best-focus position [Fig. 114.50(d)]. R_{80} errors for five different focal spots measured at $\Delta z = -500, -250, 0, 250,$ and $500 \mu\text{m}$ are $-2.1, -5.4, -12, -6.2,$ and 2% , respectively. It appears that this discrepancy in R_{80} , which is more pronounced near the best-focus position, actually results from an incoherent background halo in the FSM measurements,⁶ which spreads focused light away from the center of focus.

With the direct characterization of wavefront using the FSD-2, we can compare this with the retrieved wavefront from the multiple focal plane phase-retrieval method, which uses the aforementioned five focal-spot measurements. The best-fitting



E16593JR

Figure 114.49

Summary of wavefront measurements in the test-bed setup. (a) W_s , (b) W_p , (c) W_{transfer} , and (d) a wavefront measured at the wavefront sensor location (W_1), and (e) a calculated wavefront after the paraboloidal mirror ($W_2 = W_1 + W_{\text{transfer}}$). The wavefront units are in waves.

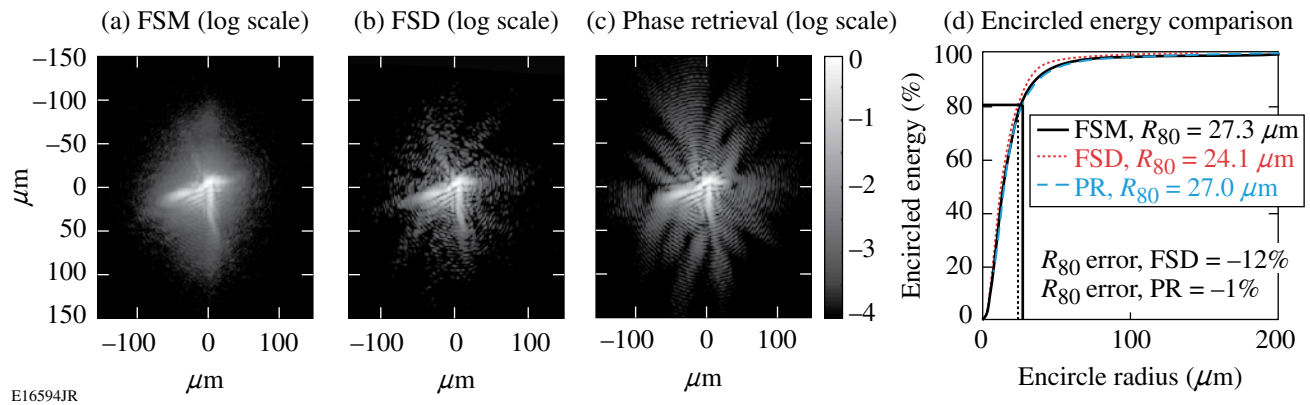
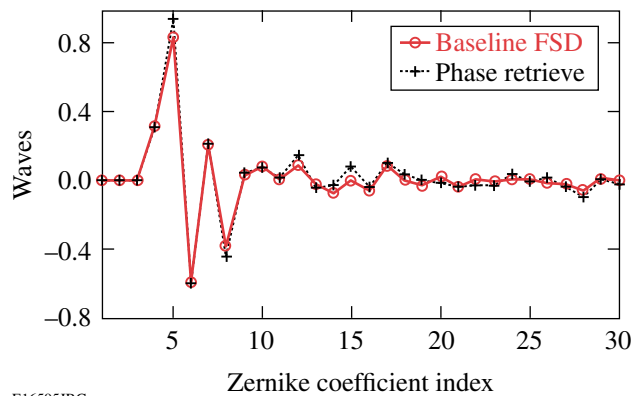


Figure 114.50

The calculated and measured focal spots for the test-bed experiment. (a) Directly measured focal spot by FSM, (b) calculated focal spot based on FSD calibration, (c) calculated focal spot from the retrieved Zernike coefficients, and (d) encircled energy comparisons and the relative R_{80} errors with respect to the R_{80} value of the directly measured focal spot.

Zernike coefficients that minimize the difference between the measured and the calculated focal spots are calculated by an optimization routine. The retrieved wavefront, corresponding to W_2 , agrees well with the W_2 from the baseline FSD. Figure 114.51 compares Zernike coefficients and the wavefront difference. The rms (root-mean-square) difference between the two wavefronts is 0.074 waves. Although one might expect that the R_{80} prediction from the retrieved phase coefficients would have similar errors as in the FSD-2 approach, the R_{80} errors in the five different focal planes in the phase-retrieval case are actually all within 2%. Putting more weight on the direct measurements, it shows that it is possible for the phase-retrieval process to produce a wavefront map that fits all the focal-spot



E16595JRC

Figure 114.51

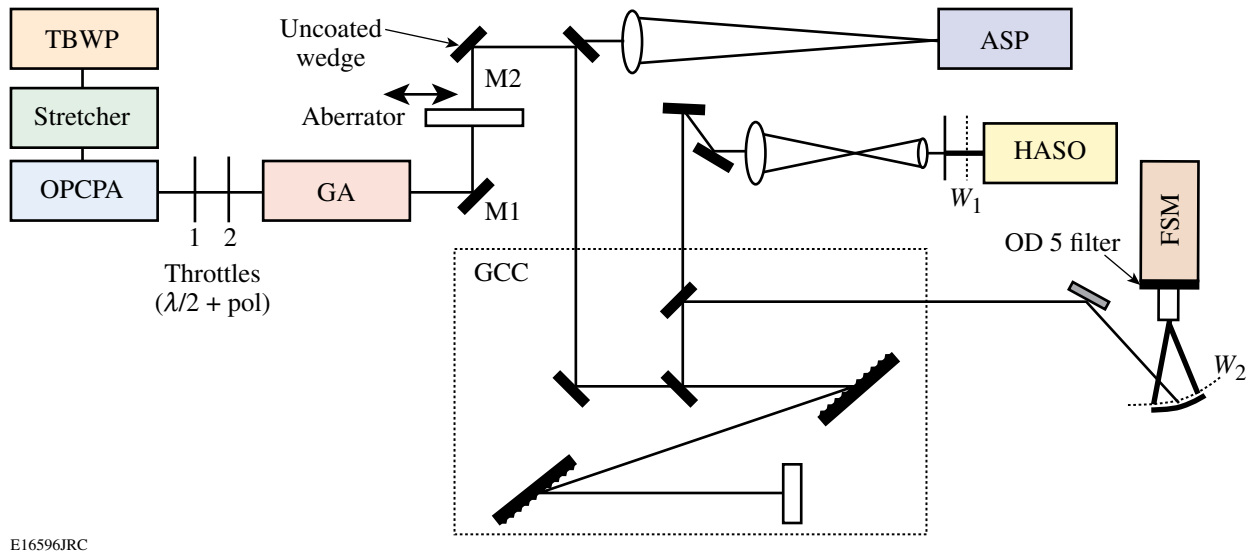
Zernike coefficients from the FSD calibrated wavefront and from phase retrieval from multi-focal-plane data agree well with each other. The rms wavefront difference is 0.074 waves.

data while still being slightly off from the true wavefront. Throughout this experiment the external and internal source errors were assumed negligible; also, the distortion mapping was not applied because the f number (~ 4) is relatively large.

FSD Demonstration in the MTW Laser System

The MTW FSD setup (Fig. 114.52) is based on phase-retrieval FSD (FSD-1) because an external calibration source is not available in the target chamber. In this case the pulse energetics is a practical concern. The attenuation was prepared in three steps; first through wave plates and a polarizer, second by Fresnel reflection off an uncoated wedge (M2), and finally by neutral-density filters inside the FSM. The main glass amplifier was not fired throughout the experiment.

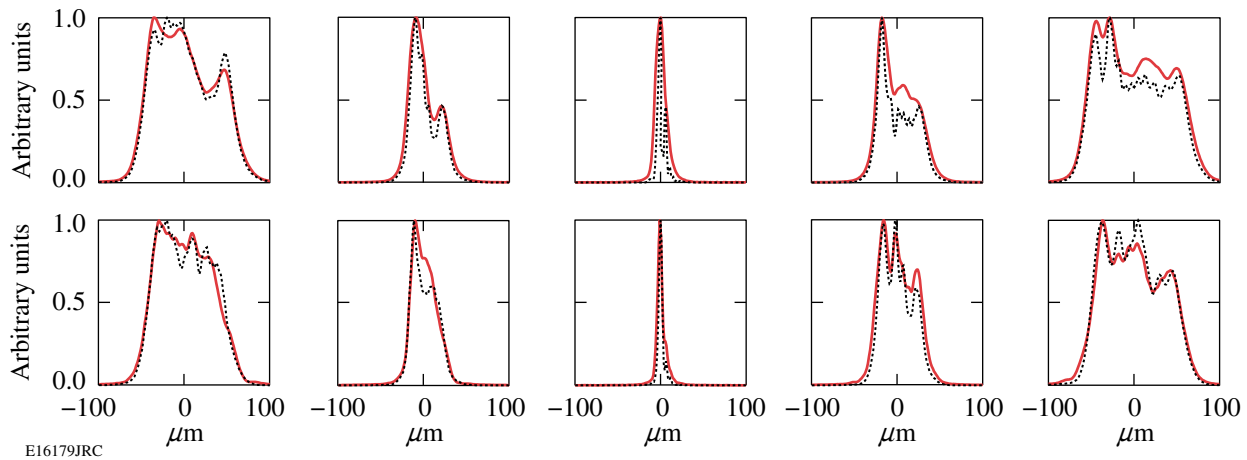
Similar to the FSD test-bed case, the beam is focused by an $f/4$ off-axis paraboloidal mirror; we measured focal spots at five different planes near focus separated by 250 μm . The objective was mounted on a remotely controlled translation stage for operation under vacuum, and the position of the objective was optically monitored using a target-viewing system. We obtained a set of modal phase coefficients that minimize an error metric, which quantifies the difference between the measured data and the intensity computed from the phase estimate, by an optimization routine under the assumption that the field is monochromatic. The modal basis is represented by Legendre polynomials because the beam shape is close to square. Figure 114.53 shows lineout comparisons at each plane after completion of the algorithm. We note generally good agreement in every plane except at the focused plane (first row, third column); the blurring of the focal spot in the horizontal direction is due to angular dispersion caused by a



E16596JRC

Figure 114.52

Experimental setup for a phase-retrieval FSD demonstration in the MTW Laser System. TBWP: a mode-locked oscillator; OPCA: parametric amplifier; GA: 15-cm-thick glass amplifier (inactive); HASO: wavefront sensor; ASP: pointing sensor; GCC: compressor chamber; FSM: focal-spot microscope.



E16179JRC

Figure 114.53

Horizontal (first row) and vertical (second row) lineout comparisons at each plane. The solid lines are from measurements; the dashed lines are from the phase-retrieval calculations. Distances are 500, 250, 0, -250, and -500 μm from the left column to the right.

slight misalignment of the compressor gratings. The angular dispersion was independently measured to be $47 \mu\text{rad}$ over the 7-nm bandwidth by marking the bandpass-filtered focal-spot position change from 1050 nm to 1057 nm. Therefore we find it better to exclude the zero-defocus plane measurement in the search algorithm. On the other hand, the focus plane measurement can be used to estimate the amount of angular dispersion. The amount of angular dispersion estimated from phase-retrieval results is $50 \mu\text{rad}$, which agrees with the independently measured value within 7% relative error.

Once the wavefront of the focusing beam is successfully characterized, this information can be used to characterize focal spots at higher energies by separately measuring the differential wavefront change. As shown in Fig. 114.54, the wavefront sensor on the diagnostic table measures sets of wavefronts belonging to the same beam used in the phase retrieval. The transfer wavefront is calculated according to Eq. (7) [Fig. 114.54(c)]. With the transfer wavefront quantified, the characterization of focal-spot distribution under a different circumstance should be possible by a single wavefront

measurement at the diagnostic table. To validate this idea, an aberrated, transmissive element was placed before the leaky mirror (Fig. 114.52). The directly measured focal spot [Fig. 114.55(a)] morphologically agrees well with the predicted focal spot using the wavefront of Fig. 114.54(e) as shown in Fig. 114.55(b), whereas the agreement is poor without using the transfer wavefront [Fig. 114.54(d) and Fig. 114.55(c)]. The calculated and directly measured focal spots are also compared in logarithmic scale in Figs. 114.56(a) and 114.56(b). The R_{80} error [Fig. 114.56(c)] is 13%, which falls slightly short of the OMEGA EP requirement. The encircled energy of the FSM focal spot shows that it has more energy scattering beyond R_{80} than FSD test-bed measurements; this may result from the extra use of filters in the FSM for attenuating the beam.

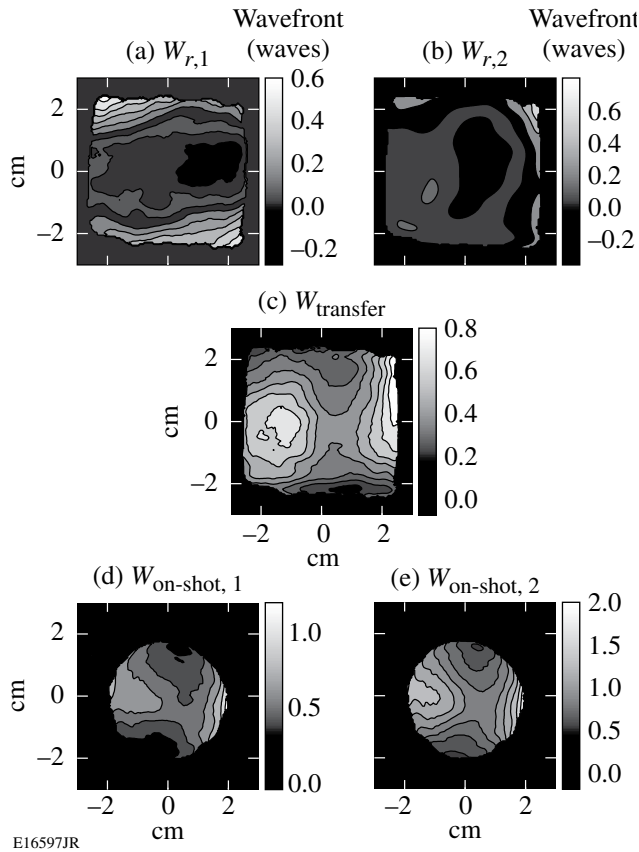
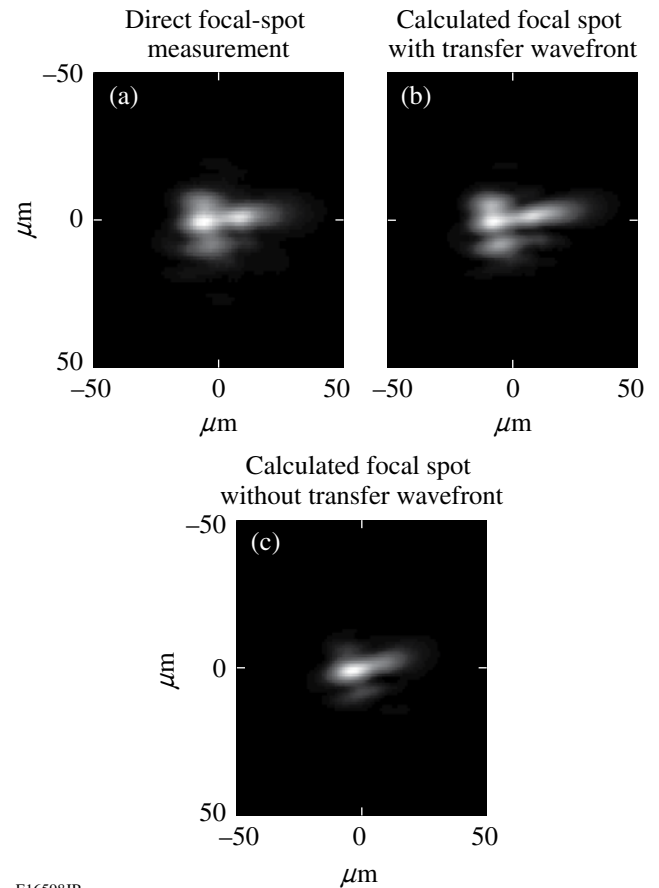


Figure 114.54 Wavefront summary of an OPCPA laser beam. (a) Wavefront measured at the wavefront sensor location, (b) wavefront after OAP reflection, from phase retrieval, (c) transfer wavefront [Eq. (3)], (d) wavefront measured at the wavefront sensor location after the insertion of an aberrator, and (e) calibrated wavefront for the W_2 plane using the transfer wavefront. Wavefront unit is in waves.

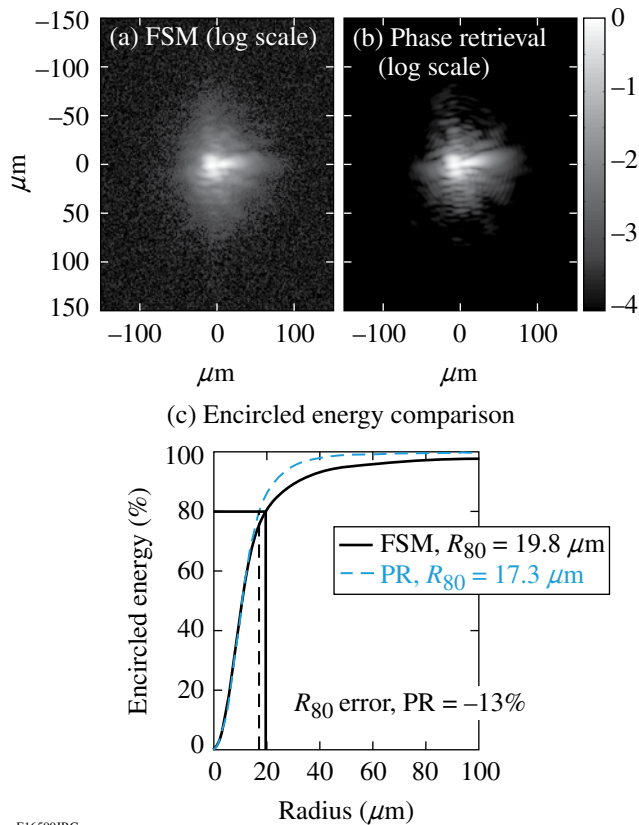


E16598JR

Figure 114.55 Linear scale comparison of the directly measured focal spot (a) in the presence of an aberrator with the calculated focal spot, (b) using the transfer wavefront obtained from phase retrieval, and (c) not using the transfer wavefront.

Conclusions

This work presented focal-spot diagnostic concepts for a high-power laser system, which is based on measuring a near-field complex field for predicting a far field. Since the wavefront at the target chamber is not directly measurable, we demonstrated two calibration procedures to characterize a “transfer wavefront” with which the measured wavefront at the diagnostic table can be easily converted to the actual wavefront at the target chamber location. One FSD approach (FSD-2) is based on direct wavefront measurements using multiple calibration sources, whereas the phase-retrieval FSD (FSD-1) is based on phase retrieval using multiple focal-plane measurements. The two calibration methods were successfully demonstrated in the FSD test-bed setup. The test-bed results show that phase retrieval agrees with the direct measurement within 0.07 waves rms. In the MTW system, the phase-retrieval FSD was applied to characterize the transfer wavefront and a focal



E16599JRC

Figure 114.56

Logarithm scale comparison of the directly measured focal spot (a) in the presence of an aberrator with the calculated focal spot and (b) using the transfer wavefront obtained from phase retrieval. Encircled energy comparisons (c) show 13% of relative R_{80} error.

spot. The disagreement in R_{80} seen in both the test-bed setup and the MTW system suggests that the FSM data may have been corrupted by an incoherent background halo. Currently the R_{80} error is not smaller than 10% from the experimental verification point of view. On the other hand, the availability of the phase-retrieval technique will complement the application of the baseline FSD in OMEGA EP, which might be impaired by system complexity.

ACKNOWLEDGMENT

The authors thank J. R. Fienup for helpful discussions and G. R. Brady for help with numerical implementations. This work was supported by the U.S. Department of Energy Office of Inertial Confinement Fusion under Cooperative Agreement No. DE-FC52-08NA28302, the University of Rochester, and the New York State Energy Research and Development Authority. The support of DOE does not constitute an endorsement by DOE of the views expressed in this article.

REFERENCES

1. S.-W. Bahk, P. Rousseau, T. A. Planchon, V. Chvykov, G. Kalintchenko, A. Maksimchuk, G. A. Mourou, and V. Yanovsky, *Opt. Lett.* **29**, 2837 (2004).
2. S.-W. Bahk, P. Rousseau, T. A. Planchon, V. Chvykov, G. Kalintchenko, A. Maksimchuk, G. A. Mourou, and V. Yanovsky, *Appl. Phys. B* **80**, 823 (2005).
3. V. Yu. Ivanov, V. P. Sivokon, and M. A. Vorontsov, *J. Opt. Soc. Am. A* **9**, 1515 (1992).
4. J. R. Fienup, *Appl. Opt.* **32**, 1737 (1993).
5. T. F. Coleman and Y. Li, *SIAM J. Optim.* **6**, 418 (1996).
6. G. Kuwabara, *J. Opt. Soc. Am.* **43**, 53 (1953).

Optimization of Laser-Damage Resistance of Evaporated Hafnia Films at 351 nm

Introduction

Highly reflective coatings for laser applications in the ultraviolet region of the spectrum pose significant challenges since laser-damage thresholds decrease significantly as the absorption edge of the film materials is approached. Damage initiation at 351 nm for pulsed laser systems in the nanosecond-pulse regime tends to be dominated by the intrinsic absorption of the film materials, as well as defect density and the standing-wave electric-field distribution within the interference structure.^{1–3} High reflectors in the near ultraviolet are typically constructed of oxides, utilizing silica as the low-index material and a refractory oxide as the high-index material. Material selection proceeds to fluorides as the wavelengths continue to become shorter and the absorption in the oxides becomes unacceptable. Silica, while somewhat challenging to evaporate, is a stable, low-absorption, high-laser-damage-threshold material that consistently outperforms the high-refractive-index component in multilayer reflectors.^{1,4} The influence of the electric field distribution is quite well understood, leaving as the primary need improved high-index film materials that may be deposited with low defect density, low absorption, and high laser-damage resistance.^{5,6}

Evaporated hafnia films are of particular interest for large-aperture laser applications due to the relatively high bandgap, ease of scale-up, ability to deposit uniform films, high degree of control throughout the deposition process, and relatively low intrinsic film stress.^{7–10} Adjusting the deposition temperature and oxygen backfill pressure during reactive deposition may modify material parameters such as laser-damage resistance, complex refractive index, and film stress in hafnia/silica multilayers.^{11–13} Furthermore, the use of hafnium metal as a source material provides a cleaner deposition than hafnium dioxide, with fewer ejected particulates, since hafnia undergoes a crystalline phase transition with a rapid change in volume while it is being heated.^{14,15}

The microstructure of the deposited film is also of concern, for both mechanical and optical performance. A weak, loosely bound film structure may be environmentally and mechani-

cally fragile, while potentially exhibiting increased tensile stress.^{16–18} As roughness increases, optical scatter will also increase, reducing the efficiency of lasers incorporating such coatings.¹⁹ In pursuing improved laser-damage resistance of the material, it is important to continue to evaluate the influence that process changes have on these other properties of the overall coating. The structure of an evaporated hafnia film tends to be quite porous, with relatively distinct zone-1 columnar growth.^{20–22} This open microstructure is sensitive to the relative humidity of the use environment and is prone to tensile stress, potentially leading to cracking of the film structure. Ideally, the film microstructure could be deterministically controlled to reduce the environmental influence on film properties as well as achieve a neutral film stress in the final use environment, but there is minimal control over such properties for standard evaporated films. As porosity is increased in the film, there is a corresponding decrease in refractive index, requiring additional layers to achieve desired reflectivity specifications for reflective coatings.

A great deal of effort has been expended in determining the laser-damage mechanisms in hafnia films. The presence of “nanoclusters” of hafnium within the layers, which provide localized heating when irradiated by a laser, has been hypothesized.²³ These defects may be of the order of a few tens of atoms, leading to a reduction in laser-damage resistance as evidenced by localized initiation sites.²³ Modifications to the deposition process that avoid the formation of nanoclusters, or break existing clusters, are expected to lead to significant improvements in the laser-damage resistance of the deposited hafnia.

This effort is centered around the need to improve the laser-damage resistance of multilayer high-reflector coatings for use at a 351-nm wavelength at a 0.5-ns pulse duration. This requires the reduction, or ideally the avoidance, of nanoclusters or nano-absorbers in the growing hafnia layers. Monolayers of hafnia are deposited for characterization by pulsed-laser-damage testing, x-ray diffraction (XRD), transmission electron microscopy (TEM), and spectrophotometry. Ideally, x-ray diffraction will be

capable of resolving the presence of any significant crystalline inclusions within the hafnia films, providing the opportunity to characterize these inclusions for size and composition. The refractive index of the film will also be characterized, in an effort to understand the impact of any changes in deposition conditions with the overall density of the film structure. Finally, multilayer high-reflector coatings will be fabricated by utilizing the established deposition process to determine the influence of the process on the performance of finished mirrors for use in a 351-nm laser.

Experimental Procedure

Depositions of hafnia films were performed in a Vacuum Process Technology (VPT) 56-in., box-type evaporation system (see Fig. 114.57). The system is cryopumped to provide a clean base vacuum of less than 3×10^{-6} Torr. The chamber is equipped with a planetary rotation system and fixed-position uniformity masks to achieve a consistent film-thickness distribution within 1% peak-to-valley. The interior of the chamber is heated using a 12-kW array of quartz heater lamps. Two Ferrotec EV-M8 electron-beam guns are utilized as evaporation sources, one equipped with six 25-cc pockets and the other a 400-cc continuously rotating pan. Deposition control is performed with an Inficon IC5 deposition controller and an array of six quartz-crystal monitor (QCM) heads, with four of

the six used in a weighted average to monitor the evaporant flux from each source. This provides improved noise reduction in the thickness measurement, while averaging measurements in different regions of the chamber to minimize the effects of shifts in the vapor plume.

A cleaved-float-glass sample and a polished fused-silica substrate were placed in substrate fixtures in the planetary rotation system. The cleaved-float-glass substrate provides a virgin glass surface for more accurate determination of the laser-damage threshold, with no contaminants from cleaning or polishing processes.⁴ The polished fused-silica sample is suitable for spectral measurement, x-ray diffraction, or electron microscopy. A shutter system installed on the planet made it possible to load four such pairs of substrates into the system, while only one pair is exposed at any given time. As a result four different sets of deposition conditions can be tested for each pumping cycle of the chamber.

The six-pocket electron-beam gun was loaded with 99.9%-purity hafnium metal supplied by Aran Isles. A monolayer of hafnia, with a nominal layer thickness of 177 nm, was deposited on each pair of substrates. The deposition rate was varied for each value of the oxygen backfill pressure, as outlined in Table 114.I, while the substrate temperature was maintained at 200°C for all depositions.

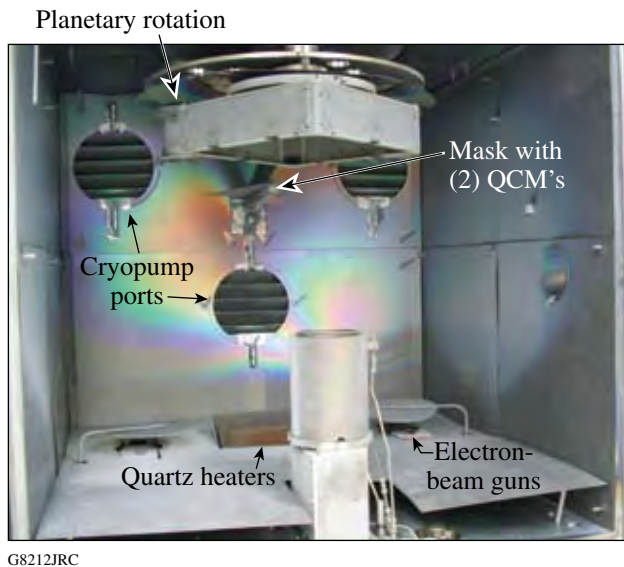
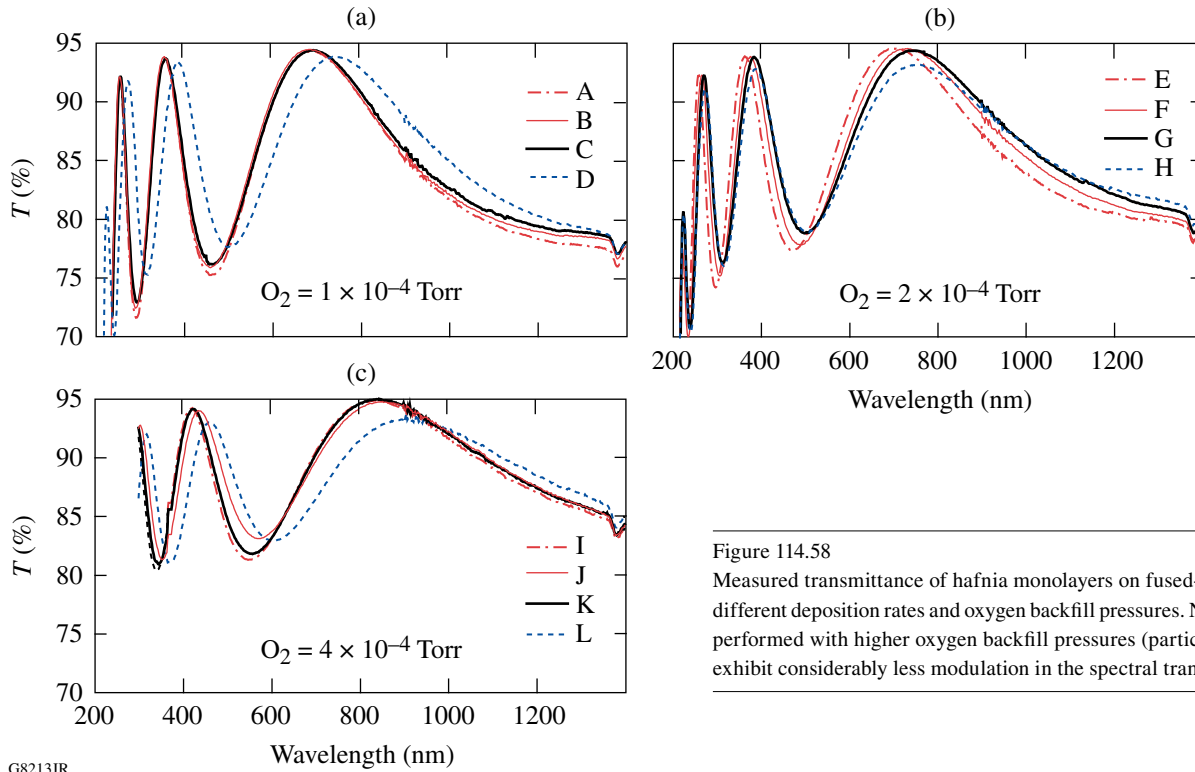


Figure 114.57
The 56-in. evaporation system used to prepare hafnia monolayers. The system uses quartz heater lamps and cryopumps and provides uniform evaporation from the electron-beam guns through the use of planetary rotation and fixed-position uniformity masks. Film-thickness control is achieved with multi-point quartz-crystal monitoring (QCM).

Measurements of Deposited Layers

The performance of the hafnia film was evaluated relative to three primary concerns: spectral/photometric performance, film stress, and laser-damage resistance. Changes in material properties were evaluated based on differences in refractive index, porosity, and crystallinity, as well as imaging of the film structure. The presence of different material phases and inclusions is of particular interest since such differences may significantly impact the laser-damage resistance of the material. Further evaluation of the material properties of the coating, such as relative elemental content or bonding structure, may be pursued in future work but was not undertaken at this time. The influence on film stress will be studied in the future for deposition conditions that yield films with sufficiently high laser-damage resistance.

First, spectral measurements were performed on all fused-silica samples at approximately 40% relative humidity using a Perkin–Elmer Lambda 900 spectrophotometer operating in a normal-incidence transmittance configuration. The transmittance measurements for the coated samples are shown in Fig. 114.58.



G8213JR

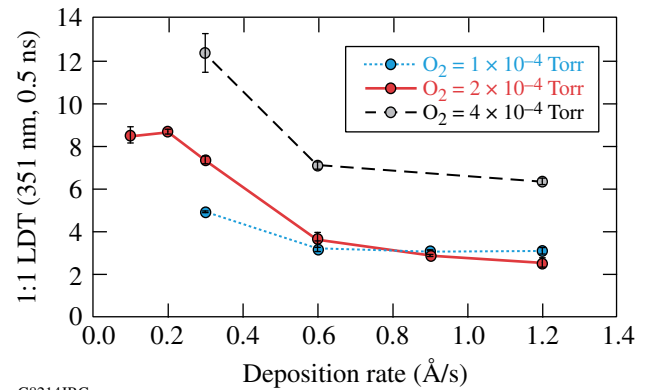
Table 114.I: Sample identifiers A–N are assigned to substrates coated at one of six different deposition rates while using one of three oxygen backfill pressures.

Sample	O ₂ Backfill Pressure (Torr)	Deposition Rate (Å/s)
A	1×10^{-4}	1.2
B	1×10^{-4}	0.9
C	1×10^{-4}	0.6
D	1×10^{-4}	0.3
E	2×10^{-4}	1.2
F	2×10^{-4}	0.9
G	2×10^{-4}	0.6
H	2×10^{-4}	0.3
I	4×10^{-4}	1.2
J	4×10^{-4}	0.9
K	4×10^{-4}	0.6
L	4×10^{-4}	0.3
M	2×10^{-4}	0.1
N	2×10^{-4}	0.2

Figure 114.58

Measured transmittance of hafnia monolayers on fused-silica substrates for different deposition rates and oxygen backfill pressures. Note that depositions performed with higher oxygen backfill pressures (particularly samples I–L) exhibit considerably less modulation in the spectral transmission data.

All of the samples were characterized for their laser-damage resistance at 351 nm, using a 0.5-ns pulsed laser in a standard testing procedure.²³ Samples were tested in both 1:1 and *N*:1 configurations, with multiple threshold measurements used to establish a mean and standard deviation for each sample. Results are shown in Fig. 114.59.

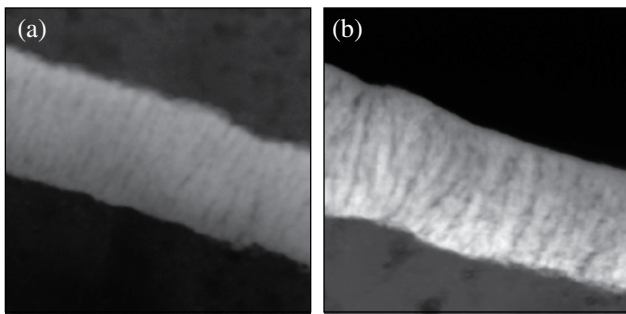


G8214JRC

Figure 114.59

Measured laser-damage resistance of hafnia monolayers (as a function of deposition rate) at 351 nm and 0.5-ns pulse length, tested in 1:1 mode. Note the strong dependence on O₂ backfill at low deposition rates, with the slowest depositions and the greatest O₂ backfill leading to the highest laser-damage thresholds.

To better understand the material changes in the hafnia, samples were prepared for cross-section TEM, to provide high-resolution imaging of the film growth structure. Samples were prepared from multilayers consisting of hafnia layers deposited at 0.3 to 1.2 Å/s, alternated with identical silica layers, to determine the influence of changing process conditions within a single sample. Images of hafnia layers deposited at rates of 0.3 and 1.2 Å/s are shown in Fig. 114.60. Selected area electron diffraction and microdiffraction were used with a spot size of the order of 2 nm in an attempt to ascertain the presence of any crystalline nature to the hafnia material. Neither method was able to distinguish the presence of crystallites, although this may indicate that this method is not sufficiently sensitive on the thin TEM samples to properly evaluate crystalline content of these films.



G8215JR

Figure 114.60

(a) TEM image of a layer of hafnia deposited at 1.2 Å/s in an O₂ backfill of 2.0×10^{-4} Torr. Columns are relatively distinct and perpendicular to the substrate surface. (b) TEM image of a layer consisting of hafnia deposited at 0.3 Å/s in an O₂ backfill of 4.0×10^{-4} Torr. Columns are not as distinct (more branching), and the film exhibits a greater porosity than that deposited at a higher rate. Image is in dark field, 126×126 nm.

Finally, XRD measurements of the hafnia films on samples “E” and “H” were collected using a Phillips MRD diffractometer with a Cu K_α source to evaluate the crystallinity of the hafnia structure. The coated sample was oriented in a near-grazing incidence configuration, with the incident angle $\theta = 2.2^\circ$ and the diffracted angle 2θ incremented in steps of 0.02° , with a 13-s integration time at each position. The resulting scans are shown in Fig. 114.61.

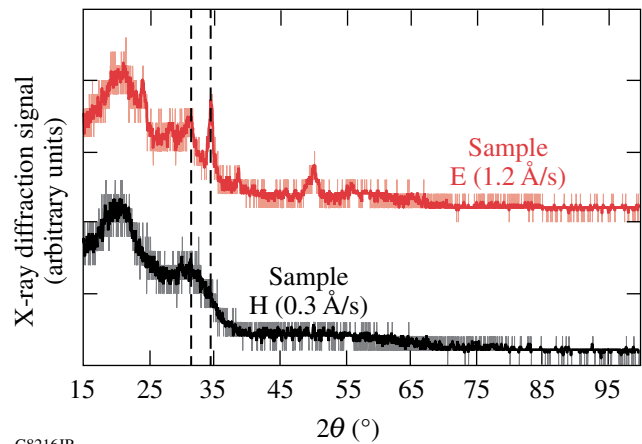
Analysis of Hafnia Performance

The spectral transmission measurements of all of the samples in Fig. 114.58 were analyzed by fitting the measured data to a Sellmeier dispersion relationship, given by²⁴

$$n^2(\lambda) = A_0 + \frac{A_1 \lambda^2}{\lambda^2 - A_2}, \quad (1)$$

where n is the wavelength-dependent real part of the index of refraction, λ is the wavelength, and A_i are the calculated constants allowing the experimental data to be fit. The refractive-index data and film thickness can be used to directly determine the theoretical transmittance of the coating by any of the standard film performance calculations or software.²⁴ The real part of the refractive indices determined for each of the samples is depicted in Fig. 114.62. Reducing the deposition rate decreases the real refractive index, while an increase in the oxygen backfill pressure further decreases the real refractive index. This decrease in refractive index indicates a change in the density of the film, which corresponds to an increase in film porosity. This may be experimentally observed by changes in the mechanical stability of the material and the influence of relative humidity on the film’s optical thickness, which increases for highly porous films.

Results of the laser-damage testing indicate two primary features of interest. First, there is a distinct increase in the laser-damage threshold as the deposition rate is decreased. This was explored further for deposition rates below 0.3 Å/s for a backfill of 2.0×10^{-4} Torr. Deposition rates of 0.2 and 0.1 Å/s exhibited damage thresholds within the measurement



G8216JR

Figure 114.61

X-ray diffraction analysis of hafnia films deposited on silica substrates. Samples were measured in a grazing-incidence configuration, with $\theta_{\text{incident}} = 2.2^\circ$ and 2θ incremented in steps of 0.02° , with a 13-s integration time at each position. The signal is background subtracted and smoothed with a boxcar average to clarify the diffraction peaks. As the deposition rate is increased, there is a clear increase in the crystalline signature for the film.

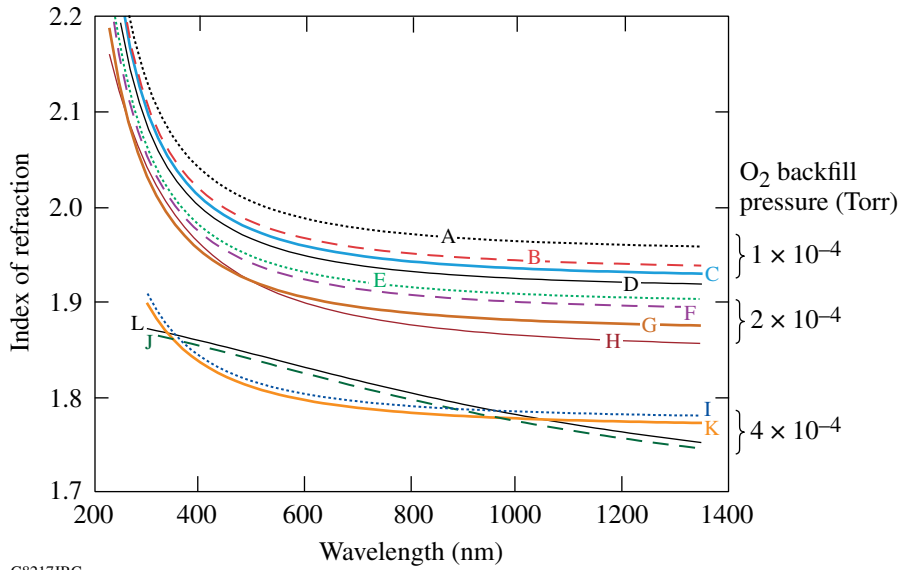


Figure 114.62

Modeled refractive indices for each of the hafnia-coated samples indicate a dependence on O_2 backfill and deposition rate. An increase in the O_2 backfill significantly reduces the hafnia refractive index, while a decrease in the deposition rate provides a lesser reduction in refractive index. Samples prepared with a backfill pressure of 4.0×10^{-4} Torr appear to have an abnormal dispersion curve, with a relatively poor fit to the Sellmeier function. This is likely due to the presence of scatter at shorter wavelengths, which also reduces transmittance.

G8217JRC

uncertainty of each other, indicating that further decreasing the rate below 0.2 \AA/s is not beneficial. Second, the laser-damage resistance at higher deposition rates is independent of the oxygen backfill pressure for the two “typical” backfill pressures (1×10^{-4} and 2×10^{-4} Torr), but a high oxygen backfill pressure of 4×10^{-4} Torr provides a substantial benefit. This likely indicates that the reduction in damage resistance at high deposition rates is not due to oxygen/hafnium adatom arrival ratios, and a resulting improvement in film stoichiometry, but some other effect of the relative deposition rates, such as film density. Hacker *et al.* argue that oxygen in excess of that needed for stoichiometric oxides benefits laser-damage resistance by increasing film porosity due to increased evaporant flux collisions with oxygen that may provide a mechanism for additional oxygen incorporation in the film.³ This excess oxygen influences the behavior of absorptive regions in the film undergoing heating during laser interactions, as well as during recrystallization and oxidation/reduction reactions. It may saturate regions susceptible to damage, providing excess oxygen during melting and cooling, and significantly increasing the probability of formation and preservation of stoichiometric material.

Conversely, laser-damage resistance at very low deposition rates depends significantly on oxygen backfill pressure, denoting the absence of this other effect. It is suggested that this difference in laser-damage resistance is due to the presence, or lack thereof, of nanoclusters of hafnium metal (or oxide) deposited within the film. As the deposition rate is increased, the hafnium source must be heated more aggressively with a

higher electron-beam current. This added energy increases the probability of ejecting very small solid particulates from the source, creating defects that will limit the laser-damage resistance. The laser-damage threshold appears independent of oxygen backfill for rates in the 0.6 to 1.2 \AA/s range, except for the highest backfill pressure of 4×10^{-4} Torr, where there is a dramatic improvement. The reason for this notable improvement is not known but may relate to the interaction of the nanocluster during formation or in the surrounding film structure with the available oxygen. Further investigation is necessary to better understand this phenomenon. As the deposition rate is decreased, and the presence of these nanocluster defects is reduced or eliminated, the absorption in the film becomes the limiting damage criterion and the presence of additional oxygen further improves the film stoichiometry.

XRD Analysis

To verify the potential presence of nanoclusters or other inclusions within the hafnia film, two of the monolayers were characterized using XRD. It was expected that the nanoclusters would exhibit the crystalline nature of the hafnium source material or would be oxidized like the hafnium dioxide film, so these signatures were sought in the diffraction patterns. The size of any crystallites present may be determined based on the peak broadening given by Scherrer's equation:²⁵

$$t = \frac{0.9\lambda}{B \cos \theta_B}, \quad (2)$$

where t is the crystallite size, λ is the wavelength of the x-ray illumination, B is the width of the diffraction peak in radians,

and θ_B is one-half the diffracted angle ($2\theta_B$) of the x-ray radiation. The diffraction patterns of samples E and H are shown in Fig. 114.61.

The first goal in evaluating the films with XRD is to detect the presence of crystalline nanoclusters, but of equal importance is the identification of the phase of any film inclusions. The presence of a metal inclusion, versus an oxide inclusion, should significantly affect the absorption, thermal conductivity, and resulting influence on laser-damage resistance for the component. Samples E and H exhibit a clear difference in crystallinity, as illustrated in Fig. 114.61, although the overall magnitude of the diffraction peaks is quite low, as evidenced by the relative degree of noise surrounding the peaks. The diffraction peaks observed for sample E can be analyzed to determine the phase content in the crystalline inclusions using Philips X'Pert HighScore XRD software.²⁶ Peak locations clearly indicate that the crystalline phase present is hafnium dioxide, not hafnium metal.

The widths of the peaks in the scan of sample E were determined to calculate the size of the crystalline inclusions. The peak at 34.59° has a measured width of 0.47° , but this is actually a double peak as indicated in hafnia reference file 78-0049 of the ICDD database. The peak at 31.44° is a good single peak with a width of 0.96° . This leads to a calculated crystallite size of 9.7 nm, in good agreement with the maximum 10-nm inclusion size determined by thermal modeling of laser-damage morphology.²³

Application to Mirror Fabrication

The ultimate goal of this effort is to produce a mirror with a greater ability to withstand high incident laser fluence at 351 nm. Such a mirror typically consists of alternating quarter-wave optical thicknesses of hafnia and silica, so that constructive interference will lead to greater than 99% reflectivity of the incident intensity. Previous tests of silica monolayers show that the laser-damage resistance is significantly higher than that of hafnia.⁴ The highest laser-damage resistance for a hafnia monolayer in this study was achieved with the lowest deposition rate (0.3 \AA/s) and high oxygen backfill pressure. In order to reduce scatter, the oxygen backfill pressure was limited to 2.0×10^{-4} Torr.

A 23-layer mirror design was established to achieve the desired reflectance at 351 nm at near-normal incidence. The spectral performance of the deposited mirror shown in Fig. 114.63 is shifted to a slightly shorter wavelength than the targeted 351-nm central wavelength.

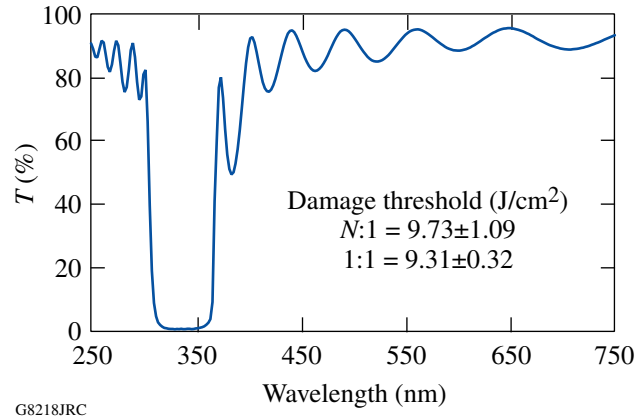


Figure 114.63

Spectral performance of a 23-layer mirror designed for near-normal incidence at 351 nm and produced by the deposition process used for sample H.

Laser-based reflectometry measurements at 351 nm indicate that the reflectivity of the mirror is 99.2% with approximately 0.5% loss due to scatter from the porous film structure. Laser-damage testing of this multilayer at 351 nm and 0.5-ns pulse length yields an $N:1$ threshold of $9.73 \pm 1.09 \text{ J/cm}^2$, while the $1:1$ procedure results in a threshold of $9.31 \pm 0.32 \text{ J/cm}^2$. By comparison, hafnia/silica multilayers prepared with the standard process (hafnia deposition rate of 1.2 to 1.5 \AA/s) in the past four years at LLE have yielded $1:1$ damage thresholds of 1.16 to 5.64 J/cm^2 , with an average threshold of 3.36 J/cm^2 . Even when targeting defects in the improved mirror, the laser-damage resistance is substantially higher than that of any comparable mirror previously produced.

A 31-layer suppressed-electric-field design⁵ was selected to further improve laser-damage resistance in the hafnia layers. The slow-rate deposition technique provides a great deal of flexibility in depositing the coating design since deposition rates and/or oxygen backfill pressures are readily varied for each layer deposited. More-rapid deposition may be utilized for layers interacting with lower-amplitude electric fields, providing not only faster processing, but also minimizing the number of necessary layers and decreasing the surface roughness and associated scatter. The electric-field profile of the outermost 14 layers of this design is illustrated in Fig. 114.64, indicating the deposition rates of any reduced-rate hafnia layers, all of which were deposited with an oxygen backfill pressure of 4×10^{-4} Torr. Laser-damage threshold of this coating undergoing $N:1$ testing reached $13.13 \pm 1.15 \text{ J/cm}^2$, while the $1:1$ procedure resulted in a threshold of $12.11 \pm 0.51 \text{ J/cm}^2$.

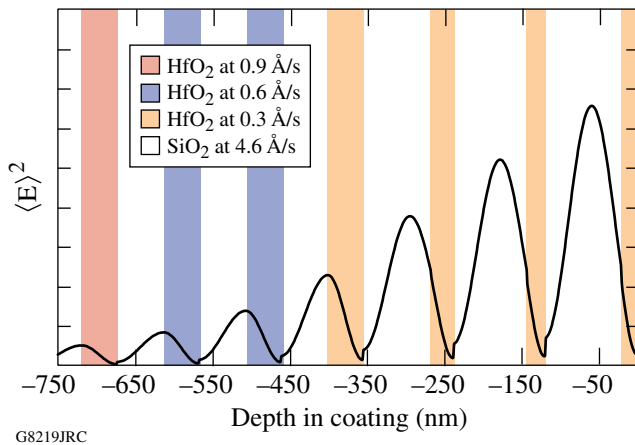


Figure 114.64

Time-averaged electric-field squared in the outer 14 layers of a hafnia/silica reflector designed for 28° incidence, p -polarization at 351 nm. The hafnia layer thicknesses are reduced from typical quarter-wave optical thicknesses in the outer layers to shift the peak electric fields into the more-damage-resistant silica layers. The deposition process is also adjusted to provide maximum laser-damage resistance in regions of the highest standing-wave electric-field intensity.

This testing led to the deposition of production UV transport mirrors (UVHR1 and UVHR2) for LLE's OMEGA EP Laser System. Coatings were produced on BK7 substrates with a measured $N:1$ laser-damage resistance at 351 nm and 0.5-ns pulse duration, ranging from 9 to 16.63 J/cm^2 . Additionally, a strong dependence of laser-damage threshold with respect to relative humidity was noted. The measured laser-damage threshold of a single sample changed from 13.08 to 16.63 J/cm^2 as the relative humidity of the testing environment increased from 24% to 44%, respectively.

Results and Discussion

It is clear that the changes in deposition parameters of evaporated hafnia films significantly alter the refractive index, crystallinity, and laser-damage resistance. XRD makes it possible to quantitatively analyze the film structure, leading to the conclusion that higher deposition rates lead to crystalline inclusions of hafnium dioxide within the amorphous structure. The presence of smaller nanocluster inclusions of hafnium metal has been hypothesized based on laser-damage morphology, but the signature of such inclusions was not observed in the XRD measurements, nor was it apparent in the electron diffraction work. If these nanoclusters are the precursor of damage, then decreasing deposition rate must be reducing the absorption cross-section of the nanoclusters. It is likely that this results from a decrease in the mean size of the nanoclusters con-

tained within the film, or possibly the thermal coupling of the cluster to the surrounding hafnia matrix. A sufficiently gentle evaporation, with a source temperature held very close to the evaporation temperature of the material, provides insufficient energy for the ejection of nanoclusters and improves the overall laser-damage resistance of the material.

The presence of a high oxygen backfill pressure can be expected to scatter coating molecules during transport from the source to the substrate, since the purpose of the vacuum is to increase the mean free path of the coating molecules to avoid this effect. By increasing the oxygen pressure, a greater percentage of the coating will be scattered and the film will condense with less energy at the substrate surface.¹⁷ This energy reduction leads to a more porous film, with reduced mechanical integrity, but, as shown, the laser-damage resistance is significantly improved.

The porosity and resulting influence on the optical properties of the film may explain the relationship between relative humidity and film performance, as past experience has shown a decrease of approximately 2.7% in optical thickness for films in nominal 40% relative humidity versus purged or vacuum environments with approximately 0% relative humidity. This would lead to changes in the standing-wave electric-field profile, altering intensities within the layers and the corresponding damage thresholds. However, it is also possible that the presence of additional moisture increases the available oxygen within the film, decreasing both the hafnium-to-oxygen ratio and the absorption.³

It is expected that chamber geometry and e-beam sweep pattern play a significant role in the rate dependence of hafnia deposition. If the nanocluster explanation is accurate, then chamber geometries that provide a greater deposited film rate for an equivalent source heating would lead to a shifting of the inflection point in the damage graph to higher deposition rates. If the absorption and subsequent damage are primarily due to film non-stoichiometry, then higher deposition rates due to changing geometry should lead to further reductions in laser-damage resistance as oxidation becomes more incomplete. Further investigation of the film structure due to the process modifications, as well as the fundamental cause of the change in laser-damage resistance, is necessary to better understand and utilize these results.

Future Work

Reducing the deposition rate for slow film growth substantially improves laser-damage performance at 351 nm.

Further work is needed to verify the change in the size of the crystalline inclusions, using cross-section and plan-view TEM imaging. Process modifications for e-beam evaporation will be extended to deposition rates below 0.3 Å and higher oxygen backfill pressures during reactive deposition to further improve laser-damage resistance. The influence of the changing film morphology—specifically reduced density leading to potentially higher scatter in the UV—will also be explored to determine the impact on optical and mechanical properties of multilayer coatings. Texture of the film crystallinity should be investigated with XRD to better separate nucleation and film structure from the crystalline signature of film inclusions.

Conclusions

Laser-damage testing of samples processed under different deposition conditions clearly suggests that multiple factors are influencing the damage resistance of the layers. It is hypothesized that, at higher deposition rates, nanoclusters of hafnium metal are ejected from the source and embedded within the growing film, reducing the laser-damage threshold of the material. These clusters are sufficiently small that oxidation is still complete, but the presence of the crystalline inclusion in the overall amorphous structure leads to a degradation of laser-damage resistance. By reducing deposition rates, the range of cluster sizes and the corresponding absorption cross-section is also reduced, enhancing laser-damage resistance. The manipulation of the film porosity and damage resistance through the use of deposition rate and oxygen backfill pressure provides the freedom to modify only those layers interacting with the highest-intensity electric fields, where laser damage is most likely to occur. The use of this process adjustment results in significantly higher laser-damage resistance for multilayer hafnia/silica mirrors at 351 nm.

ACKNOWLEDGMENT

The authors wish to thank Malcolm Thomas (Cornell Center for Materials Research) for support in TEM sample preparation and imaging. This work was supported by the U.S. Department of Energy Office of Inertial Confinement Fusion under Cooperative Agreement No. DE-FC52-08NA28302, the University of Rochester, and the New York State Energy Research and Development Authority. The support of DOE does not constitute an endorsement by DOE of the views expressed in this article.

REFERENCES

1. A. M. Piegari, M. R. Perrone, and M. L. Protopapa, in *Sixth Conference on Optics: 2000*, edited by V. I. Vlad (SPIE, Bellingham, WA, 2001), Vol. 4430, pp. 869–881.
2. M. Reichling, A. Bodemann, and N. Kaiser, *Thin Solid Films* **320**, 264 (1998).
3. E. J. Hacker, H. Lauth, and P. Weissbrodt, in *Laser-Induced Damage in Optical Materials: 1995*, edited by H. E. Bennett *et al.* (SPIE, Bellingham, WA, 1996), Vol. 2714, pp. 316–330.
4. S. Papernov, D. Zaksas, J. F. Anzellotti, D. J. Smith, A. W. Schmid, D. R. Collier, and F. A. Carbone, in *Laser-Induced Damage in Optical Materials: 1997*, edited by G. J. Exarhos *et al.* (SPIE, Bellingham, WA, 1998), Vol. 3244, pp. 434–445.
5. J. H. Apfel, *Appl. Opt.* **19**, 1880 (1977).
6. M. L. Protopapa *et al.*, *J. Vac. Sci. Technol. A* **20**, 643 (2002).
7. J. B. Oliver and D. Talbot, *Appl. Opt.* **45** 3097 (2006).
8. J. B. Oliver, J. Howe, A. Rigatti, D. J. Smith, and C. Stolz, in *Optical Interference Coatings*, OSA Technical Digest (Optical Society of America, Washington, DC, 2001), p. ThD2.
9. J. DiJon *et al.*, in *Laser-Induced Damage in Optical Materials: 1999*, edited by G. J. Exarhos *et al.* (SPIE, Bellingham, WA, 2000), Vol. 3902, pp. 158–168.
10. C. J. Stolz, C. L. Weinzapfel, A. L. Rigatti, J. B. Oliver, J. Taniguchi, R. P. Bevis, and J. S. Rajasansi, in *Advances in Mirror Technology for X-Ray, EUV Lithography, Laser, and Other Applications*, edited by A. M. Khounsary, U. Dinger, and K. Ota (SPIE, Bellingham, WA, 2004), Vol. 5193, pp. 50–58.
11. R. Thielsch, A. Gatto, and N. Kaiser, *Appl. Opt.* **41**, 3211 (2002).
12. B. Andre, J. Dijon, and B. Rafin, U.S. Patent No. 7,037,595 (2 May 2006).
13. H. Leplan *et al.*, *J. Appl. Phys.* **78**, 962 (1995).
14. R. Chow *et al.*, *Appl. Opt.* **32**, 5567 (1993).
15. C. J. Stolz *et al.*, in *Advances in Optical Interference Coatings*, edited by C. Amra and H. A. Macleod (SPIE, Bellingham, WA, 1999), Vol. 3738, pp. 318–324.
16. L. B. Freund and S. Suresh, *Thin Film Materials: Stress, Defect Formation, and Surface Evolution* (Cambridge University Press, Cambridge, England, 2003).
17. M. Ohring, *Materials Science of Thin Films: Deposition and Structure*, 2nd ed. (Academic Press, San Diego, 2002), pp. 723–730.
18. J. A. Floro *et al.*, *MRS Bull.* **27**, 19 (2002).
19. A. V. Tikhonravov *et al.*, *Appl. Opt.* **42**, 5140 (2003).
20. B. A. Movchan and A. V. Demchishin, *Fiz. Met. Metalloved* **28**, 653 (1969).
21. J. V. Sanders, in *Chemisorption and Reactions on Metallic Films*, edited by J. R. Anderson, *Physical Chemistry, A Series of Monographs* (Academic Press, London, 1971), pp. 1–38.
22. J. A. Thornton, in *Modeling of Optical Thin Films*, edited by M. R. Jacobson (SPIE, Bellingham, WA, 1988), Vol. 821, pp. 95–103.

23. S. Papernov and A. W. Schmid, *J. Appl. Phys.* **82**, 5422 (1997).
24. A. V. Tikhonravov and M. K. Trubetskov, OptiLayer Thin Film Software, Optilayer Ltd., <http://www.optilayer.com> (9 June 2005).
25. B. D. Cullity, *Elements of X-Ray Diffraction*, 2nd ed. (Addison-Wesley, Reading, MA, 1978).
26. PANalytical, Inc., Westborough, MA 01581 (see <http://www.panalytical.com>).

Publications and Conference Presentations

Publications

- C. Dorrer and J. Bromage, "Impact of High-Frequency Spectral Phase Modulation on the Temporal Profile of Short Optical Pulses," *Opt. Express* **16**, 3058 (2008).
- O. V. Gotchev, N. W. Jang, J. P. Knauer, M. D. Barbero, R. Betti, C. K. Li, and R. D. Petrasso, "Magneto-Inertial Approach to Direct-Drive Laser Fusion," *J. Fusion Energ.* **27**, 25 (2008).
- J. S. Green, V. M. Ovchinnikov, R. G. Evans, K. U. Akli, H. Azechi, F. N. Beg, C. Bellei, R. R. Freeman, H. Habara, R. Heathcote, M. H. Key, J. A. King, K. L. Lancaster, N. C. Lopes, T. Ma, A. J. MacKinnon, K. Markey, A. McPhee, Z. Najmudin, P. Nilson, R. Onofrei, R. Stephens, K. Takeda, K. A. Tanaka, W. Theobald, T. Tanimoto, J. Waugh, L. Van Woerkom, N. C. Woolsey, M. Zepf, J. R. Davies, and P. A. Norreys, "Effect of Laser Intensity on Fast-Electron-Beam Divergence in Solid-Density Plasmas," *Phys. Rev. Lett.* **100**, 015003 (2008).
- Z. Jiang and J. R. Marciante, "Impact of Transverse Spatial-Hole Burning on Beam Quality in Large-Mode-Area Yb-Doped Fibers," *J. Opt. Soc. Am. B* **25**, 247 (2008).
- K. L. Marshall, K. Hasman, M. Leitch, G. Cox, T. Z. Kosc, A. Trajkovska-Petkoska, and S. D. Jacobs, "Doped Multilayer Polymer Cholesteric-Liquid-Crystal (PCLC) Flakes: A Novel Electro-Optical Medium for Highly Reflective Color Flexible Displays," in the *SID 07 Digest*, edited by J. Morreale (Society for Information Display, San Jose, CA, 2007), Vol. XXXVIII, Book II, pp. 1741–1744.
- K. L. Marshall, A. Trajkovska-Petkoska, K. Hasman, M. Leitch, G. Cox, T. Z. Kosc, and S. D. Jacobs, "Polymer Cholesteric-Liquid-Crystal (PCLC) Flake/Fluid Host Electro-Optic Suspensions and Their Applications in Color Flexible Reflective Displays," in the *Proceedings of The International Display Manufacturing Conference 2007*, edited by C. H. Chen and Y.-S. Tsai (Society for Information Display, Hsinchu, Taiwan, 2007), pp. 70–73.
- A. V. Okishev, V. I. Smirnov, L. B. Glebov, and J. D. Zuegel, "An Optical Differentiator Based on a Regenerative Amplifier with an Intracavity Tunable Volume Bragg Grating Amplifier," in *Advanced Solid-State Photonics on CD-ROM* (Optical Society of America, Washington, DC, 2008), Paper WE32.
- O. Okunev, G. Chulkova, I. Milostnaya, A. Antipov, K. Smirnov, D. Morozov, A. Korneev, B. Voronov, G. Gol'tsman, W. Slysz, M. Wegrzecki, J. Bar, P. Grabiec, M. Górska, A. Pearlman, A. Cross, J. Kitaygorsky, and R. Sobolewski, "Registration of Infrared Single Photons by a Two-Channel Receiver Based on Fiber-Coupled Superconducting Single-Photon Detectors," in the *Second International Conference on Advanced Optoelectronics and Lasers*, edited by I. A. Sukhoivanov, V. A. Svich, and Y. S. Shmaliy (SPIE, Bellingham, WA, 2008), Vol. 7009, p. 70090V.
- L. Parlato, G. P. Pepe, D. Pan, C. De Lisio, V. Pagliarulo, A. Cosentino, N. Marrocco, D. Dalena, G. Peluso, A. Barone, and R. Sobolewski, "Time-Resolved Optical Characterization of Proximized Nano-Bilayers for Ultrafast Photodetector Applications," *J. Phys., Conf. Ser.* **97**, 012317 (2008).
- A. Simon, "An Alternative Analysis of Some Recent Diffusion Experiments on the Large Plasma Device," *Phys. Plasmas* **15**, 022507 (2008).
- A. Simon, "Comment on 'Two-Dimensional Equilibrium of a Low Temperature Magnetized Plasma,'" *Plasma Sources Sci. Technol.* **17**, 028001 (2008).
- T. P. Simula, N. Nygaard, S. X. Hu, L. A. Collins, B. I. Schneider, and K. Mølmer, "Angular Momentum Exchange Between Coherent Light and Matter Fields," *Phys. Rev. A* **77**, 015401 (2008).

S. Wu, J. Zhang, A. Belousov, J. Karpinski, and R. Sobolewski, "Dynamics of Intervalley Transitions and Propagation of Coherent Acoustic Phonons in GaN Single Crystals Studied by Femtosecond Pump-Probe Spectroscopy," in *Gallium Nitride*

Materials and Devices III, edited by H. Morkoç, C. W. Litton, J.-I. Chyi, Y. Nanishi, and E. Yoon, (SPIE, Bellingham, WA, 2008), Vol. 6894, p. 68940K.

Forthcoming Publications

K. U. Akli, S. B. Hansen, A. J. Kemp, R. R. Freeman, F. Beg, D. Clark, D. Hey, K. Highbarger, J. Green, G. Gregori, K. Lancaster, T. Ma, A. J. MacKinnon, P. Norreys, N. Patel, P. K. Patel, R. B. Stephens, C. Stoeckl, M. Storm, W. Theobald, L. Van Woerkom, R. Weber, and M. H. Key, "Laser Heating of Solid Matter by Light Pressure-Driven Shocks," to be published in *Physical Review Letters*.

C. Dorrer, "Effect of Jitter on Linear Pulse Characterization Techniques," to be published in *Optics Express*.

C. Dorrer and I. Kang, "Linear Self-Referencing Techniques for Short Optical Pulse Characterization," to be published in the *Journal of the Optical Society of America B* (invited).

M. C. Ghilea, T. C. Sangster, D. D. Meyerhofer, R. A. Lerche, and L. Disdier, "Aperture Tolerances for Neutron Imaging Systems in Inertial Confinement Fusion," to be published in *Review of Scientific Instruments*.

V. N. Goncharov, "Ablative Richtmyer–Meshkov Instability: Theory and Experimental Results," to be published in the *Proceedings of Scottish Summer School*.

V. N. Goncharov, "Direct-Drive Inertial Fusion: Basic Concepts and Ignition Target Designing," to be published in the *Proceedings of Scottish Summer School*.

V. N. Goncharov, T. C. Sangster, P. B. Radha, T. R. Boehly, T. J. B. Collins, R. S. Craxton, J. A. Delettrez, R. Epstein, V. Yu. Glebov, S. X. Hu, I. V. Igumenshchev, R. Janezic, S. J. Loucks, J. R. Marciante, J. A. Marozas, F. J. Marshall, D. N. Maywar, J. P. Knauer, P. W. McKenty, S. P. Regan, R. G. Roides, W. Seka, S. Skupsky, V. A. Smalyuk, J. M. Soures, C. Stoeckl, R. Betti, R. L. McCrory, D. D. Meyerhofer, D. Shvarts, J. A. Frenje, R. D. Petrasso, and C. K. Li, "Performance of Direct-Drive Cryogenic Targets on OMEGA," to be published in *Physics of Plasmas* (invited).

O. V. Gotchev, P. Brijesh, P. M. Nilson, C. Stoeckl, and D. D. Meyerhofer, "A Compact, Multi-Angle Electron Spectrometer for Ultra-Intense Laser–Interaction Experiments," to be published in *Review of Scientific Instruments*.

S. X. Hu, "Heating of Frozen Rydberg Gases in a Strong Magnetic Field," to be published in the *Journal of Physics B*.

S. X. Hu, V. A. Smalyuk, V. N. Goncharov, J. P. Knauer, P. B. Radha, I. V. Igumenshchev, J. A. Marozas, C. Stoeckl, B. Yaakobi, D. Shvarts, T. C. Sangster, P. W. McKenty, D. D. Meyerhofer, and R. L. McCrory, "Studies of Plastic-Ablator Compressibility for Direct-Drive Inertial Confinement Fusion on OMEGA," to be published in *Physical Review Letters*.

I. V. Igumenshchev, "Magnetically Arrested Disks and Origin of Poynting Jets: Numerical Study," to be published in the *Astrophysical Journal*.

I. Kang, C. Dorrer, L. Zhang, M. Dinu, M. Rasras, L. Buhl, S. Cabot, A. Bhardwaj, X. Liu, M. Cappuzzo, L. Gomez, A. Wong-Foy, Y. F. Chen, N. K. Dutta, S. S. Patel, D. T. Neilson, C. R. Giles, A. Piccirilli, and J. Jacques, "Characterization of the Dynamical Processes in All-Optical Signal Processing Using Semiconductor Optical Amplifiers," to be published in the *IEEE Journal of Selected Topics in Quantum Electronics* (invited).

C. Kim, J. U. Wallace, and S. H. Chen, "Effects of Dilution, Polarization Ratio, and Energy Transfer on Photoalignment of Liquid Crystals Using Coumarin-Containing Polymer Films," to be published in *Macromolecules*.

R. L. McCrory, D. D. Meyerhofer, R. Betti, R. S. Craxton, J. A. Delettrez, D. H. Edgell, V. Yu. Glebov, V. N. Goncharov, D. R. Harding, D. W. Jacobs-Perkins, J. P. Knauer, F. J. Marshall, P. W. McKenty, P. B. Radha, S. P. Regan, T. C. Sangster, W. Seka, R. W. Short, S. Skupsky, V. A. Smalyuk, J. M. Soures,

C. Stoeckl, B. Yaakobi, D. Shvarts, J. A. Frenje, C. K. Li, R. D. Petrasso, and F. H. Séguin, “Progress in Direct-Drive Inertial Confinement Fusion Research,” to be published in *Physics of Plasmas* (review talk).

M. Mikulics, M. Marso, S. Wu, A. Fox, M. Lepsa, D. Gruetzmacher, R. Sobolewski, and P. Kordos, “Sensitivity Enhancement of Metal–Semiconductor–Metal Photodetectors on Low-Temperature-Grown GaAs Using Alloyed Contacts,” to be published in *IEEE Photonics Technology Letters*.

M. Nakatsutsumi, J. R. Davies, R. Kodama, J. S. Green, K. L. Lancaster, K. U. Akli, F. N. Beg, S. N. Chen, D. Clark, R. R. Freeman, C. D. Gregory, H. Habara, R. Heathcote, D. S. Hey, K. Highbarger, M. H. Key, J. A. King, K. Kreskelnick, T. Ma, A. MacPhee, H. Nakamura, R. B. Stephens, M. Storm, M. Tampo, W. Theobald, L. Van Woerkom, R. L. Weber, M. S. Wei, N. C. Woolsey, and P. A. Norreys, “Space and Time Resolved Measurements of the Heating of Solids to Ten Million Kelvin by a Petawatt Laser,” to be published in the *New Journal of Physics*.

P. Nilson, W. Theobald, J. Myatt, C. Stoeckl, C. Mileham, M. Storm, O. V. Gotchev, I. A. Begishev, J. Brown, J. D. Zuegel, R. Betti, D. D. Meyerhofer, and T. C. Sangster, “High-Intensity Laser–Plasma Interactions in the Refluxing Limit,” to be published in *Physics of Plasmas* (invited).

T. C. Sangster, V. N. Goncharov, P. B. Radha, V. A. Smalyuk, R. Betti, R. S. Craxton, J. A. Delettrez, D. H. Edgell, V. Yu. Glebov, D. R. Harding, D. Jacobs-Perkins, J. P. Knauer, F. J. Marshall, R. L. McCrory, P. W. McKenty, D. D. Meyerhofer, S. P. Regan, W. Seka, R. W. Short, S. Skupsky, J. M. Soures, C. Stoeckl, B. Yaakobi, D. Shvarts, J. A. Frenje, C. K. Li, R. D. Petrasso, and F. H. Séguin, “High-Areal-Density Fuel Assembly in Direct-Drive Cryogenic Implosions,” to be published in *Physical Review Letters*.

W. Seka, D. H. Edgell, J. P. Knauer, J. Myatt, A. V. Maximov, R. W. Short, T. C. Sangster, C. Stoeckl, R. E. Bahr, R. S. Craxton, J. A. Delettrez, V. N. Goncharov, I. V. Igumenshchev, and D. Shvarts, “Time-Resolved Absorption in Cryogenic and Room-Temperature, Direct-Drive Implosions,” to be published in *Physics of Plasmas* (invited).

V. A. Smalyuk, D. Shvarts, R. Betti, J. A. Delettrez, D. H. Edgell, V. Yu. Glebov, V. N. Goncharov, R. L. McCrory, P. W. McKenty, D. D. Meyerhofer, P. B. Radha, S. P. Regan, T. C. Sangster, W. Seka, S. Skupsky, C. Stoeckl, B. Yaakobi, J. A. Frenje, C. K. Li, R. D. Petrasso, and F. H. Séguin, “The Role of Hot-Electron Preheat in the Compression of Direct-Drive Imploding Targets with Cryogenic D_2 Ablators,” to be published in *Physical Review Letters*.

A. A. Solodov and R. Betti, “Stopping Power and Range of Energetic Electrons in Dense Plasmas of Fast-Ignition Fusion Targets,” to be published in *Physics of Plasmas*.

M. Storm, I. A. Begishev, R. J. Brown, C. Guo, D. D. Meyerhofer, C. Mileham, J. Myatt, P. M. Nilson, T. C. Sangster, C. Stoeckl, W. Theobald, and J. D. Zuegel, “A High-Resolution Coherent Transition-Radiation Diagnostic for Laser-Produced Electron-Transport Studies,” to be published in *Review of Scientific Instruments*.

W. Theobald, R. Betti, C. Stoeckl, K. S. Anderson, J. A. Delettrez, V. Yu. Glebov, V. N. Goncharov, F. J. Marshall, D. N. Maywar, R. L. McCrory, D. D. Meyerhofer, P. B. Radha, T. C. Sangster, W. Seka, D. Shvarts, V. A. Smalyuk, A. A. Solodov, B. Yaakobi, C. D. Zhou, J. A. Frenje, C. K. Li, F. H. Séguin, R. D. Petrasso, and L. J. Perkins, “Initial Experiments on the Shock-Ignition Inertial Confinement Fusion Concept,” to be published in *Physics of Plasmas*.

A. Trajkovska-Petkoska and S. D. Jacobs, “Effect of Different Dopants on Polymer Cholesteric Liquid Crystals,” to be published in *Molecular Crystals and Liquid Crystals*.

A. Trajkovska-Petkoska, T. Z. Kosc, K. L. Marshall, K. Hasman, and S. D. Jacobs, “Motion of Doped-Polymer-Cholesteric Liquid Crystal Flakes in a Direct-Current Electric Field,” to be published in the *Journal of Applied Physics*.

B. Yaakobi, T. R. Boehly, T. C. Sangster, D. D. Meyerhofer, B. A. Remington, P. G. Allen, S. M. Pollaine, H. E. Lorenzana, K. T. Lorenz, and J. A. Hawreliak, “EXAFS Measurements of Quasi-Isentropically Compressed Vanadium Targets on the OMEGA Laser,” to be published in *Physics of Plasmas*.

Conference Presentations

A. V. Okishev, V. I. Smirnov, L. B. Glebov, and J. D. Zuegel, "Optical Differentiator Based on a Regenerative Amplifier with an Intracavity Tunable Volume Bragg Grating Filter," *Advanced Solid-State Photonics*, Nara, Japan, 27–30 January 2008.

T. C. Sangster, "OMEGA EP High-Energy Petawatt Laser: Status and Progress," *JOWOG '08*, Los Alamos, NM, 4–8 February 2008.

W. T. Shmayda, "Fusion-Power and Hydrogen-Economy Community Material Issues," *American Ceramic Society Conference*, Cocoa Beach, FL, 24–27 February 2008.

J. M. Soures and D. D. Meyerhofer, "OMEGA and OMEGA EP Provide Unique Capabilities for NLUF Programs," *NNSA–SSAA Symposium*, Washington, DC, 26–28 February 2008.

A. V. Okishev, "The OMEGA/OMEGA EP Laser System: New Frontiers in ICF and HEDP Research," *X Khariton's Topical Scientific Readings*, Sarov, Russia, 11–14 March 2008.

The following presentations were made at the NIF Diagnostic Workshop, Los Alamos National Laboratory, Los Alamos, NM, 28 March 2008:

V. Yu. Glebov, T. C. Sangster, C. Stoeckl, M. Cruz, S. Roberts, M. Moran, and R. A. Lerche, "A Neutron Bang Time (NBT) Detector for the THD Campaign on the NIF."

V. Yu. Glebov, T. C. Sangster, C. Stoeckl, T. Duffy, M. Cruz, S. Roberts, M. Moran, and R. A. Lerche, L. Dauffy, R. Tommasini, A. Throop, J. Celeste, Z. A. Ali, and C. J. Horsfield, "The NIF Neutron Time-of-Flight (nTOF) Diagnostic Status and Plans."

